Technical Note

CEL

TN no. N-1608

title: THE STRUMMING VIBRATIONS OF MARINE CABLES: STATE OF THE ART

author: O.M. Griffin, S.E. Ramberg, R.A. Skop, D.J. Meggitt and S.S. Sergev

date: May 1981

sponsor: Naval Research Laboratory

program nos: YF59-556-091-01-400

CIVIL ENGINEERING LABORATORY
NAVAL CONSTRUCTION BATTALION CENTER
Port Hueneme, California 93043

Unclassified

SECURITY CLASSIFICATION OF THIS PAGE (When Data Entered)

REPORT DOCUMENTATION PAGE

READ INSTRUCTIONS BEFORE COMPLETING FORM

1. REPORT NUMBER: TN-1608	2. GOVT ACCESSION NO.: DN787011
3. RECIPIENT'S CATALOG NUMBER:	
4. TITLE (and Subtitle): THE STRUMMING VIBRATIONS OF MARINE CABLES: STATE OF THE ART	5. TYPE OF REPORT & PERIOD COVERED: Final, FY 1981
	6. PERFORMING ORG. REPORT NUMBER:
7. AUTHOR(s): O.M. Griffin, S.E. Ramberg, R.A. Skop, D.J. Meggitt, and S.S. Sergev	8. CONTRACT OR GRANT NUMBER(s):
9. PERFORMING ORGANIZATION NAME AND ADDRESS: Naval Research Laboratory, Washington, DC 20375	10. PROGRAM ELEMENT, PROJECT, TASK AREA & WORK UNIT NUMBERS: CEL Proj. YF59-556-091-01-400, NRL Problem 0274-0-1
11. CONTROLLING OFFICE NAME AND ADDRESS: Civil Engineering Laboratory, Naval Construction Battalion Center, Port Hueneme, CA 93043	12. REPORT DATE: May 1981
	13. NUMBER OF PAGES: 198
14. MONITORING AGENCY NAME & ADDRESS(if different from Controlling Office):	15. SECURITY CLASS. (of this report): Unclassified
	15a. DECLASSIFICATION/DOWNGRADING SCHEDULE:

16. DISTRIBUTION STATEMENT (of this Report)

This publication is required for official use or for administrative or operational purposes only. Distribution is limited to U.S. Government Agencies. Other requests must be referred to the Civil Engineering Laboratory, Naval Construction Battalion Center, Port Hueneme, CA 93043

17. DISTRIBUTION STATEMENT (of the abstract entered in Block 20, if different from Report)

18. SUPPLEMENTARY NOTES

19. KEY WORDS (Continue on reverse side if necessary and identify by block number)

Cable strumming vibrations; vortex-excited vibrations; marine cable systems; ocean engineering.

20. ABSTRACT (Continue on reverse side if necessary and identify by block number)

This report discusses recent findings on strumming of cables from the marine cable dynamics research program conducted by the Naval Facilities Engineering Command. Emphasis is placed on an understanding of the basic strumming phenomenon, the development of design procedures, the definition of hydrodynamic force coefficients applicable in practice, and the specification of structural response parameters relevant to marine cable design. Strumming analysis methods for both taut and slack marine cables are described

continued

DD FORM 1 JAN 73 1473 EDITION OF 1 NOV 65 IS OBSOLETE

Unclassified

SECURITY CLASSIFICATION OF THIS PAGE (When Data Entered)

20. Continued

together with the computer codes that are available to implement the various analysis procedures. Although this report emphasizes marine cable systems, the results of the NAVFAC/CEL research effort are applicable to other marine structures as well. These applications are discussed in the report as appropriate.

Library Card

Civil Engineering Laboratory
THE STRUMMING VIBRATIONS OF MARINE CABLES: STATE OF THE ART (Final), by Griffin, Ramberg, Skop, Meggitt, and Sergev
TN-1608 198 pp illus May 1981 Unclassified

1. Cable strumming vibrations 2. Marine cable systems I. YF59-556-091-01-400

This report discusses recent findings on strumming of cables from the marine cable dynamics research program conducted by the Naval Facilities Engineering Command. Emphasis is placed on an understanding of the basic strumming phenomenon, the development of design procedures, the definition of hydrodynamic force coefficients applicable in practice, and the specification of structural response parameters relevant to marine cable design. Strumming analysis methods for both taut and slack marine cables are described together with the computer codes that are available to implement the various analysis procedures. Although this report emphasizes marine cable systems, the results of the NAVFAC/CEL research effort are applicable to other marine structures as well. These applications are discussed in the report as appropriate.

Technical Note TN 1608

The Strumming Vibrations of Marine Cables: State of the Art

O. M. Griffin, S. E. Ramberg, and R. A. Skop

Marine Technology Division
Naval Research Laboratory
Washington, DC 20375

D. J. Meggitt and S. S. Sergev

Civil Engineering Laboratory

May 1981

CIVIL ENGINEERING LABORATORY
NAVAL CONSTRUCTION BATTALION CENTER
Port Hueneme, CA 93043

CONTENTS

FOREWORD AND ACKNOWLEDGMENTS

The overall preparation of this report was undertaken as part of the research program of the Naval Research Laboratory (NRL). The NRL cable dynamics program has been sponsored by the Civil Engineering Laboratory (CEL), Naval Construction Battalion Center (NCBC), which also sponsored the towing channel cable strumming experiments at the David Taylor Naval Ship Research and Development Center (DTNSRDC). The authors are grateful to Mr. J.H. Pattison for providing detailed reports of the towing channel experiments. The authors also are grateful to Professor T. Sarpkaya of the Naval Postgraduate School for providing detailed reports of the NPGS laboratory-scale experiments which were sponsored by CEL.

These efforts are part of the Naval Facilities Engineering Command (NAVFAC) cable dynamics research program for which sponsorship and technical coordination are provided by CEL. The MIT experiments described in this report were sponsored by the Office of Naval Research, Code 480, and the authors are grateful to Dr. J. K. Vandiver of the Ocean Engineering Department at MIT for providing detailed accounts of those field experiments. The camera-ready manuscript for this report was composed by the Computerized Technical Composition Office at NRL.

EXECUTIVE SUMMARY

Vortex-excited oscillations of marine cable systems and structures are caused by the resonant, nonlinear interaction between the flowing water and the structure, which takes place as a result of vortex shedding. These oscillations usually are characterized by a resonant wake capture or "lock-on" phenomenon in which the wake flow and the body oscillate in unison at the same frequency. In the case of a cable these relatively high frequency oscillations, which are predominantly in a direction normal to the incident flow, are called *strumming*. Reduced fatigue life, large hydrodynamic forces (particularly drag) and induced stresses, and high acoustic noise levels often accompany vortex-excited oscillations. The reliability of a cable system's performance depends on the ability to predict this dynamic behavior for conditions that are commonly found in the ocean environment.

The objective of this report is to present an overview of the state of knowledge concerned with strumming oscillations and to apply these findings to the development of design methods for cable systems that are likely to undergo these oscillations. The report emphasizes recent findings from the marine cable dynamics research program conducted by the Naval Facilities Engineering Command. Although this report emphasizes marine cable systems, results of the NAVFAC/CEL research effort are applicable to other marine structures as well. These applications are discussed in the report as appropriate.

This report is limited in scope to the problems caused by vortex shedding from bluff, flexible structures and cables in steady currents, and the resulting vortex-excited oscillations. Emphasis is placed on an understanding of various aspects of the basic phenomena, the development of design procedures, the definition of hydrodynamic force coefficients applicable in practice, and the specification of structural response parameters relevant to marine cable design.

Section 2 of this report gives detailed discussions of the present state-of-the-art concerning the vortex-excited oscillations of flexible, cylindrical structures with nominally circular cross-sections. Particular attention is given to the behavior of a cable in a flowing fluid and to the specification of the hydrodynamic forces and the resonant vibration response characteristics. The coherence or phase uniformity of the vortex shedding due to lock-on also is discussed. The effects of yaw or inclination of the cable, surface roughness, and shear (nonuniform flow) gradients are assessed in terms of their influence on vortex-excited oscillations.

In Section 3 of the report a discussion is given of recent experimental studies of cable strumming. The physical scales of the experiments range from relatively small flow channels, to large towing channels and to field experiments in the oceanic environment. The field experiments encompass relatively small-scale tests conducted in a tidal inlet and large-scale, deep water tests of moored arrays.

Analytical models which have been developed for the prediction of cable strumming are discussed in Section 4 of the report. The various modelling approaches taken by different investigators are reviewed, and recommendations are made for applications to the cable design process. Comparisons are made between the model predictions and available experimental data from both laboratory and field scale tests. A discussion is given of the prediction methods and design procedures which have been developed and calibrated for practical applications. The parameters that must be considered in an assessment of the severity of strumming oscillations are defined and step-by-step procedures are given for making such an assessment.

Computer codes for predicting and modelling cable strumming are described in Section 5. The codes that have been developed for ocean engineering applications comprise two areas of application: the static analysis of cable arrays and the dynamics of marine cables. NATFREQ is a code for calculating natural frequencies, mode shapes, and drag amplification factors for taut cables with attached masses. DESADE and DECEL 1 are two versions of a code that was developed to statically analyze

structural marine cable arrays. This code includes a resonant vibration analysis routine which calculates the static deflections of the array due to the added drag forces that accompany strumming oscillations. SEADYN is a nonlinear finite element cable system model being developed by CEL. A wide variety of systems can be modeled, including: pay-out and reel-in, time varying current fields, and point loads. The Skop-Griffin strumming model has been incorporated into SEADYN. SLAK is a finite-element computer code that was originally developed for the analysis of the free vibrations of slack cables in three dimensions. This code has been adapted at NRL for ocean engineering calculations of cable equilibrium shapes, support reaction forces, natural frequencies and the mode shapes with respect to the equilibrium position.

Several appendices are included to provide additional details on topics discussed in the body of the report. These topics include the dynamics of taut and slack marine cables, and the measurement of cable added mass and hydrodynamic damping coefficients. Another appendix provides the mathematical background for the "wake-oscillator" approach to modelling vortex-excited oscillations. Other types of modelling approaches (i.e., empirical, discrete-vortex, etc.) are also discussed in order to provide a complete background to the cable designer.

NOMENCLATURE AND LIST OF SYMBOLS[†]

a,b,c	Coefficients defined in Table 4.2
$a_1,\ b_1,\ c_1,\ d_1$	Coefficients defined in Table 4.3.
C_{dh}	Unsteady force coefficient on a cylinder or cable vibrating in the cross flow direction; see equation (E1.5).
C_{mh}	Unsteady force coefficient on a cylinder or cable vibrating in the cross flow direction; see equation (E1.5).
$C_D,\ C_{DO}$	Steady drag coefficient on a vibrating (stationary) cylinder or cable.
C_L	Lift coefficient; see equation (E1.2)
C_{LE}	Excitation force coefficient; see equation (2.4)
C_R	Reaction force coefficient; see equation (E1.2)
C_{RE}	Fluid reaction (damping) force coefficient; see equation (2.5)
D	Cable diameter (m or ft).
f_n	Natural frequency (Hz).
f_s	Strouhal frequency (Hz).
I_i	Modal scaling factor; see equation (2.3).
k_s	Reduced damping; see equation (2.2).
L	Cable length (m or ft).
m	Cable physical mass per unit length (kg/m or lb_m/ft).
m_e	Effective mass per unit length (kg/m or lb_m/ft); see equation (5.1) and example 8.3 (physical plus added mass).
m'	Cable virtual mass (physical plus added mass) per unit length (kg/m or lb_m/ft).
Re	Reynolds number, VD/ν.
Re_v	Vibration Reynolds number, $fD^2/2\nu$
St	Strouhal number, f_sD/V.

[†]Other symbols not listed here are defined in Appendices A through E.

T	Cable static tension (N or lb_f)
u	Wake velocity fluctuation (m/s or ft/sec); see equation (2.6).
V	Incident flow velocity (m/s or ft/sec or knots).
V_r	Reduced velocity, $V/f_n D$.
$V_{r,crit}$	Critical reduced velocity.
ω_r	Response parameter, $(1 + 2\bar{Y}/D)\ (V_r\ St)^{-1}$; see equation (4.3.2).
W	Phase angle function; see Table 2.3 and Appendix E.
$\bar{x}$	In line displacement (m or ft).
$\bar{X}$	In line displacement amplitude (m or ft).
$\bar{y}$	Cross flow displacement (m or ft).
$\bar{Y}$	Cross flow displacement amplitude (m or ft).
Y	Normalized displacement amplitude, $\bar{Y}/D$.
$Y_{EFF,MAX}$	Normalized displacement amplitude; see equation (2.3).
$\bar{z}$	Coordinate measurement along the cylinder or cable (m or ft).
β	Yaw angle (deg or rad).
β'	Phase angle (deg or rad); see Table 2.3.
$\bar{\beta}$	Shear flow parameter; see equation (2.8).
δ	Log decrement of structual damping; also surface roughness (see equation (2.7).
ϵ	Phase angle (deg or rad); see equation (E1.8).
γ_i	Normalizing factor; see equation (4.3.1).
ϕ	Phase angle (deg or rad); see equation (E1.2).
ϕ_1	Phase angle (deg or rad); see equation (E1.2).
μ	Mass ratio, see equation (E1.1).
ν	Kinematic fluid viscosity (m^2/sec or ft^2/sec).
ρ	Fluid density (kg/m^3 or lb_m/ft^3).
ρ_s	Cable density (kg/m^3 or lb_m/ft^3).
ρ_{AB}	Correlation coefficient; see equation (2.6).

$\psi_i(z)$	Mode shape for i th flexible beam mode; see Table E1.
ζ_s	Structural damping ratio; see equation (E1.1).

LIST OF FIGURES

The Strumming Vibrations of Marine Cables:

State of the Art

1. INTRODUCTION

1.1 Objectives. At the beginning of Fiscal Year 1975, technical management of the NAVFAC cable dynamics research program was undertaken by the Civil Engineering Laboratory, Naval Construction Battalion Center. The overall objective of this program, as stated in a research plan put forward by CEL/NCBC, is:

"... to provide for the development of effective methods for the analysis of the dynamic response of 3-dimensional, moored cable structures which undergo dynamic motions generated by various natural or man-produced causes. Failure to predict this dynamic behavior by suitable analytical techniques will affect the confidence in the adequacy of the system design as well as the estimated reliability of the system's performance."

"[One aspect of this problem] is the small-displacement, "high frequency" response generated by shedding vortices as water flows past the cable-this response is commonly referred to as cable strumming. The objective of the plan for this specific area is twofold: (1) development of a capability to predict the strumming response (i.e., deflection, frequency, generated acoustic energy, and drag force) of cable networks which have horizontally or vertically oriented cable segments, in taut or catenary configuration subjected to a current which may vary along the cable length, and (2) development of techniques which can be used to suppress cable strumming."

This report considers the problem of marine cable design against strumming vibrations. The suppression of these vibrations is dealt with in a separate CEL-sponsored report.†

†J.E. Kline, A. Brisbane and E.M. Fritzgerald, "Cable Strumming Suppression" MAR Inc., Technical Report 249, July 1980.

1.2 Background. It is often found that bluff, or unstreamlined, structures display some form of undesirable oscillatory instability arising from motion relative to a surrounding fluid. A common mechanism for resonant, flow-excited oscillations is the organized and periodic shedding of vortices as the flow separates alternately from opposite sides of a long, bluff body. The flow field exhibits a dominant periodicity and the body is acted upon by time-varying pressure loads. These result in steady and unsteady drag forces in line with the flow and unsteady lift or side forces perpendicular to the flow direction. If the structure is flexible and lightly damped internally as in the case of a cable, then resonant oscillations can be excited normal or parallel to the incident flow direction. For the more common cross flow oscillations, the body and the wake have the same frequency of oscillation which is near one of the characteristic frequencies of the structure. The shedding meanwhile is shifted away from the natural, or Strouhal, frequency at which pairs of vortices would be shed if the structure were restrained from oscillating. This phenomenon is known as "lock-on" or "wake capture."

The vortex-excited oscillations of marine cables, commonly termed *strumming*, result in early fatigue, increased hydrodynamic forces and amplified acoustic flow noise; they sometimes lead to structural damage and possibly to failure. Flow-excited oscillations very often are a critical factor in the design of underwater cable arrays, mooring systems, drilling risers, and offshore platforms, since these complex structures usually have bluff cylindrical shapes which are conducive to vortex shedding when they are placed in a flow. An understanding of the basic nature of the fluid-structure interaction which produces vortex-excited oscillations is an important consideration in the reliable design of offshore structures and cable systems.

Problems associated with the shedding of vortices often have been neglected in the past in relation to the design of offshore platforms and cable structures, largely because reliable experimental data and design methods have not been available. However, the dynamic analysis of ocean structures and cable systems has become increasingly important in the prediction of stress distributions and fatigue life in the offshore environment. These factors are particularly relevant as new and more complex systems

must be designed to withstand the deep ocean environment over long time periods. Reliable experimental data are now in hand for the dynamic response of and flow-induced forces on a model scale. Based upon these experiments, semi-empirical prediction models have been developed and favorably compared with field test data.

1.3 NAVFAC/CEL Research Program in Cable Strumming. During the late 1960's and early 1970's the Navy conducted several experiments on large, three-dimensional moored cable structures. These structures were intended to serve as platforms for a variety of oceanographic sensors. In general, the performance of these cable structures was substantially less than desired, due primarly to a lack of adequate means for calculating the dynamic response of the structure during installation or while in place in the water column. In recognition of the Navy's inadequate capabilities for the design and prediction of the performance of moored cable structures, the Civil Engineering Laboratory (CEL) of the Naval Facilities Engineering Command (NAVFAC) initiated a research program to develop effective means for the analysis of the dynamic response of complex, three-dimensional moored cable structures in the ocean.

The objectives of the strumming portion of the research were twofold: (1) development of a capability to predict the strumming response (i.e., deflection, vibration amplitude and frequency, drag force) of cable networks which have cable segments at arbitrary orientation to the flow, in taut or catenary configurations with or without attached masses, subjected to a current which may vary in magnitude or direction along the cable length; and (2) development of techniques which can be used to suppress cable strumming.

The research plan reviewed the analytical models then available (1974) for the calculation of strumming and concluded that the so-called semi-heuristic approach offered the most promise for extension to the strumming of cables. At the time the plan was written, the models had been applied only to two-dimensional rigid cylinders. The first step in model development, then, was the extension of the models to taut, flexible cables in uniform, perpendicular currents. Succeeding efforts extended the models to yawed cables in uniform currents, slack cables and to cables in nonuniform currents.

The research plan also recommended an extensive program of laboratory and field experiments to provide data for validating the analytical models at each stage of development. The laboratory experiments were to be conducted in water tunnels, towing tanks and wind tunnels, depending on the particular aspect of the phenomenon being investigated and the scale of model required.

1.4 Scope of the Report. This report is limited in scope to the problems caused by vortex shedding from marine cable structures and moorings, and to the resonant cross flow or strumming oscillations that often are excited by the vortices. The topics discussed in this report are primarily concerned with, but not limited to, the various elements of the NAVFAC/CEL cable dynamics research program. A discussion is given of the basic fluid dynamic characteristics of a cable in an incident flow, including the hydrodynamics forces, resonant dynamic response characteristics and Reynolds number effects. Additional consideration is given to the fluid/structure interaction effects of shear (nonuniform flow) and roughness of the cable surface. Relevant experimental findings from towing channel experiments, small-scale field experiments and large scale field experiments also are discussed.

Strumming analysis methods for both taut and slack marine cables are described together with the computer codes that are available to implement the various analysis procedures. Emphasis is placed here on the development of design procedures, on the definition of hydrodynamic loads and force coefficients applicable in practice, and on the definition of structural and hydrodynamic response parameters relevant to marine cable design. Towing cable hydrodynamics is not considered explicitly in this report, though many of the topics discussed also are applicable to that problem as well.

2. CROSS FLOW STRUMMING OSCILLATIONS

2.1 Resonant Cross Flow Response Characteristics. The frequency f_s of the vortex shedding from a circular cylinder is related to the other main flow parameters (D, the diameter of a cylinder; V, the flow velocity) parameters through the nondimensional Strouhal number defined as follows

$$St = \frac{f_s D}{V}.$$

The value of the Strouhal number varies somewhat in different regimes of the Reynolds number and with the shape of the cylinder (circular, *D*-section, etc.). For the ranges of the Reynolds number when the Strouhal number remains constant the relation between the shedding frequency and the velocity is linear for a given cylinder, i.e.

$$f_s = KV,$$

where $K = St/D$. When a cylinder immersed in a flowing fluid is free to oscillate in the cross-flow direction, the latter relation does not hold in the vicinity of the natural frequency of the cylinder. This complex resonance phenomenon— called "lock-on" or wake capture — is discussed in detail in this section of the report.

If the Reynolds number is lower than about 10^5, then the vortex shedding is predominantly periodic and the value of the Strouhal number can be assumed to be roughly 0.2 for a circular cylinder or cable. The Strouhal number — Reynolds number dependence is discussed further in Section 2.4. Measurements of the frequencies, displacement amplitudes and forces which result from vortex-excited oscillations have been obtained by many investigators from experiments both in air and in water. In this section of the report, some of the most recent of these experiments and related studies are summarized in order to provide a background for the cable strumming problem. A detailed review of the basic aspects of the problem of vortex-excited oscillations in general has been made recently by Sarpkaya (1). King (2) and Griffin (3) have reviewed the subject in the context of ocean engineering applications.

A typical structure used for experimental strumming tests consists of a cylinder positioned normally to the flow and flexibly supported at each end. Representative measurements for such a cylinder in air have been reported by Griffin and Koopmann (4) and in water by Dean, Milligan and Wootton (5). The results obtained are generally the same in both media; as the incident flow velocity V, or the "reduced velocity" V_r as in Fig. 2.1, is increased, the unsteady displacement amplitude first builds up to a maximum, after which it begins to decrease as the upper limit of the locking-on range between the vortex and vibration frequencies is approached. For one example shown in the figure, the lock-on lim-

its, defined by vibration displacements greater than the resonant threshold ($2\bar{Y}/D = 0.1$), are given by reduced velocities $V_r = 4.5$ and 7.5 in air, with the maximum displacement amplitude occuring at $V_r \sim 6$. For the in-water experiments the resonance band is somewhat wider, from $V_r = 4$ to nearly 8, but the peak displacement amplitude again is excited at $V_r \sim 6$. The narrow resonance band in air is typical of lightly-damped systems while the broad resonance in water is typical of systems with relatively higher structural damping. From the table in the figure it can be seen that even though the damping and mass ratios of the two systems differ by factors of ten, the reduced damping is very nearly the same and so are the peak displacement amplitudes Y_{MAX} for the two cylinders. Typical values of V_r corresponding to Y_{MAX} are listed in Table 2.1.

When Reynolds and Froude number effects are neglected, the maximum cross flow displacement amplitude can be expressed from dimensional analysis as being dependent on three quantities, viz.,

$$Y_{MAX} = \bar{Y}_{MAX}/D = f\left[\frac{\omega_s}{\omega_n}, \zeta_s, \mu\right]. \tag{2.1}$$

Here ω_s/ω_n is the ratio of the Strouhal and structural frequencies $\omega_s = 2\pi St\ V/D$ and ω_n, respectively; and ζ_s is the *structural* damping ratio. The parameter μ is a mass ratio, defined by $\mu = \rho D^2/8\pi^2 St^2 m$, where ρ is the fluid density and m is the structure's or cable's effective mass. St is the Strouhal number and D is the cylinder diameter. This parameter also results from the normalization of the force coefficients in the governing equation of structural motion as shown, for example, by Griffin (6), Sarpkaya (1), and Vickery and Watkins (7).

It has been demonstrated experimentally (2,3,7) that the peak displacement amplitude $\bar{Y}_{MAX}$ of vortex-excited oscillation for any given structure is a function of a "reduced damping parameter" of the form:

$$k_s = \frac{2m\delta}{\rho D^2}, \tag{2.2a}$$

or equivalently

$$\zeta_s/\mu = 2\pi St^2 k_s,\ St = \frac{f_s D}{V}, \tag{2.2b}$$

Table 2.1
Reduced Velocity $V_r = V/f_n D$ at the Peak Cross Flow Displacement Amplitude Due to Vortex Shedding

Type of Structure	Medium	Investigators	$V_r = \frac{V}{f_n D}$
A*	Air	Griffin, Skop and Koopmann (1973)	6.1-6.3
A	Air	Parkinson, Feng and Ferguson (1966)	6.1
A	Air	Glass (1969)	5.9
A	Water	Glass (1970)	8.0
A	Air	Koopmann (1970)	6.7
A	Air	Nakamura (1977)	5.0
B	Water	King, Prosser and Johns (1973)	6.0-7.5
C	Air	Mei and Currie (1969)	6.1
D	Water	Dale, Menzel and McCandless (1966)	5.8-6.6
E	Water	Cohen (1975)	5.8
F	Water	Dean, Milligan and Wootton (1977)	6.0

A—Elastically-mounted rigid circular cylinder.
B—Flexible cantilever circular cylinder.
C—Pivoted rigid circular cylinder.
D—Flexible hydrophone cable.
E—Flexible cable with steel rod core.
F—Flexible cylinder, clamped-clamped ends.

(δ is the logarithmic decrement of the cable's structural damping, i.e. $\delta = 2\pi\zeta_s$ when the damping is small). The importance of the reduced damping follows directly from an energy balance on the vibrating cylinder or cable at resonance. Moreover, the relation between Y_{MAX} and k_s or ζ_s/μ is valid for flexible cylindrical structures with normal modes $\psi_i(z)$, for vibrations in the ith mode; z is the spanwise coordinate. The local cross flow displacement is then

$$y_i = Y \psi_i (z) \sin \omega t$$

at each z, and the maximum displacement amplitude is scaled by the factor

$$Y_{EFF,MAX} = Y_{MAX} I_i^{1/2} / |\psi_i(z)|_{MAX} = Y_{MAX}/\gamma_i \tag{2.3a}$$

where the modal scaling factor I_i is defined by

$$I_i = \frac{\int_0^L \psi_i^4(z)\, dz}{\int_0^L \psi_i^2(z)\, dz} \text{ or } \gamma_i = \frac{|\psi_i(z)|_{MAX}}{I_i^{1/2}}. \tag{2.3b}$$

Equation (2.3b) was obtained by Iwan (8) and Skop and Griffin (9) in the course of developing a "wake-oscillator" formulation for predicting the vortex-excited oscillations of structures (see Appendix D). Typical values of I_i are tabulated in references 3, 8 and 9, and in Table E1.

Experimental measurements of $Y_{EFF,MAX}$ as a function of ζ_s/μ are plotted in Fig. 2.2. These results encompass a wide range of single cylinders of various configurations at Reynolds numbers from Re = 300 to 10^6. All available experiments to date indicate that the limiting unsteady displacement for an elastically-mounted rigid cylinder is about $2Y_{EFF,MAX} \approx 2$ to 3, as shown in the figure. This result has been obtained both in air and in water, even though the mass ratios of vibrating cylinders in the two media differ by as much as two orders of magnitude. For cylinders and cables vibrating in water the mass ratio $\frac{m}{\rho D^2}$ varies from slightly greater that 1 to about 8; in air typical values of the mass ratios corresponding to the figure cover a range $\frac{m}{\rho D^2} = 25$ to 500. The experimental data in Fig. 2.2 indicate that the reduced damping can increase by a factor of nearly *fifty* ($\zeta_s/\mu = 0.01$ to 0.5) while the peak-to-peak displacement amplitude decreases by a factor of only about *two* or *three* (2-3 diameters to 1 diameter). In that range of the figure the hydrodynamic forces predominate and the light, flexible structures that are typically employed in water (cables, cantilevered beams) can undergo large cross flow oscillations.

A fairly wide variety of structural elements is included in the data. For example, the experiments of Vickery and Watkins (7) were conducted with a pivoted rigid cylinder in incident flows of both water and air. As noted previously, Dean, Milligan and Wootton (5) measured the cross flow response in water of both spring-mounted cylinders and flexible cylindrical beams. King's results (3, 10, 11) were

obtained with yawed and unyawed flexible cantilevered cylinders that underwent cross flow oscillations in flowing water of various depths (in relation to the cylinder's length).

Table 2.2. Vortex-excited cross flow displacement amplitude response of cylindrical structures.
Legend for Data Points in Fig. 2.2

Type of cross-section and mounting; medium	Symbol
Various investigators, from Griffin (6):	
Spring-mounted rigid cylinder; air	* ○ ⊣ ◙ ◐
Spring-mounted rigid cylinder; water	♦
Cantilevered flexible circular cylinder; air	△
Cantilevered flexible circular cylinder; water	X ▽ ⊕
Pivoted rigid circular rod; air	□ ▲
Pivoted rigid circular rod; water	●
From Dean, Milligan and Wootton (5):	
Spring-mounted rigid cylinder; water	◩
Flexible circular cylinder, $L/D = 240$; water	◪
From King (16):	
Cantilevered flexible circular cylinder, $L/D = 52$ (PVC); water	◴
Cantilevered flexible circular cylinder, $L/D = 52$ (Stainless steel); water	◶

2.2 Hydrodynamic Forces. The unsteady fluid dynamic forces acting on a resonantly vibrating, cylindrical structure due to vortex shedding have been categorized as follows (4,6):

- The exciting force, by which energy is transferred to the structure and which drives the vibrations;
- The reaction or damping force, which is exactly out-of-phase with the structure's velocity;
- The "added mass" force, which is exactly out-of-phase with the structure's acceleration;
- The fluid inertia force.

These components can be deduced from the total hydrodynamic force as measured, say, by Sarpkaya (12) and Mercier (13); or the components can be measured individually as discussed by Griffin and Koopmann (4,6). This decomposition of the forces is carried one step further than one proposed by Sarpkaya (1), who divides the total transverse force into "drag" and inertia terms. The "drag" term is the *negative* of the lift as it is usually characterized. Both characterizations of the force components have their merits depending upon the particular situation being studied and there is a direct correspondence between them, as discussed in references 3 and 6, and in Appendix E.

Some practical and useful comparisons can be made between the fluid forces measured when a cylinder is forced to vibrate and the fluid forces measured when the cylinder is resonantly excited by vortex shedding. The forced cylinder measurements discussed here were made in water by Sarpkaya (1,12) and Mercier (13) and the self-excited cylinder measurements were made in air and in water by Griffin and Koopmann, King and others as indicated in Table 2.3 (see references 3 and 6).

Table 2.3. Hydrodynamic Forces on Circular Cylinders; from Sarpkaya (12).

		Reduced Velocity, $V_r = 5$.		Fluid Force Components, Equation (E1.10)		
Displacement, $Y = Y/D$	Inertia Coefficient,[++] C_{mh}	Drag Coefficient, C_{dh}	Phase Angle, $\beta' = \arctan [C_{dh}/C_{mh}]$	Excitation, $-C_{dh}\cos\epsilon$	Damping, $-C_{mh}\sin\epsilon$	Inertia, $C_{dh}\sin\epsilon$
0.13	0.4	-0.2	-26.6°	0.18	0.18	0.089
0.25	0.4	-0.35	-41.2°	0.26	0.26	0.23
0.50	1.0 to 2.2	-0.9	-42° to -22.3°	0.67 to 0.83	0.67 to 0.83	0.67 to 0.83
0.75	1.0 to 2.2	-0.6	-28.8° to -11.9°	0.48 to 0.54	0.48 to 0.54	0.26 to 0.11

[+] $\epsilon = \beta' + \gamma$ and $\gamma = \arctan W$, where $W = \dfrac{2\alpha\zeta_s}{1-\alpha^2}$, $\alpha = \dfrac{\omega}{\omega_n}$. In addition $W = 0.05$ is assumed (See Appendix E).

[++] The inertia coefficient is evaluated here in coordinates appropriate to a cylinder vibrating in a quiescent fluid or, equivalently, a fluid in uniform, steady motion.

Typical measurements reported by Sarpkaya appear in Figs. 2.3 through 2.6. The measured values for the inertia coefficient C_{mh} are shown in Figs. 2.3 and 2.5 as a function of the reduced velocity V_r, for displacements from equilibrium of $Y = \bar{Y}/D = 0.5$ and 0.75. Of particular note is the marked variation in C_{mh} in the vicinity of $V_r = 5$. This effect corresponds to the large phase shift in the fluid force relative to the vibratory displacement when the characteristic frequency of the flow is locked onto the

vibration frequency. The fluid force on the cylinder is dominated by inertia contributions at the cylinder frequency at low reduced velocities. Measurements by Bearman and Currie (14) of the phase between the pressure at 90 degrees from the front stagnation point and the cylinder's displacement confirm this large inertia effect at low V_r.

The drag or resistance force C_{dh} is plotted in Figs. 2.4 and 2.6 as a function of V_r at the same displacements, $Y = 0.50$ and 0.75. This component of the total fluid dynamic force is negative and becomes dominant near $V_r = 5$. As noted earlier, C_{dh} is the *negative of the lift coefficient as it is usually characterized*, so that the negative values of C_{dh} near $V_r = 5$ suggest a net transfer of energy to the cylinder in that region. These forced-cylinder results are comparable to the vortex-excited forces which act upon resonantly vibrating cylinders when the reduced damping is sufficiently small as in the left-hand portion of Fig. 2.2. It should be noted that C_{mh} and C_{dh} are Fourier-averaged coefficients and contain only the components of the total fluid force at the vibration frequency f. Considerable power is contained in the fluid force spectrum at other frequencies (i.e. $2f$, the Strouhal frequency f_s) for reduced velocities outside of the regime of locking-on between the vortex and vibration frequencies.

The excitation component of the lift force is defined as

$$C_{LE} = C_L \sin \phi = -C_{dh} \cos \epsilon^{\dagger}. \tag{2.4}$$

The measurements in Figs. 2.3 through 2.6 are now compared to previous measurements by other investigators. The minimum value of C_{dh} in Fig. 2.4 occurs at $V_r = 5$, and similar results were obtained at the displacements $Y = 0.13$, 0.25, and 0.75. The several values of C_{dh} and C_{mh} so obtained are listed in Table 2.3 together with the related values of the force components derived from them. For all of these cases of forced vibration the condition for self-excitation

$$C_{mh} - W C_{dh} > 0$$

is satisfied, thus assuring the possibility of the equivalent vortex-excited oscillation. The results for C_{LE} are plotted against the effective displacement in Fig. 2.7 together with a host of similar findings. The conditions under which the experiments were performed are described in Table 2.4.

†See Appendix E.

Table 2.4. The Excitation Force Coefficients on Vibrating Bluff Cylinders; Description of the Data in Figure 2.7

Symbol	Type of cylinder	Medium	Cylinder material	Investigator(s)
Δ	Flexible cantilever	Water	PVC	King (1977)
□			PVC	
			Aluminum	
			Stainless steel	
⊙	Pivoted rigid cylinder	Water & Air	Brass	Vickery and Watkins (1964)
+	Spring-mounted rigid cylinder	Air	Aluminum tubing	Griffin and Koopmann (1977)
□	Rigid cylinder, forced oscillations	Water	Stainless steel	Mercier (1973)
○	Rigid cylinder, forced oscillations	Water	Aluminum tubing	Sarpkaya (1978)
Δ	Flexible cantilever	Air	Aluminum	Hartlen, Baines and Currie (1968)

The excitation component C_{LE} of the total hydrodynamic force is important because it is this component of the fluid force system that transfers energy to the structure or cable and drives the strumming vibration. Several important characteristics of the unsteady lift and pressure forces that accompany vortex-excited oscillations are clear from the results. First there is a *maximum* of the exciting force coefficient at a peak-to-peak displacement between 0.6 and 1 diameters for all the cases shown in the figure. Second, the maximum of the force coefficient is approximately $C_{LE} =$ 0.5 to 0.6 for all but one case, the sole exception being the result at $C_{LE} =$ 0.75. C_{LE} then decreases toward zero in all cases and results in a limiting effective displacement of 2 to 3 diameters (peak-to-peak). This limit is clearly shown by the displacement amplitudes measured at low reduced damping in Fig. 2.2.

The decomposition of the fluid dynamic forces described here is based upon the supposition that both flow-induced lift (excitation) and flow-induced reaction (damping) forces act on a resonantly vibrating cable or cylinder. The "wake-oscillator" models developed by a number of investigators (see Appendix D) are also based upon the hypothesis of a fluid damping or reaction force that is exactly

out-of-phase with the cylinder's velocity. It is possible to deduce the reaction effect of the fluid from the measured force coefficients by means of the equations developed in Appendix E (see also references 3 and 6) as

$$C_{RE} = C_R \sin\phi_1 = -C_{mh} \sin\epsilon. \tag{2.5}$$

As a further step in comparing the two approaches some typical results are plotted in Fig. 2.8. All of the measurements show the same general pattern of behavior even though some were made with freely vibrating cylinders in a wind tunnel and some were made with cylinders that were forced to vibrate in water.

The remaining force components, the added mass and the fluid inertia, can be obtained from the equations given in references 3 and 6 and Appendix E when the force coefficients and the structural parameters of a cylindrical structure and its mountings (i.e., internal damping, natural frequency) are known. Detailed and related discussions of the forces and displacements that result from lock-on are given by Sarpkaya (1) and Griffin (3).

Not only are the unsteady forces amplified as shown in the preceding figures but the steady drag loads also are increased substantially as a result of vortex-excited oscillations. Sarpkaya (12) has measured steady drag coefficients as high as $C_D = 3.1$ for a cylinder vibrating in water at a displacement of $2Y_{MAX} = 1.7$. This represents an increase of nearly a factor of *300 percent* from the drag on a stationary cylinder, i.e. $C_{DO} = 1.1$ in this case. Griffin, Skop and Koopmann (15) found that the drag coefficient was increased by as much as a factor of 1.8 from the stationary cylinder case ($C_{DO} = 0.9$) for their experiments plotted in Figs. 2.2 and 2.7. The steady drag amplification on circular cross-section cylinders due to vortex-excited oscillations is plotted in Fig. 2.9. The solid line on the figure is a least-squares fit to the data points (see Section 4.1).

The static deflection at the tip of a flexible cantilever that experienced resonant cross flow oscillations in water (16) is plotted in Fig. 2.10. The drag coefficient on the vibrating flexible cylinder was

estimated to be as large as $C_D = 2.12$, an amplification of *230 percent* from the drag measured when the cylinder was restrained. This is comparable to the drag amplification measurements that are plotted in Fig. 2.9.

2.3 Coherence of Shedding due to Lock-on. An important consequence of lock-on between the vortex and vibration frequencies is the greatly increased coherence or correlation of the vortex shedding along the length of the structure or cable. Above a threshold cross flow displacement amplitude (typically $\bar{Y}/D = 0.05$ to 0.1) the shedding is in phase along the length of the cylinder or cable and the wake is nearly two-dimensional even at large Reynolds numbers. Koopmann (17) and Toebes (18) in experiments at low and high Reynolds numbers, respectively, were among the first to investigate the increased coherence of the shedding that accompanies lock-on. Koopmann's experiments were limited to Reynolds numbers below 300 but his flow-visualization photographs clearly showed that the vortex shedding was in phase along the vibrating cylinder when the cross flow displacement amplitude was above $2\bar{Y}/D = 0.1$. Toebes' experiments were conducted at much larger Reynolds numbers (Re $\sim$ 68,000), but detailed wake and pressure correlation measurements showed clearly that lock-on was accompanied by increased coherence of the shedding along the cylinder. The magnitude of the cross correlation function was reduced to values below unity only by the effects of turbulent fluctuations in the wake, and the sign of the cross correlation measured along the cylinder indicated that the shedding was in phase for distances up to seven and one-half diameters when the displacement amplitude was above $2\bar{Y}/D = 0.16$. The results of these studies were limited by the relatively small length/diameter ratios, L/D = 7.5 to 12, in the experiments. Novak and Tanaka (19) and Howell and Novak (20) also have investigated the effects of turbulence in the incident stream on the correlation effects that accompany lock-on. Smooth flow (low turbulence) experiments were conducted by them to provide a baseline for comparison with the effects of various kinds of turbulence introduced into the incident flow. Blevins and Burton (21) have developed an empirical model for predicting the vortex-excited resonance, and this model takes account of the variation in correlation length at small displacement amplitudes.

Detailed investigations of the spanwise coherence that accompanies lock-on were made recently by Ramberg and Griffin at NRL (22,23). These experiments were conducted to investigate the wakes of vibrating cables as part of the overall program to develop the semi-empirical "wake-oscillator" model for predicting the cross flow response of flexible cables (see Appendix D). The spanwise correlation coefficient ρ_{AB} measured between two hot-wire probes in the wake of a vibrating cable is plotted in Fig. 2.11. There the normalized cross correlation function (correlation coefficient) for two periodic signals, measured at the spatial displacement Δz, is given by

$$\rho_{AB}(\Delta z) = \frac{\frac{1}{T}\int_0^T u_A(z,t)\,u_B(z+\Delta z,t)\,dt}{\sqrt{\frac{1}{T}\int_0^T u_A^2(z,t)\,dt}\;\sqrt{\frac{1}{T}\int_0^T u_B^2(z+\Delta z,t)\,dt}} \tag{2.6}$$

where u_A and u_B are the fluctuating velocity signals at probes A and B in the near wake of the cable (22,23). The correlation coefficient ρ_{AB} can also be defined in terms of the pressure fluctuations measured at two locations at varying displacements along a cylinder (19). Both probes were positioned above the cable so as to measure vortices of like sign, and one probe was moved in a direction parallel to the cable which was vibrated at several displacement amplitudes. The results shown in the figure correspond to vibration frequencies equal to 90 percent of the Strouhal frequency f_s.

There are three distinguishing characteristics of the correlation in vortex shedding along the cable (22). The shedding is in phase along the cable's half-wavelength as shown by the constant *sign* of the correlation coefficient ρ_{AB}. When the moveable probe was traversed past the node of the cable, a change in sign of ρ_{AB} was observed. The *degree* of the correlation was determined by the maximum value of ρ_{AB} (relative to unity) along the cable and the *extent* of the correlation was defined as the length along the cable that ρ_{AB} was equal to its maximum constant value. Typically it was observed that the $\rho_{AB,MAX} \approx 0.90$ to 0.96 for the frequencies that correspond to vortex-excited oscillations, $f \lesssim f_s$ as shown in Table 2.5. The vortex shedding was fully correlated in *degree* and *extent* over most of the half-wavelength of the cable (L = 12 to 14 D) where the displacement amplitude was greater than a threshold of $\overline{Y} = 0.05$ to 0.1D.

Table 2.5. The degree of correlation (denoted by the maximum value of the correlation coefficient ρ_{AB}) in the wake of a vibrating cable; from reference 22.

Reynolds number = 1300		
Frequency ratio, f/f_s	Displacement amplitude, $2\bar{Y}/D$	Degree of correlation, $\rho_{AB,MAX}$
0.9	0.1	0.89
	0.2	0.94
	0.3	0.96
	0.4	0.96
	0.5	0.92
	0.6	0.92
1.0	0.1	0.88
	0.2	0.96
	0.3	0.96
	0.4	0.97
	0.5	0.97
	0.6	0.96

A further study of the coherence of the vortex shedding in the wake of a flexible cable was conducted by Ramberg and Griffin (23). It was found from spectral analysis of the vortex shedding that the component of the fluctuating pressure or velocity at the cable frequency was 15 to 20 times the component at the Strouhal frequency. The spanwise correlation coefficient ρ_{AB} attained values comparable to those shown in Table 2.5, as shown in Fig. 2.12. Note that magnitude of the spectral component C_n in Fig. 2.12 follows the distribution in displacement amplitude along the cable; this and other similar observations suggest that predictive models for vortex-excited oscillations can be correctly based upon local conditions, i.e. lift and drag forces, so long as the vortex and vibration frequencies are *locked-on*. As a practical matter it is reasonable to assume that at large displacement amplitudes the vortex shedding is coherent in *degree and extent* between nodal points on a vibrating flexible structure. As a nodal region is traversed lengthwise there is a 180 degree phase shift; the vortex shedding is again coherent in degree and extent but is shifted in phase from neighboring sections of the cable. The steady and unsteady hydrodynamic forces (drag, excitation, damping, etc.) vary with local displacement amplitude and are not constant over the half wave length of the cable.

Similar findings were obtained by Novak and Tanaka (19) and Howell and Novak (20) for experiments conducted with cylinders vibrating in smooth flow. Results similar to those in Fig. 2.11 were

obtained (19) when the cross correlation ρ_{AB} was measured between the signals from pressure taps at various spacings along a circular cylinder. When the complications of various types of turbulence and boundary layer profiles were added to the case of a low-turbulence uniform flow, Howell and Novak found that the displacement response of the cylinder was largely independent of the flow characteristics *if the structural damping was sufficiently small to allow lock-on.*

As the damping ratio ζ_s was increased, the displacement response of the flexibly-mounted cylinders became susceptible to the characteristics of the flow incident to the cylinder. The correlation coefficient at the pressures measured between two taps on the cylinder is plotted in Fig. 2.13. The cylinder employed during the experiments was a pivoted rigid rod of aspect ratio L/D = 10 in a deep boundary layer, but the results are very similar to those plotted in Figs. 2.11. In addition to the correlation profiles, Howell and Novak measured the cross flow displacement amplitudes as a function of structural damping (ζ_s = 0.01 to 0.11) and obtained results in various types of boundary layer (shear flow) environments. The measured amplitudes compare very well with those plotted in Fig. 2.2, and full lock-on was observed for the cylinder with ζ_s = 0.01 and $Y_{EFF,MAX} \approx 0.5$. This case is plotted in Fig. 2.14. These findings further confirm that flexible cylindrical structures and cables with small reduced damping ζ_s/μ will be vulnerable to resonant vortex-excited oscillations even if the incident flow is nonuniform (as discussed in Section 2.7).

A number of computer codes, prediction models and design procedures have been developed on the basis of the results just discussed. It has been found that local displacement amplitudes and forces can be predicted for flexible structures and cables from empirical data that are measured in experiments conducted with rigid cylinders, so long as the condition of lock-on is met and the frequency ratios f/f_s (or reduced velocities V_r) and displacement amplitudes are matched appropriately in the two cases.

2.4 Reynolds number effects. The overall pattern of cable and cylinder response described elsewhere in this section of the report is typical of measurements in water, air and similar fluids at all Reynolds number where vortex shedding takes place. Few results at large Reynolds numbers are available,

however, except in the case of in-line oscillations. These results are discussed by King (2). It was found from the experiments conducted by King that full-scale results at high Reynolds numbers could be modelled in small scale laboratory experiments when the reduced velocity V_r and the reduced damping k_s of the two systems were the same. This point is discussed at greater length in Section 4.3. The limited results that are available suggest that Reynolds number effects are of secondary importance if the critical reduced velocity is exceeded and the structural damping is small enough to allow excitation of a flexible cylinder or cable into resonant cross flow oscillations.

The inverse of the reduced velocity V_r or the Strouhal number corresponding to the peak vortex-excited displacement is plotted as the solid line in Fig. 2.15, adapted from the results of Wootton (24). The conditions span the critical regime near Re = 10^5 to 10^6, and little influence of the critical Reynolds number is shown. For the results in the figure, the shedding frequency f_s was locked onto the natural frequency f_n of the cylinder; the dashed line represents the value of St corresponding to the initiation of lock-on. It is likely that conditions such as shear gradients, surface roughness, and inclination to the flow are of greater importance than the Reynolds number.

In order to consider the effects of Reynolds number on vortex-excited oscillations, a universal Strouhal number — Reynolds number correlation was developed for the case of cross flow lock-on (25,26) which had not been considered in previous studies of wake similarity (27). This universal Strouhal number (or non-dimensional frequency scale) is valid at subcritical and supercritical Reynolds numbers (or non-dimensional flow velocities). The formulation has been verified for stationary two-dimensional bluff bodies with fixed and free separation points, vibrating bluff structures, and bluff cylinders in confined flow passages and at large yaw angles to the incident flow. The Strouhal number $St^* = f_s d'/V_b$ is based upon the characteristic frequency of the wake, f_s; the wake width d' at the end of the vortex formation region; and the mean velocity V_b in the region where flow separation takes place. The usual pressure drag coefficient C_D, the vortex shedding frequency, and the base pressure coefficient C_{pb} are also related by means of an inverse dependence between St^* and a wake drag coefficient $C_D^* = C_D/(d'/d)K^2$, where $K = (1 - C_{pb})^{1/2}$. Here d' is the width of the separated vortex wake and d is a characteristic lateral dimension of the structure.

The Strouhal number St^* is plotted against the wake Reynolds number $Re^* = V_b d'/\nu$ in Fig. 2.16 and the legend for the data is given in reference 26. The results span five decades of the Reynolds number, from $Re^* = 10^2$ to 10^7, except for the critical regime near $Re^* = 10^6$. The data for St^* encompass both *stationary and vibrating bluff cylinders* and bodies with blunt trailing edges, both yawed and normal to the incident flow. There is some Reynolds number dependence at the lowest Reynolds numbers, as is the case for the classical St vs. Re relationship, but only a slight dependence of St^* upon Re^* over the remainder of the subcritical range below $2(10^5)$.

The inverse dependence between St^* and the drag coefficient C_D^* is plotted in Fig. 2.17 to demonstrate the universal drag coefficient versus Reynolds number dependence. The solid line corresponds to a prediction (26) of the drag coefficient, which is in excellent agreement with a representative sampling of data points from experiments conducted at NRL and elsewhere. There is a universal correlation between the Strouhal number St^*, the Reynolds number Re^*, and the flow-induced drag coefficient C_D^* over the entire range of flow conditions where vortices are shed.

2.5 Yaw or inclination effects. Yawed cylindrical structures and cables are those which are inclined forward or backward in the plane of the incident flow. Many practical ocean engineering structures are inclined rather than normal to the incident flow; these include cables, raked marine piles and braced frame members of jacket structures. Two recent studies (10,28) have considered the effects of yaw upon the wakes of stationary and vibrating flexible cylinders. King (10) has studied the effect of yaw angle upon the criteria for the onset of vortex-excited oscillations and upon the steady drag forces acting on the structure. His study also includes a complete survey of previous studies on the subject through 1975. More recently, Ramberg (28) has completed a detailed study of the combined effects of inclination and finite length (end conditions) on the vortex wakes of stationary and vibrating cylinders. Included in this study were the effects of yaw angle on the drag and pressure forces on stationary cylinders and on the boundaries of the lock-on range for vibrating cylinders. The experiments of King and Ramberg covered the Reynolds number range from Re = 500 to $2(10^4)$.

Several conclusions were drawn from these investigations. Among the most important of King's findings was that yawing the structure *provides no protection against vortex-excited oscillations*, and sustained oscillations both in line and cross flow were recorded for yaw angles up to $\theta = 45°$ both into and away from the incident flow. The cylinder response was virtually the same whether the cylinder was inclined into or away from the flow, and a typical example (for inclination into the flow) is given in Fig. 2.18. There the reduced velocity V_r is based upon the normal component of the incident flow, $V \cos \beta$, where β is the angle between V and a plane that is normal to the axis of the structure†. The lower peak displacement amplitudes again correspond to larger values of the reduced damping k_s. The yawed flexible cylinder results are plotted in Fig. 2.2 and are indistinguishable from the displacement amplitudes measured at normal incidence. The critical reduced velocities for the onset of in line and cross flow oscillations were once again found to be $V_r = 1.2$ and $V_r = 3.5$ to 5, with the appropriate velocity term being $V \cos \beta$. Similar results were obtained during the DTNSRDC towing channel experiments discussed in Section 3.2. A marine cable that was inclined at an angle $\beta = 30°$ underwent large cross flow strumming displacement amplitudes (29), and the shedding was completely locked on to the resonant vibrations.

King also made a detailed study of yaw angle effects on the drag coefficient of a stationary cylinder. This aspect of the investigation demonstrated that if the normal component of velocity, $V \cos \beta$, were employed as the velocity scale, then a consistent value of drag coefficient C_D was obtained, and that the value of C_D so obtained was equal to the equivalent value for a cylinder at normal incidence. Ramberg's findings suggest that the drag estimated in this way may be low and somewhat dependent on the experimental arrangement (28).

Ramberg undertook a detailed investigation of the flow around yawed cylinders; the primary objective was an examination of the Independence Principle† and how it can be used correctly. This principle, as noted above, states that the proper velocity scale for characterizing the flow about and forces on bluff bodies is the component of the incident flow normal to the body. One conclusion of

†The use of normal component of velocity is called the "Independence Principle;" this is discussed in further detail later in this section.

Ramberg's investigation was that the Independence Principle is not generally valid for stationary, yawed cylinders. It was found that the variation of the shedding frequency of the vortices deviated substantially from the Independence Principle for yaw angles greater than $\beta = 25°$ to 30°, and that the vortex shedding from stationary cylinders was strongly influenced by the end conditions.

A special case (one of only two) where the Independence Principle was found to apply is for the condition of lock-on between the vortex and the vibration frequencies. A typical example of the results obtained by Ramberg is shown in Fig. 2.19. The bounds for lock-on during cross flow oscillations are plotted for yaw angles up to 50° from normal incidence. The yawed cylinder results are in excellent agreement with comparable experiments performed with a cylinder positioned normal to the incident flow. The region inside the dashed lines and data points corresponds to the lock-on regime. The findings from Ramberg's investigation imply that the various methodologies for predicting vortex-excited oscillations at normal incidence can be applied with resonable confidence to a cylinder at an angle of inclination to the flow. King's findings further suggest that such an extension of the results obtained at normal incidence is valid for flexible cylindrical structures in flowing water.

2.6 Surface Roughness Effects. Another factor influencing the hydrodynamic forces that result from vortex-excited oscillations is the surface roughness of the cable or cylinder. Sarpkaya (30) has measured the unsteady hydrodynamic forces on sand-roughened cylinders forced to vibrate and has compared his measurements to similar experiments with a smooth cylinder. Some typical results for the *total* hydrodynamic force coefficient $C_{T,MAX}$ are plotted in Fig. 2.20. Substantial increases are apparent in the unsteady hydrodynamic force coefficient for the rough cylinder, though additional study is necessary to determine which components of the total force are amplified by the roughness. The resonant effect of lock-on is apparent, however, when the coefficient C_T is plotted against the displacement amplitude $\bar{Y}/D$ as in Fig. 2.21. Once again the peak value of C_T is obtained at $2\bar{Y}/D = 1$ for the different reduced velocities in the lock-on regime. The increase in C_T for the roughened cylinder as compared to a smooth cylinder is readily apparent in Fig. 2.21. The Reynolds number based on the

cylinder diameter was Re $= 5 \times 10^4$, the largest value reached by Sarpkaya. This corresponded to a roughness Reynolds number of $Re_\delta = 500$, where the relationship between Re_δ and Re is

$$Re_\delta = Re(\delta/D). \tag{2.7}$$

Here δ is the average roughness height. Sarpkaya (30) employed a uniform sand roughness on the cylinder and discusses some of the complexities that arise when the roughness is nonuniform and irregular.

Peltzer and Rooney (31) have conducted one of the most complete and up-to-date studies of the effects of shear and roughness on vortex shedding from stationary circular cylinders. The Reynolds numbers for their experiments spanned the range from Re $= 1.6 \times 10^5$ to 3.6×10^5, for smooth and roughened cylinders (roughness $\delta/D = 1 \times 10^{-3}$), and steepness parameters (see Section 2.7) from $\bar{\beta}$ $= 0$ (uniform flow) to $\bar{\beta} = 0.041$. This range of parameters was sufficient to provide both subcritical, critical (or transcritical), and supercritical vortex shedding conditions. Some of the uniform flow baseline conditions for the smooth and rough cylinders are plotted in Fig. 2.22, along with some recent measurements by Buresti and Lanciotti (32) and by Alemdaroglu, Rebillat and Goethals (33). The Strouhal number *St* versus roughness Reynolds number Re_δ plot illustrates the three Reynolds number ranges just mentioned. Szechenyi (34) introduced the idea of roughness scaling to achieve high Reynolds number flows, and found that critical and supercritical flows were reached for $Re_\delta > 200$. The results in Fig. 2.22 are in good agreement with this finding. These results are in good overall agreement with the original supercritical roughness Reynolds number simulation of Szechenyi although the supercritical Strouhal numbers measured by Szechenyi were somewhat higher ($St \sim 0.26$) than those plotted in Fig. 2.22. Sarpkaya's experiments with vibrating cylinders spanned the three regimes and the results at $Re_\delta = 500$ in Fig. 2.21 approach close to, or are in, the supercritical range of Re_δ.

Nakamura (35) has measured the steady drag forces and Strouhal frequencies on rough circular cylinders at supercritical Reynolds numbers, and *has observed strong regular vortex shedding at Re* $\approx$ $4(10^6)$ *and above.* In this Reynolds number range the vortex-excited cross flow displacement amplitude of a rough cylinder *increased substantially* from the corresponding smooth cylinder experiment. This

finding would tend to confirm Sarpkaya's measurements of amplified hydrodynamic forces due to surface roughness in addition to the force amplification due to lock-on. A comprehensive study of the effects of surface roughness on the steady drag forces on stationary cylinders was made by Miller (36) for the case of a stationary cylinder, and another recent report by Hove, et al. also considers this problem in some detail (37).

2.7 Shear (Nonuniform Flow) Effects. The effects of velocity gradients (shear) are difficult to quantify on the basis of available evidence, especially for structures and cables which are vibrating. However, the sparse information that is available suggests that a full-scale cylindrical structure or cable will vibrate at large displacement amplitudes even in the presence of nonuniform flow effects if the reduced damping is sufficiently small and the critical reduced velocity is exceeded. Detailed experiments reported by Howell and Novak (20) and by Kwok and Melbourne (38) give strong evidence that a flexible bluff structure with a circular cross-section will vibrate resonantly at large displacement amplitudes when a turbulent boundary layer type of shear flow is incident upon the cylinder. Kwok and Melbourne measured maximum tip displacements comparable to those in Fig. 2.2 for reduced dampings in the range $k_s = 2$ to 12 ($\zeta_s/\mu \sim 0.5$ to 3).

Stansby (39) investigated the phenomenon of lock-on for the cross flow vibrations of circular cylinders in a linear shear flow and has compared the results to similar experiments in uniform flow. From these experiments Stansby developed empirical equations to predict the bounds for lock-on in a shear flow, based upon the assumption of universal similarity in the wakes of bluff bodies (25,26). However, these results are limited to cylinders with small length/diameter ratios (L/D = 8 to 16), relatively low Reynolds number (Re = 3000 to 10,000) and small displacement amplitudes ($\bar{Y}/D < 0.2$).

A recent paper and a report by Fischer, Jones and King (16,40) describes some problems that were anticipated during the installation of foundation piles for the Shell Oil production platform in the Cognac field of the Gulf of Mexico. The problems stemmed largely from the anticipated vortex-excited oscillations of the piles during two operations: while they were being lowered from a derrick barge into

sleeves in the platform base and while the inserted piles were being hammered into the sea bed. Maximum tip displacement amplitudes (cross flow) of 3.2 to 3.8 m (10.5 to 12.5 ft) from equilibrium were predicted for currents as low as 0.6 m/s (0.31 kt) at the platform site. These large-scale motions were expected to create difficulties while "stabbing" the piles into the sleeves, and they could also increase the risk of buckling and fatigue failures during the pile driving operations.

Experiments were conducted with model piles in three laboratories (40), for both the pile lowering and the pile driving operations. Uniform and nonuniform (shear) flows were modelled in the experiments. The shear parameter that characterizes a nonuniform flow is defined as

$$\bar{\beta} = \frac{D}{V_{REF}} \frac{\Delta V}{\Delta \bar{z}}, \tag{2.8}$$

where V is the magnitude of the incident flow velocity and $\bar{z}$ (in this case) is the depth of the water. The reference value V_{REF} is usually taken as the velocity magnitude at half the distance along the cable or structure, although the maximum value from a velocity profile is sometimes used. For the small-scale experiments reported by Fischer et al (40) the shear parameter was $\bar{\beta} = 0.01$ which matched the actual Cognac site value at depths between 100 m (330 ft) and 250 m (820 ft).

The results from some typical model-scale experiments are plotted in Fig. 2.24. The tests were conducted with a 1:168 scale model of the large marine piles of diameter $D = 2.1$ m (7 ft). Both the full-scale and the model piles had specific gravities of 1.5. It is clear from the results in Fig. 2.24 that a shear flow with $\bar{\beta} = 0.01$ to 0.015 had virtually no mitigating effect on the peak vortex-excited displacement amplitudes in the cross flow direction. The data plotted in the figure correspond to a free-cantilever flexible beam with no tip mass at the free end. This configuration matched closely the "stabbed" pile before an underwater hammer was attached for driving it into the sea bed. The structural damping of the PVC model in Fig. 2.24 was $\zeta_s = 0.063$ and for a similar stainless steel model the damping was $\zeta_s \approx 0.015$; the two flexible cylinders experienced tip displacement amplitudes of $2\bar{Y} =$ 3D and 4D, respectively. These damping ratios and displacement amplitudes fall well toward the left-hand portion of Fig. 2.2 where hydrodynamic effects are dominant.

It was concluded from a study of the static and dynamic stress levels within the Cognac piles during driving that the large cross flow displacement amplitudes (of the level shown in Fig. 2.24) would triple the stresses from a corresponding stationary 130 m (426 ft) long pile. The apparent steady drag coefficient on the oscillating pile was $C_D = 2.12$; this is an amplification of 230 percent from the drag coefficient ($C_{DO} = 0.93$) when the pile was restrained. A fatigue life of four days was predicted for a stabbed pile (without a hammer attached) when it was exposed to a current of magnitude 0.46 m/sec (0.9 kt). Additional details and assumptions pertaining to the study are discussed in reference 40.

A flag-type or flexible tail fairing type of wake interference device was developed to suppress the cross flow oscillations. Such a device was tested successfully on the model piles, but the particular configuration was chosen because of the nearly unidirectional currents at the Cognac site (40). Few actual problems were encountered during the field installation, but in the case of one pile typical peak-to-peak displacement amplitudes of 3 m (9.8 ft) were measured. The cause of these cross flow oscillations was attributed to alternate vortex shedding.

A program of experiments recently was conducted to assess the effects of shear on vortex shedding from smooth and rough cylinders at large Reynolds numbers (31). The experiments were conducted with a cylinder of aspect ratio L/D = 16 at Reynolds numbers in the range of 1.5 (10^5) to 3 (10^5) in order to assess the minimum shear (as denoted by the shear parameter $\bar{\beta}$ given above) at which the characteristic lengthwise cellular vortex shedding pattern was initiated. An incipient cellular pattern of vortex shedding was observed at the weakest shear gradient, $\bar{\beta} = 0.007$, and persisted in stronger form over the test range to shear levels given by $\bar{\beta} = 0.04$. Most of the test runs, however, were carried out at values of the shear parameter, $\bar{\beta} = 0.007$ to 0.02, which are representative of ocean site conditions. The results obtained by Peltzer and Rooney provide a reasonably extensive data base of circumferential mean pressure and vortex shedding frequencies for smooth and rough circular cylinders at subcritical, critical and supercritical Reynolds numbers.

Peterka, Cermak and Woo (41) are conducting experiments to study the vortex shedding from large aspect-ratio (L/D = 12 to 128), stationary and vibrating circular cylinders and cables in a linear

shear flow. Figure 2.25 shows the Strouhal number based on centerline velocity for L/D = 34, $\bar{\beta}$ = 0.032, and Re = 4000. This figure confirms the existence of two cells at the boundaries and shows a tendency toward a cellular vortex pattern over the central section of the stationary cylinder. Regions with a similar frequency can be identified over a limited distance, but it is not clear that cells with well-defined boundaries exist. When the data from Fig. 2.25 are presented as Strouhal numbers based on the local velocity, the data are grouped around Strouhal numbers of 0.2 to 0.21 (41). The data indicates that some cellular structure occurs but that no clear cell boundaries can be identified in many regions.

Two smoke visualization photographs of the wake of the same cylinder at a Reynolds number slightly below 2000 are shown in Fig. 2.26. The region observed is roughly from the centerline to L = 8D below the centerline where no clear indication of a cell structure was evident from frequency measurements in the wake. The smoke was illuminated by a strobe light that was synchronized with the shedding frequency, and an exposure time long enough to cover about six or seven shedding cycles was used. The periodic structure seen in the smoke pattern along the cylinder length is a result of smoke introduction through equally spaced holes in the base of the cylinder. If a coherent cell shedding at the strobe frequency for seven or eight cycles existed during the exposure time, the result would appear as a banded system as seen in the top photograph. If a cell with a frequency different from the strobe frequency was shedding or if no shedding occurred during the exposure time, the result would look like the bottom photo. However, the photos in Fig. 2.26 were taken at two different times using the same strobe frequency. These results suggest that cells of finite size, but of different frequencies and extent, exist at different times in the wake (41). An inclined pattern of vortex shedding similar to that shown in the top photograph was observed by Stansby (39) for a cylinder with L/D = 16, $\bar{\beta}$ = 0.025 and Re $\approx$ 3000.

The available evidence through 1980 relevant to shear flow effects on bluff bodies has been summarized in an NRL report (42). Additional detailed findings are given in the proceedings of recent International Conferences on Wind Engineering (see references 43 and 44) and in several of the references just cited.

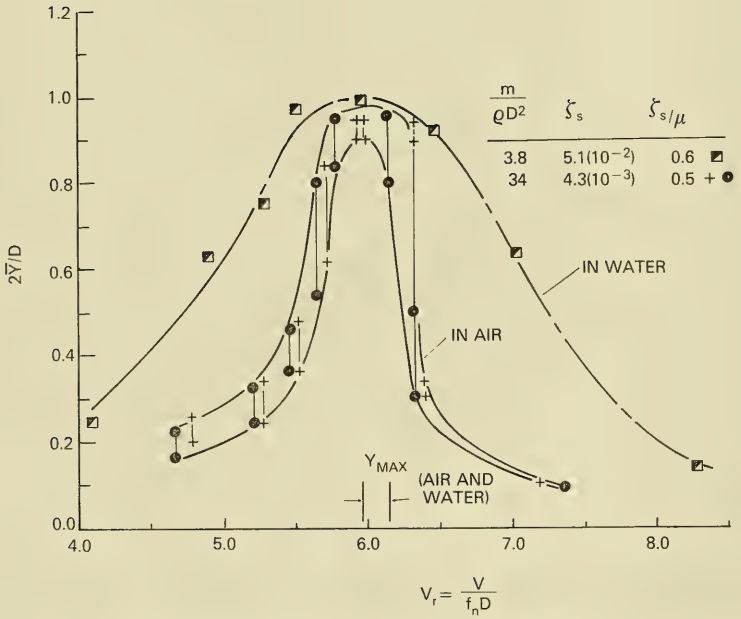

Figure 2.1 The cross flow displacement amplitude $2\overline{Y}/D$ for a circular cylinder plotted against the reduced velocity $V_r = V/f_n D$. Data points denoted by (+,•) were measured in a wind tunnel using a cylinder with a natural frequency f_n = 52 Hz and diameter D = 6.1 mm (4). Data points denoted by (◩) were measured in water using a cylinder with f_n = 2.2 Hz (air), 2.0 Hz (water) and D = 25 mm (5).

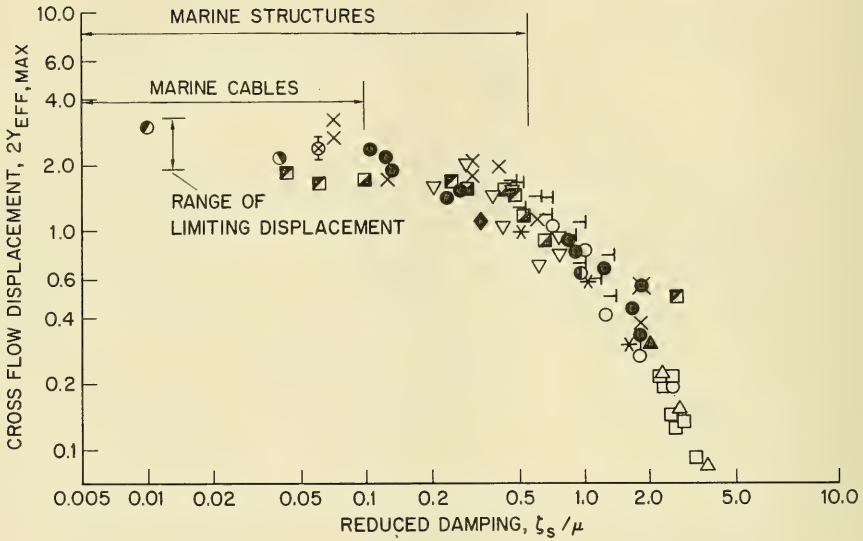

Figure 2.2 Maximum vortex-excited cross flow displacement $2Y_{EFF,MAX}$ of circular cylinders, scaled as in Eq. (2.3), as a function of the reduced damping $\zeta_s/\mu = 2\pi St^2 k_s$. The damping ratio ζ_s (or the long decrement δ) was measured in *still air* for *all* cases shown in the figure. The legend for the data points is given in Table 2.2.

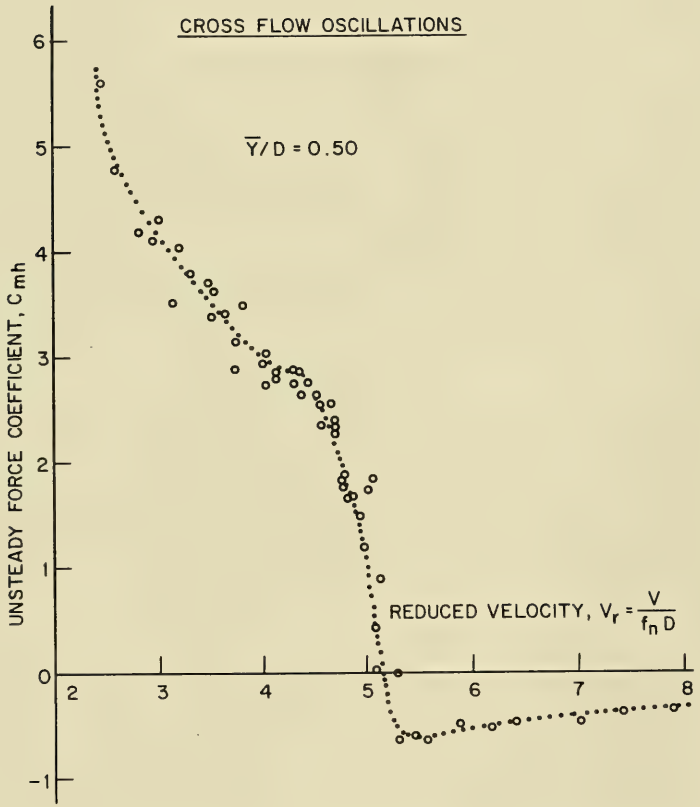

Figure 2.3 The inertia coefficient C_{mh} at the vibration frequency plotted against the reduced velocity V_r for $\overline{Y}/D = 0.5$. The data are from Sarpkaya (12) and were measured in water with uniform, steady fluid motion past a cylinder oscillating normal to the flow. The coefficient C_{mh} was derived from the total unsteady transverse force. Lock-on occurs near $V_r = 5$.

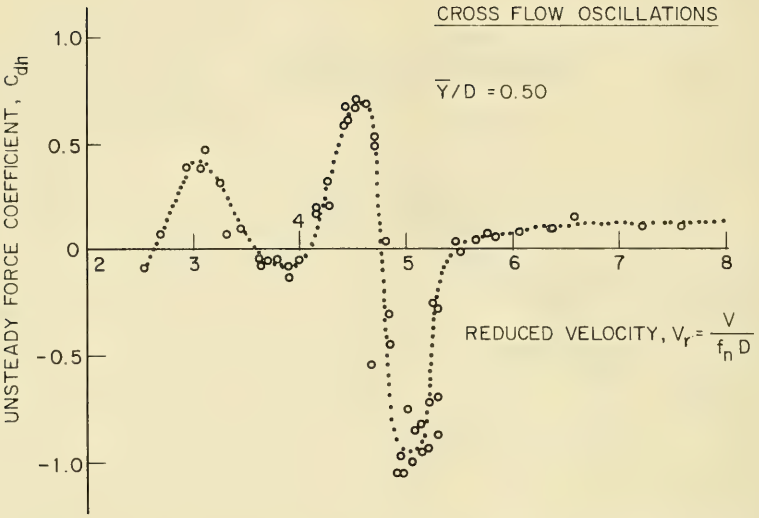

Figure 2.4 The "drag" coefficient C_{dh} at the vibration frequency plotted against the reduced velocity V_r for $\overline{Y}/D = 0.5$. The data are from Sarpkaya (12) and were measured in water with uniform, steady fluid motion past a cylinder oscillating normal to the flow. The coefficient C_{dh} was derived from the total unsteady transverse force. Lock-on occurs near $V_r = 5$.

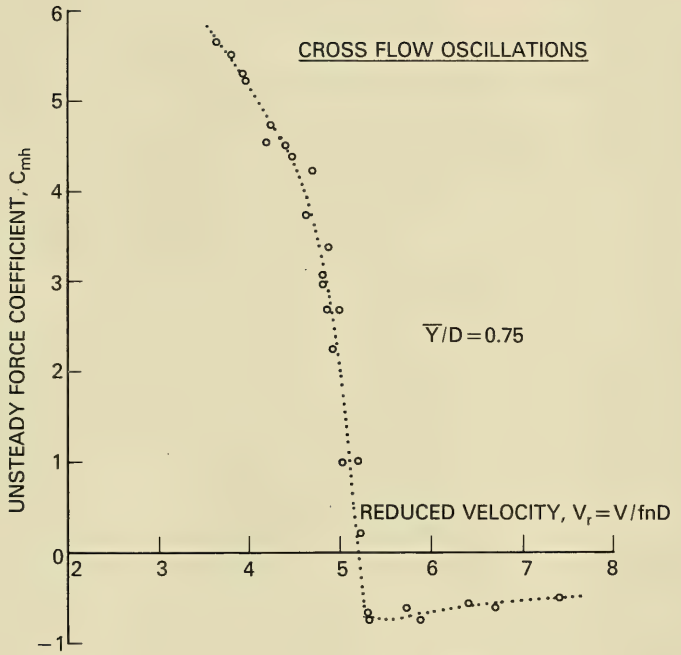

Figure 2.5 The inertia coefficient C_{mh} at the vibration frequency plotted against the reduced velocity V_r for $\overline{Y}/D = 0.75$. The data are from Sarpkaya (12) and were measured in water with uniform, steady fluid motion past a cylinder oscillating normal to the flow. The Coefficient C_{mh} was derived from the total unsteady transverse force. Lock-on occurs near $V_r = 5$.

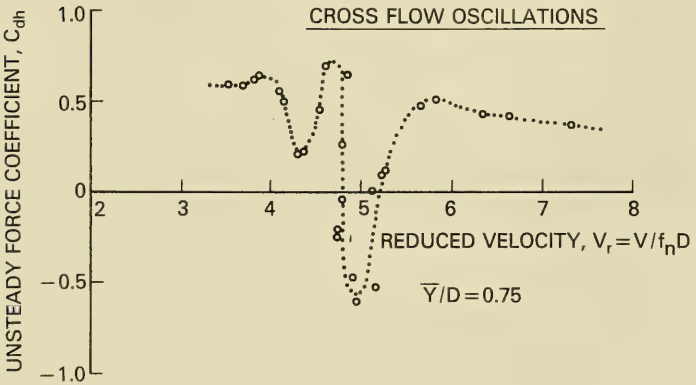

Figure 2.6 The "drag" coefficient C_{dh} at the vibration frequency plotted against the reduced velocity V_r for $\overline{Y}/D = 0.75$. The data are from Sarpkaya (12) and were measured in water with uniform, steady fluid motion past a cylinder oscillating normal to the flow. The coefficient C_{mh} was derived from the total unsteady transverse force. Lock-on occurs near $V_r = 5$.

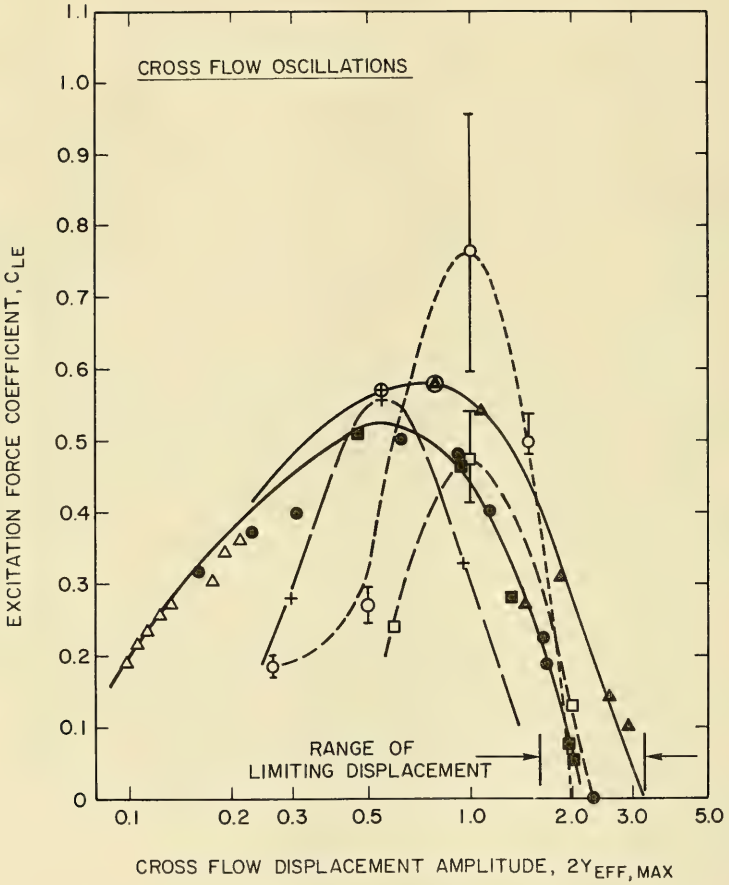

Figure 2.7 The excitation component C_{LE} of the lift force plotted against the vortex-excited cross flow displacement $2Y_{EFF,MAX}$ (peak-to-peak), as in Eq. (2.3). The legend for the data points is given in Table 2.4.

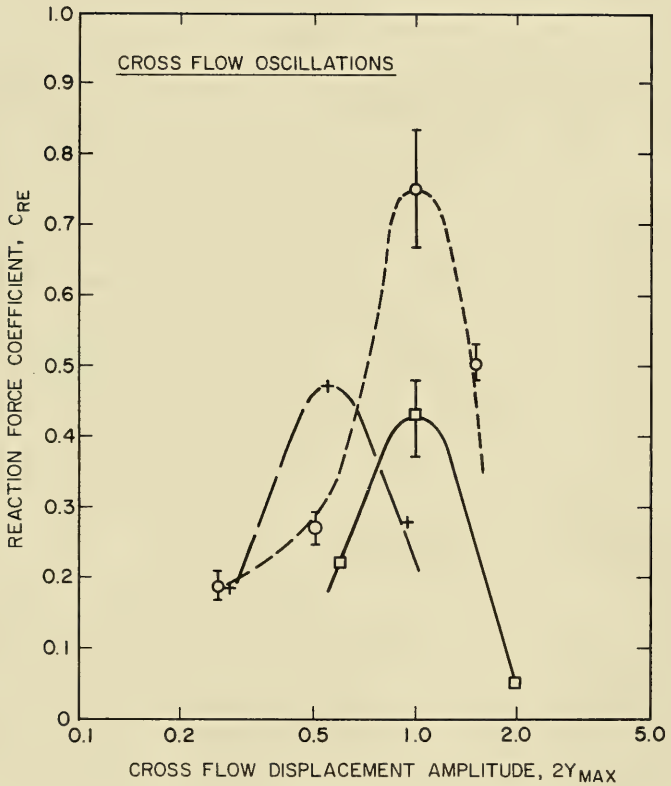

Figure 2.8 The fluid reaction coefficient C_{RE} plotted against the maximum cross flow displacement $2Y_{MAX}$ for a circular cylinder vibrating in uniform flow. Legend for data points: – –, Griffin and Koopmann (4); ——, Mercier (13); --- Sarpkaya (12).

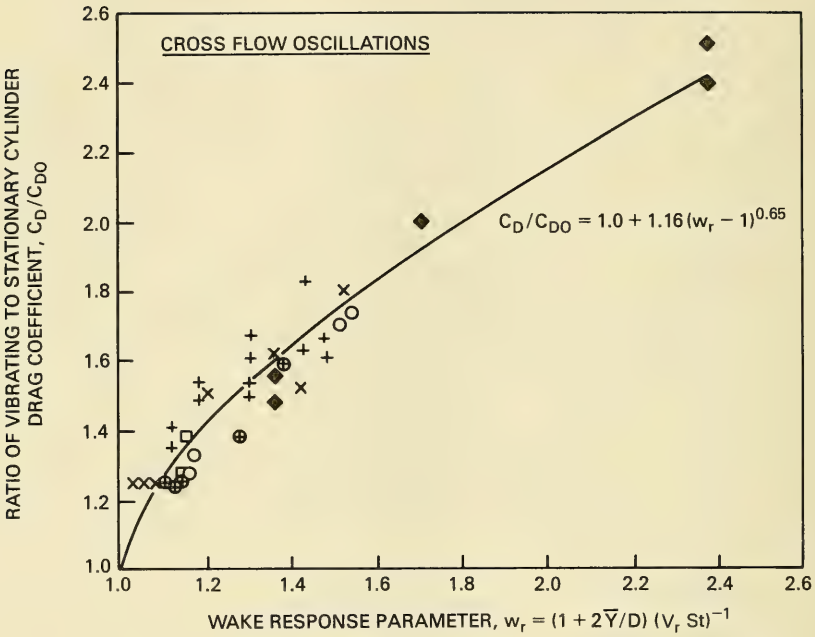

Figure 2.9 The ratio of the steady drag coefficient C_D due to vortex-excited cross flow oscillations and the steady drag coefficient C_{DO} on a stationary circular cylinder plotted against the wake response parameter w_r. Here $2Y/D$ is the peak-to-peak displacement amplitude (D is the diameter of the cylinder), V_r is the reduced velocity and St is the Strouhal number.

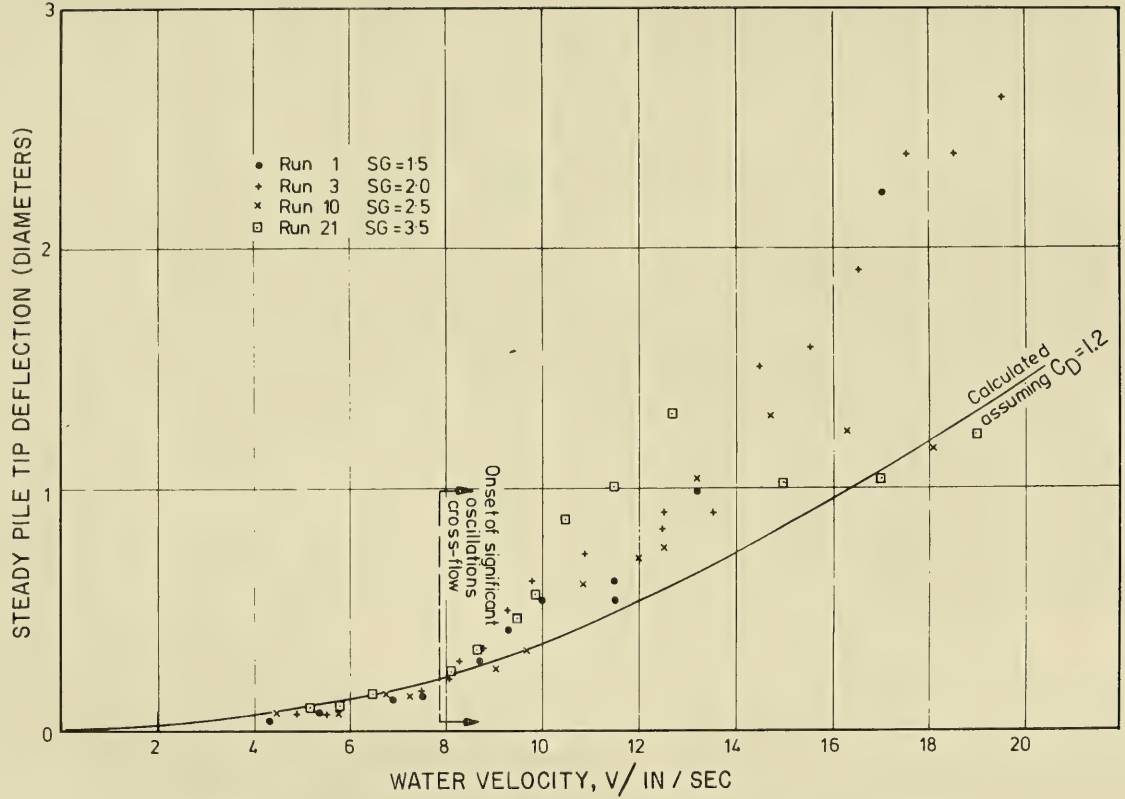

Figure 2.10 Steady drag-induced deflection at the tip of a free-ended cantilever piling. The piling was oscillating as shown, for example, in Fig. 2.24; from King (16).

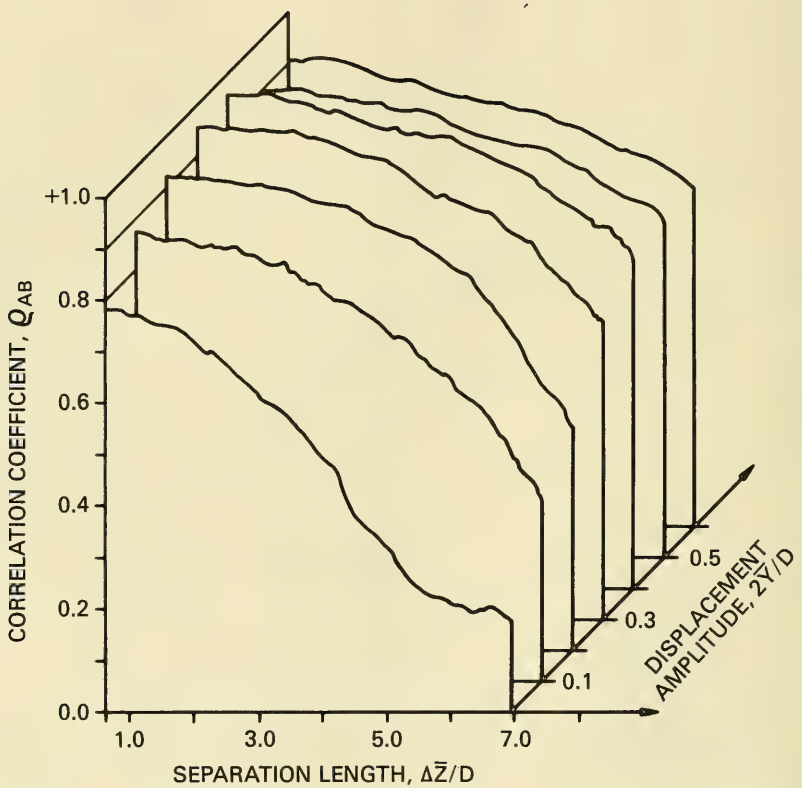

Figure 2.11 Spanwise correlation coefficients ρ_{AB} for the velocity signals measured in the wake of a vibrating cable at a Reynolds number of 1300; from reference 22. The spanwise separation between the two measuring probes is given by $\Delta\ \bar{Z}/D$ and the vibration displacement amplitude by $\bar{Y}_{MAX}/D$. Vibration frequency equal to 90 percent of the Strouhal number frequency f_s.

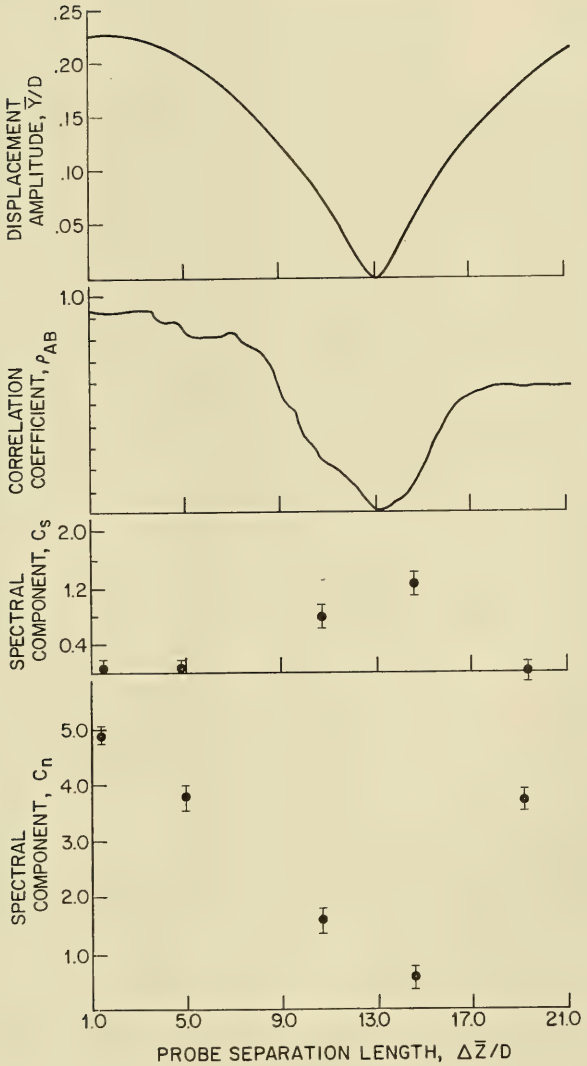

Figure 2.12 Distribution of displacement amplitude $\overline{Y}/D$, magnitude of the spanwise correlation coefficient ρ_{AB}, and the spectral content of the vortex shedding at the vibration frequency $f(C_n)$ and at the Strouhal frequency $f_s(C_s)$; from reference 23. The spanwise separation between the measuring probles is given by $\Delta\overline{z}/D$ and the variation displacement amplitude by $\overline{Y}/D$. Vibration frequency equal to 86 percent of the Strouhal frequency f_s. Reynolds number = 610.

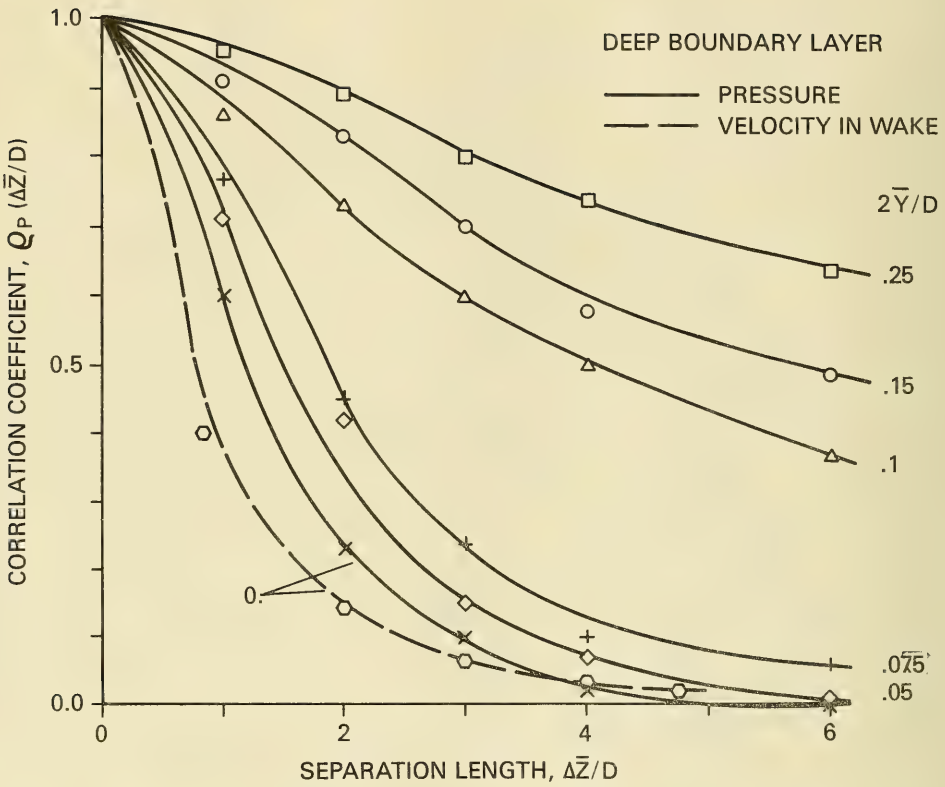

Figure 2.13 Spanwise correlation coefficient R_p between the fluctuating pressures measured on a vibrating pivoted rigid cylinder in a deep boundary layer flow; from reference 20. The peak-to-peak tip displacement amplitude of the cylinder is given by $2\bar{Y}/D$ and the spanwise separation between the pressure taps is given by $\Delta\bar{z}/D$. Reynolds number = 75,000.

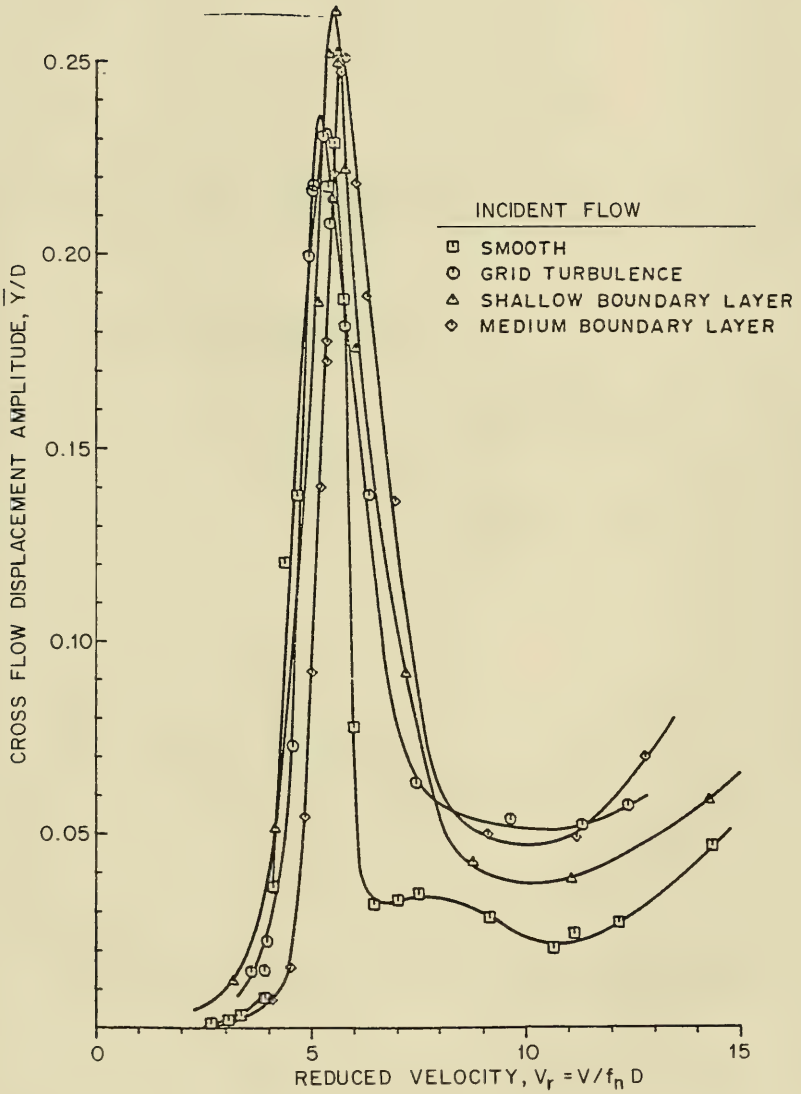

Figure 2.14 Peak cross flow displacement amplitude $\overline{Y}/D$ (root-mean-square of $\overline{Y}$) plotted against reduced velocity V_r for a flexibly-mounted circular cylinder in uniform and sheared incidents flows; from Howell and Novak (20). Structural damping ratio $\zeta_s = 0.01$; aspect ratio $L/D = 10$. The various types of incident wind flows are given by the legend. The figure was provided by Dr. John F. Howell, University of Bath, England.

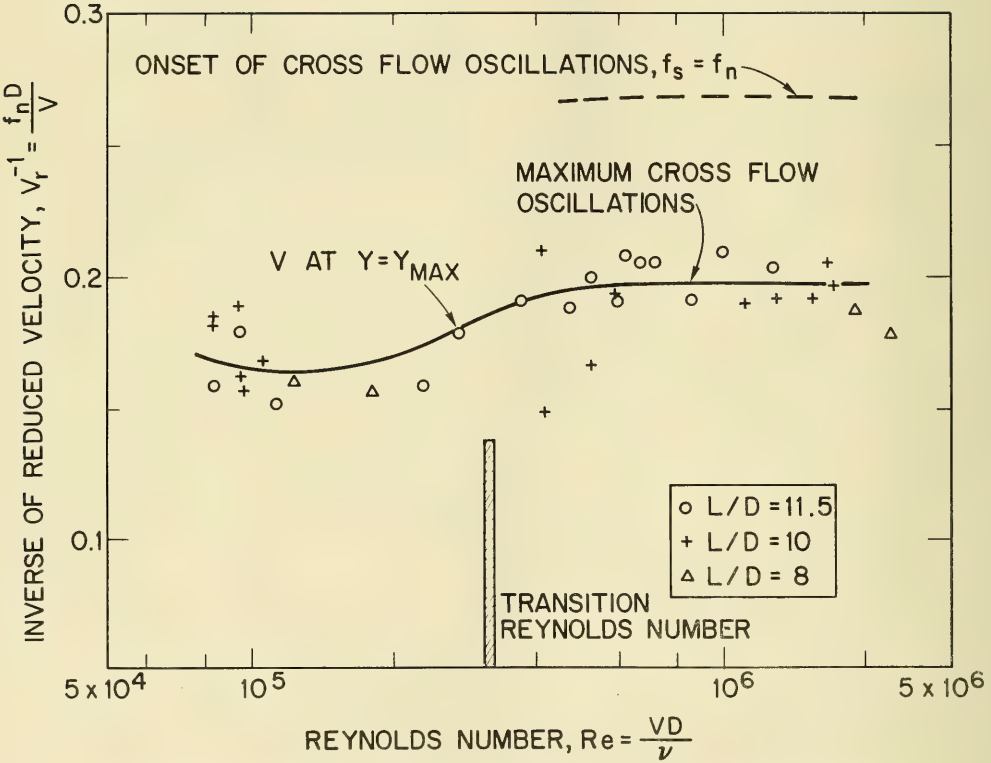

Figure 2.15 Inverse reduced velocity V_r^{-1} for maximum displacement amplitudes plotted against the Reynolds number for roughened cylinders. The inverse of V_r is the Strouhal number based on f_n. Maximum peak displacement, ——; onset of vortex-excited oscillations ---; from Wootton (24).

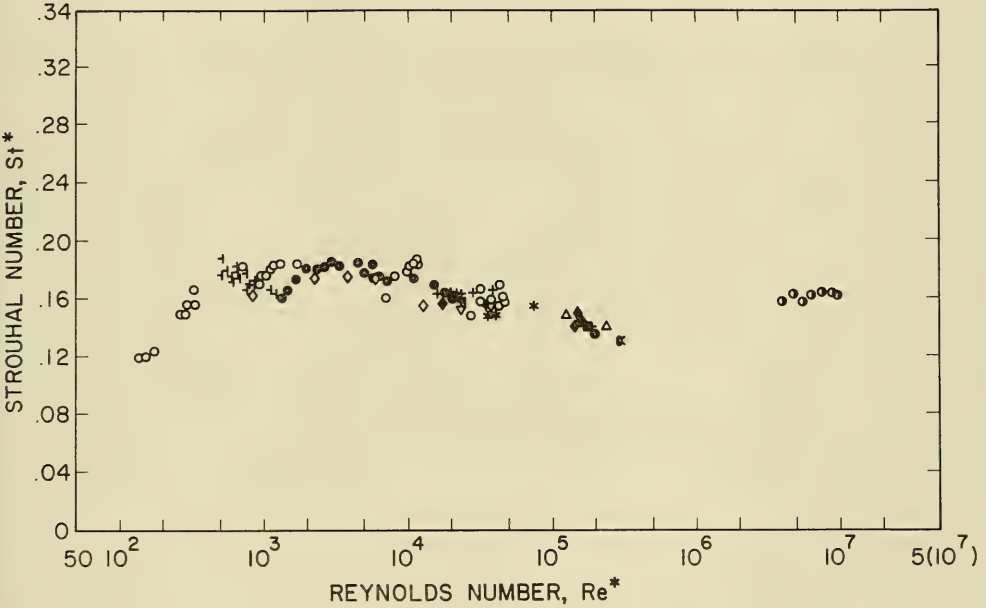

Figure 2.16 Universal Strouhal number St^* plotted against the wake Reynolds number Re^* (see Section 2.4). A detailed legend for the data in given in reference 26.

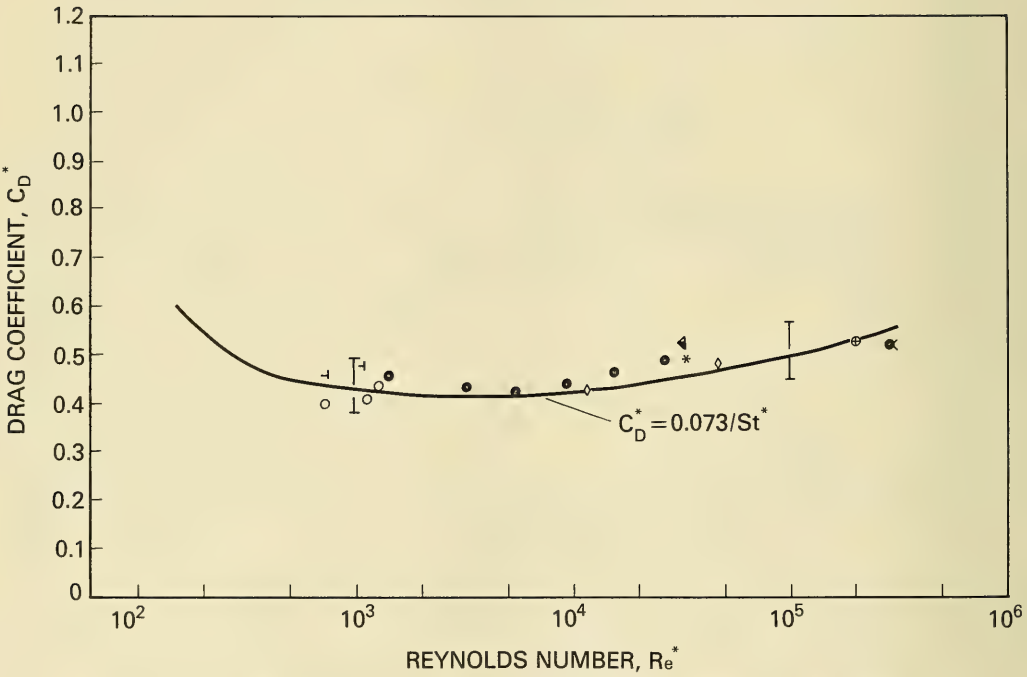

Figure 2.17 The universal wake drag coefficient C_D^* plotted against the wake Reynolds number (see Section 2.4). A detailed legend for the data points is given in reference 26.

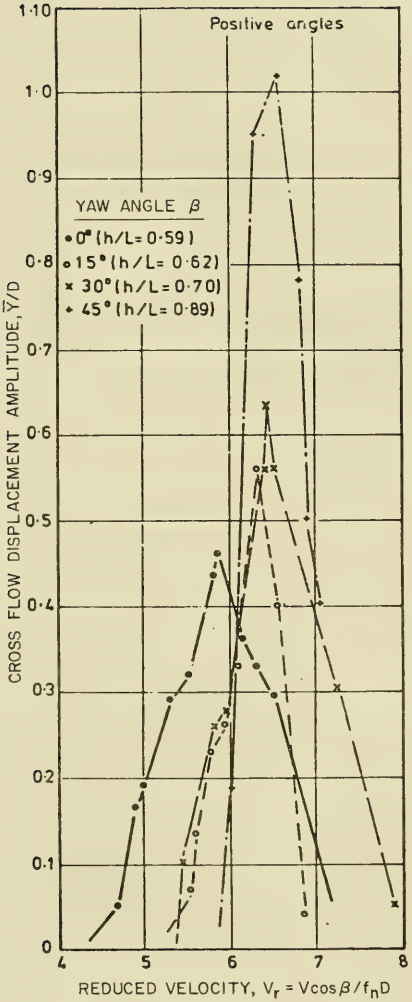

Figure 2.18 The cross flow induced displacement amplitude $\bar{Y}/D$ for flexible, yawed cylinders in uniform flow plotted against the reduced velocity V_r; from King (10). The reduced velocity is based upon the component of the incident flow normal to the cylinder, $V \cos \beta$, where β is the yaw angle. The Reynolds number of the experiments was Re $\approx 10^4$.

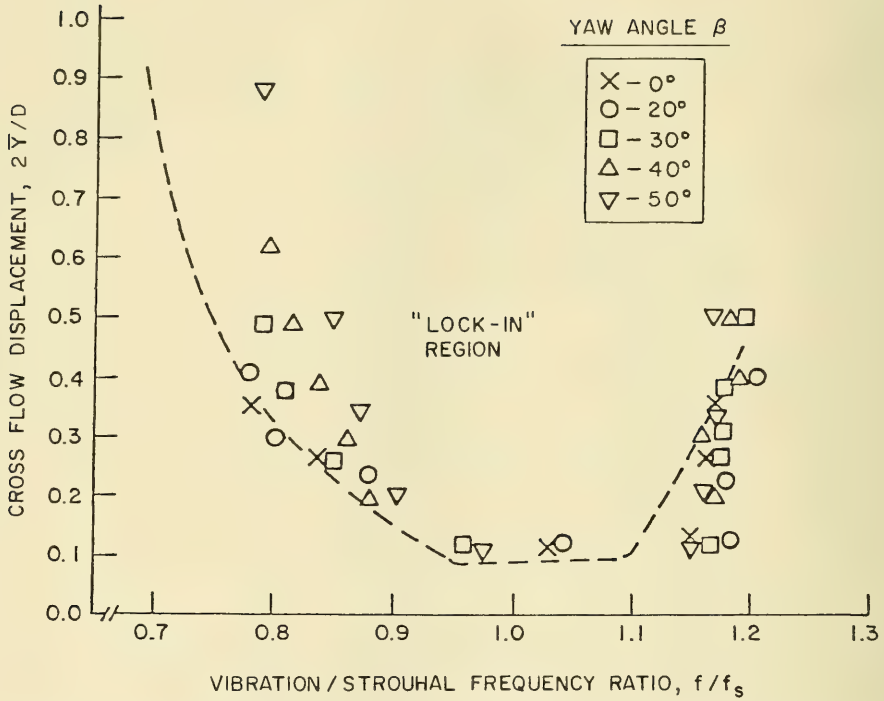

Figure 2.19 Lock-on boundaries (in terms of the cross flow displacement amplitude $2\bar{Y}/D$) plotted against the ratio of vibration and Strouhal frequencies; from Ramberg (28). The Strouhal frequency f_s was estimated from the cosine law relation $f_s = 0.21\ V \cos \beta / D$. *Lock-on* occurs *inside* the area bounded by the data points and dashed lines, and the latter correspond to the case of flow normal to the vibrating cylinder.

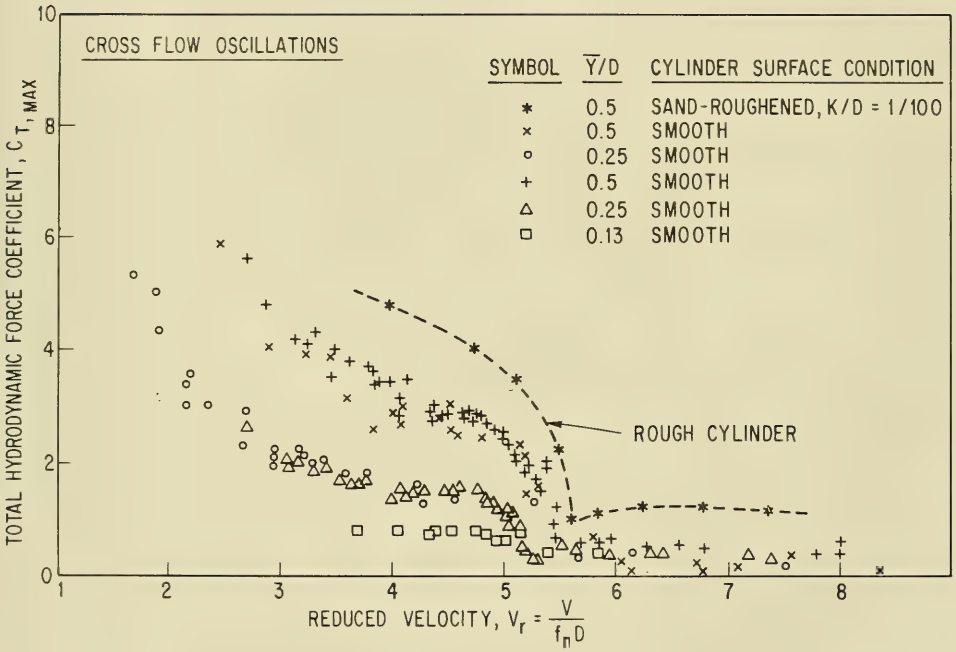

Figure 2.20 Total unsteady transverse force coefficient at the locked-on vibration frequency (Force/1/2/$\rho V^2 DL$). $C_{T,MAX}$, measured on smooth and rough circular cylinders vibrating in the cross flow direction, plotted against the reduced velocity V_r; from Sarpkaya (20). The measurements were made under the same conditions as in Fig. 2.3 through 2.6, and lock-on occurs near $V_r = 5$.

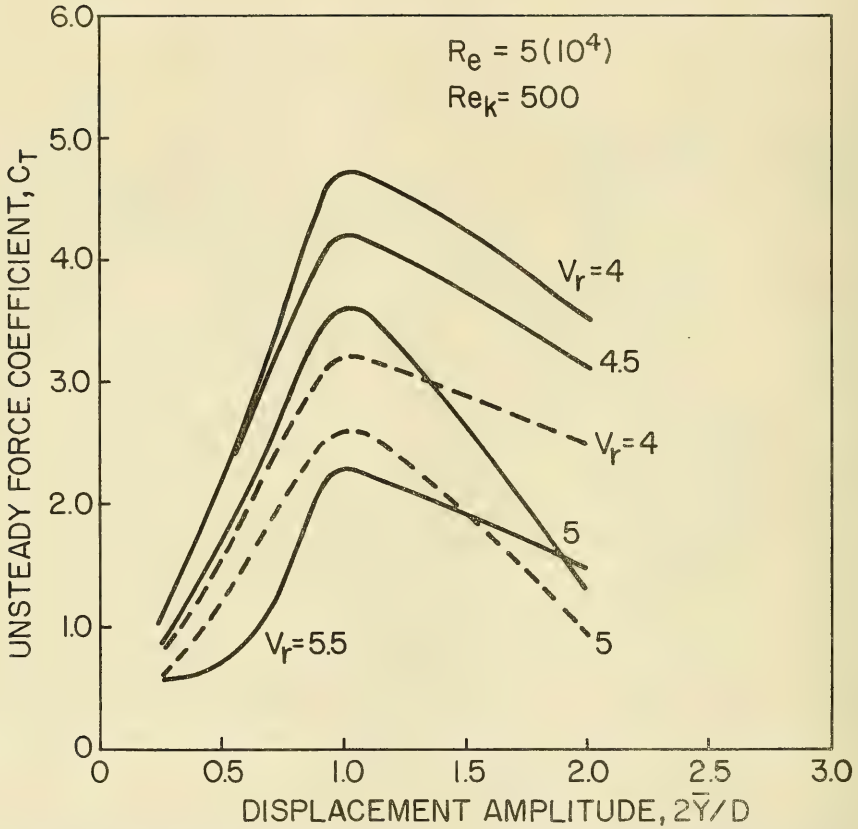

Figure 2.21 Total unsteady transverse force coefficient C_T, measured on smooth and rough circular cylinders vibrating in the cross flow direction plotted against the displacement amplitude $2\bar{Y}/D$, from Sarpkaya (30). Legend for data points: ——, rough cylinder; -----, smooth cylinder.

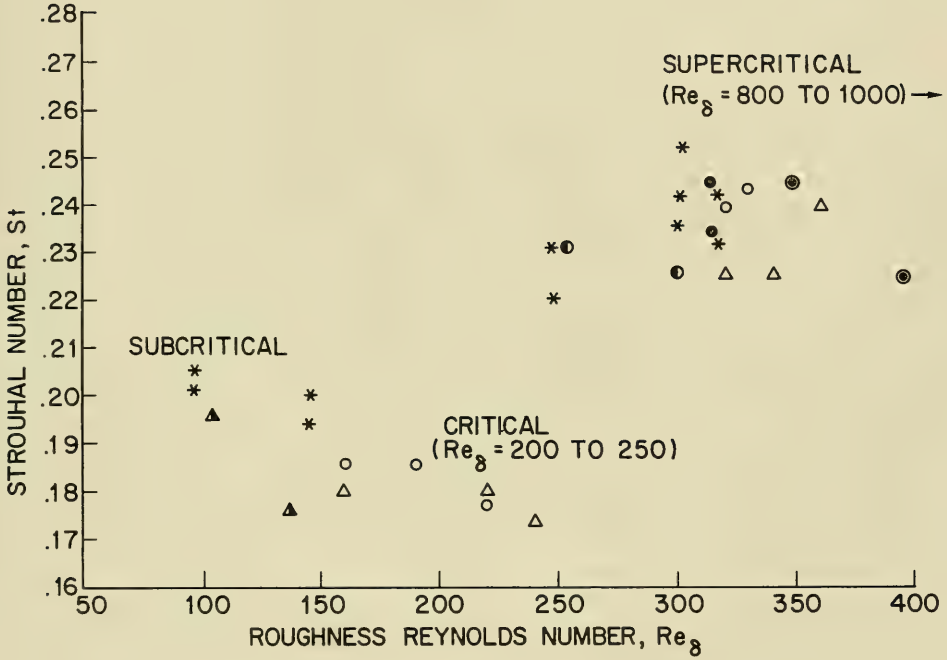

Figure 2.22 Strouhal number $St = f_s D/V$ plotted against the roughness Reynolds number $Re_\delta = V\delta/\nu$. Here δ is the cylinder surface roughness. Legend for data points:

Peltzer and Rooney (31):

○ Rough ($\delta/D = 10^{-3}$)
△ Rough, low turbulence = .03%

Buresti and Lanciotti (32):

*Rough ($\delta/D = 10^{-3}$)
●Rough ($\delta/D = 3.5 \times 10^{-3}$)

Alemdaroglu, Rebillat and Goethals (33):

▲ Rough ($\delta/D = 10^{-3}$)
◐ Rough ($\delta/D = 5 \times 10^{-3}$)
◉ Rough ($\delta/D = 3.4 \times 10^{-3}$)

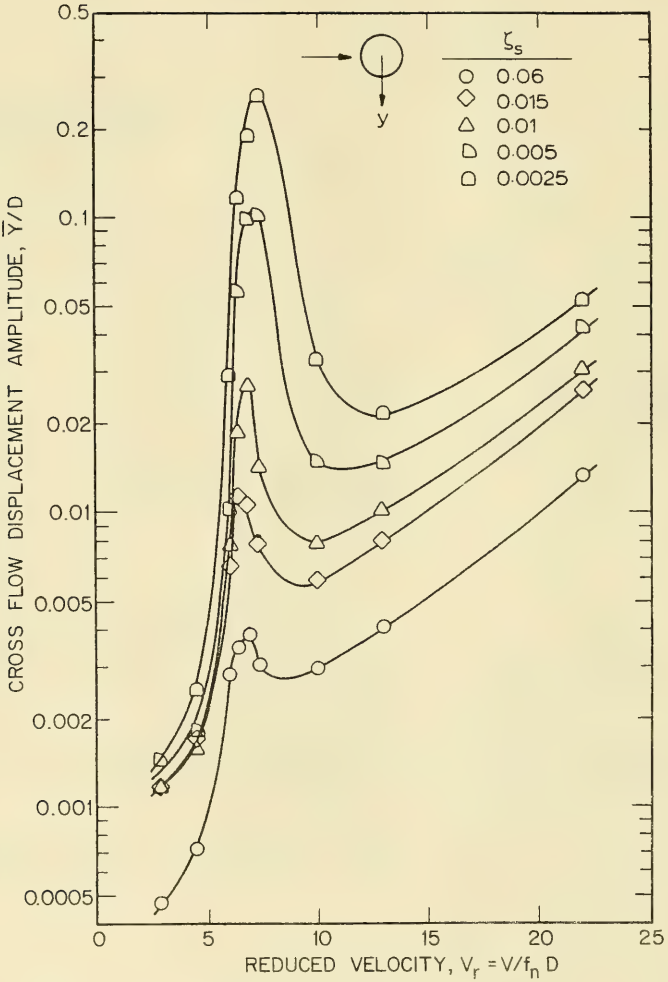

Figure 2.23 Peak cross flow displacement response $\overline{Y}/D$ (standard deviation of $\overline{Y}$) plotted against reduced velocity $V_r = V/f_n D$ for a model circular cylinder in a turbulent boundary layer; from Kwok and Melbourne (38). The structural damping ratio ζ_s of the rigid pivoted model was varied as shown on the figure. The characteristic flow velocity V was measured at the tip of the cylinder, of aspect ratio $L/D = 9$. The figure was provided by Dr. K.C.S. Kwok, University of Sydney, Australia.

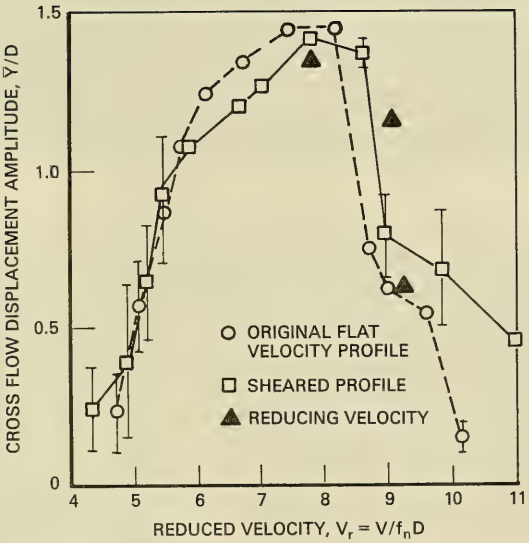

Figure 2.24 Measured peak cross flow displacement amplitude $\overline{Y}/D$ plotted as a function of the reduced velocity V_r. A slender, fully submerged and cantilevered circular cylinder was employed as the model ($L/D = 52$. $D = 12.7$ mm (0.5 in)) for experiments conducted in uniform ($\overline{\beta} = 0$) and shear ($\overline{\beta} = 0.01$ to 0.015) flows of water. The cylinder was a 1:168 scale model of a full-scale marine pile with the same specific gravity (SG = 1.5), from experiments reported by Fischer, Jones and King (40) and King (16). In the case of the shear flow V is the maximum value in the nonuniform incident velocity profile. The figure was provided by Dr. Warren Jones of the Shell Development Company.

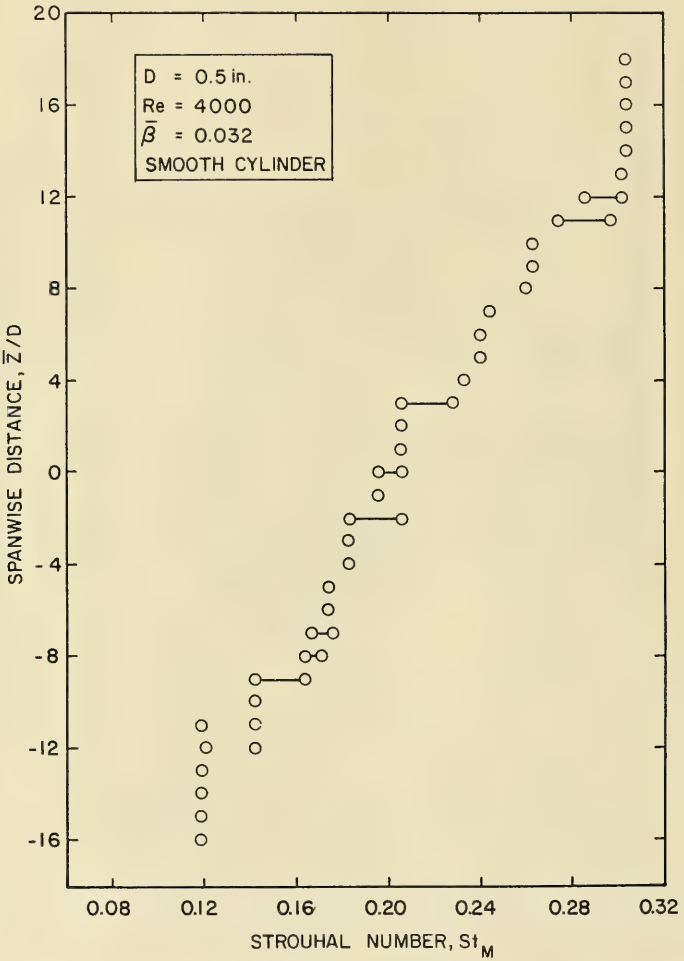

Figure 2.25 Strouhal number St_M (based upon the center line velocity V_M) plotted against the spanwise distance along a circular cylinder in a linear shear flow; from Peterka, Cermak and Woo (41). Reynolds number $Re_M = 4000$, shear flow steepness parameter $\bar{\beta} = 0.032$.

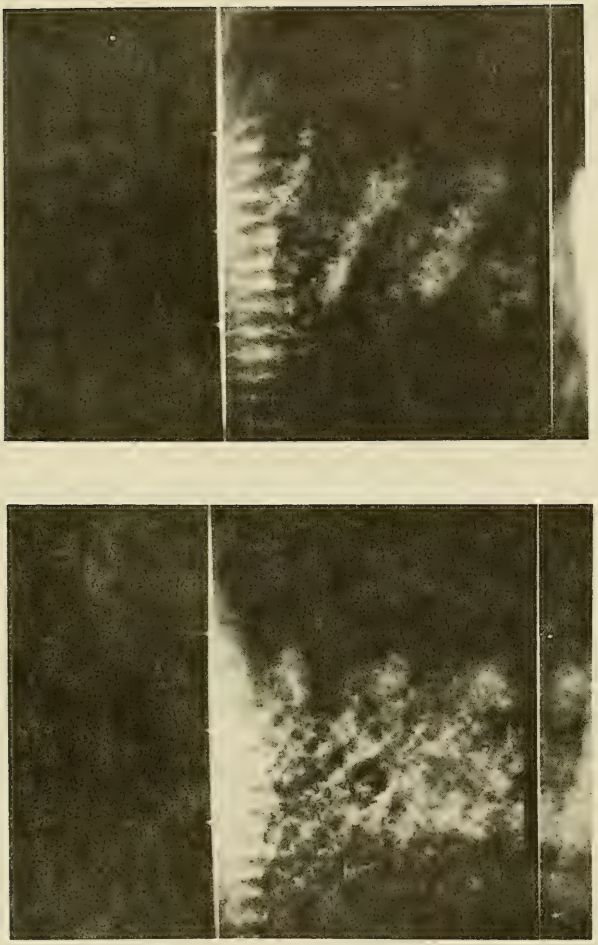

Figure 2.26 Long exposure photographs of vortex shedding from a circular cylinder in a linear shear flow; from Peterka, Cermak and Woo (41). Reynolds number $\mathrm{Re}_M = 20000$; shear flow steepness parameter $\bar{\beta} = 0.032$; cylinder aspect ratio $L/D = 20$. The photographs were provided by Dr. Jon Peterka, Colorado State University.

3. EXPERIMENTAL STRUMMING RESULTS

3.1 Behavior of Cables in Fluid Flows. The measured frequency and displacement amplitude responses for small-diameter taut cables undergoing cross flow strumming vibrations in water are plotted in Figs. 3.1 and 3.2. These results are taken from laboratory-scale experiments reported by Dale, Menzel and McCandless (45). In the first set of experiments (see Fig. 3.1) a 2.5 mm diameter cable, 0.9 m in length, was excited in three resonant strumming modes over the frequency range 14-28 Hz, and in the second set of experiments (see Fig. 3.2) a cable of the same diameter, but 1.8 m in length, was excited in six modes over the same frequency range. Predictions have been made for the response frequency and the strumming displacement for the case shown in Fig. 3.1 and they are shown there as a function of the flow speed V together with the experimental results obtained by Dale and his colleagues. The calculations of the cable response were made with the "wake-oscillator" model of Skop and Griffin that is described in Appendix D. The agreement between the prediction and the experiments is generally satisfactory for the strumming displacement and frequency, the flow speed at the maximum amplitude and the flow speeds at which the cable passes from one natural mode to the next. The reduced velocities which correspond to the peak strumming displacements are noted on the figure.

The higher modes and frequencies of the cable result in larger strumming displacements. This follows from the dependence of the cable's damping ratio ζ_s on 1/f, which results in smaller values of the reduced damping at the higher frequencies and, consequently, larger strumming amplitudes. A similar result was obtained by King (46), who found that the higher normal modes of a flexible cantilever corresponded to smaller values of ζ_s/μ or k_s, so that the higher modes experience increasing peak displacements.

The steady drag and the tension fluctuations on a strumming small-diameter cable were measured by Dale and McCandless (47). The cables employed in the experiments were between 1.45 mm (0.057 in) and 3.6 mm (0.140 in) in diameter and approximately 0.9 m (3 ft) long. A spherical mass of 0.23 kg (0.5 lb) was attached to the free end of the cables as they were towed through still water. The details of the experimental set-up are discussed by Dale and McCandless.

The drag and strumming force (fluctuating tension at the attachment) are plotted in Figs. 3.3 and 3.4. The tests were conducted with a smooth cable 2.72 mm (0.107 in) in diameter. The third ($n = 3$) and fourth ($n = 4$) mode resonances of the cable are clearly shown as the relative flow velocity (Reynolds number) is increased. A portion of the second mode ($n = 2$) is visible at the left-hand side of both figures. The drag coefficient C_D is amplified for all of the modes from the stationary cable reference value plotted in the figure. The peak value of the tension fluctuation for each cable mode corresponds to the peak strumming displacement amplitude and to the peak drag coefficient for that particular cable mode. In other experiments conducted as part of the same program, Dale and McCandless measured strumming drag coefficients as large as $C_D = 2$. This corresponds to an amplification of the steady drag by a factor of about two, and this finding is in good agreement with the results discussed in Section 2 of this report.

Some indication of the changes that occur in the flow pattern in the wake of a strumming cable can be obtained from the photographs in Fig. 3.5. The photographs were taken at NRL in a wind tunnel equipped with an aerosol flow visualization system (48). Two views of each of the cable wakes are shown with the flexible cable held stationary and with the cable vibrating with the sinusoidal displacement amplitude pattern along its length that is typical of strumming. In the photographs the maximum displacement amplitude is about 30 percent of a diameter, and the wake is highly coherent with $\rho_{AB} \approx 0.9$ (see Section 2.3) over a distance of 10 diameters along the cable's length. One photograph from the wake of the vibrating cable represents the wake of a node in the vibration pattern; in this case the wake is irregular and similar to the pattern downstream from the stationary cylinder. When the displacement amplitude is 0.3 D the wake flow is highly regular and coherent, and the vortex pattern is typical of the wake of a resonantly vibrating bluff body.

3.2 Towing and Flow Channel Experiments. A program of cable strumming experiments was carried out in the towing basin at the David W. Taylor Naval Ship R&D Center (DTNSRDC) (29,49,50). These experiments added more details concerning the behavior of flexible cables to the fundamental results that are described earlier in this report.

The following dimensionless parameters were varied during the towing experiments:

- Reynolds number, $\mathrm{Re}_n = V \sin\theta\, D/\nu$, based on the normal component of the incident flow;
- Length-to-diameter ratio, L/D;
- Angle, θ, between the cable and the incident flow;
- Tuning parameter, $2T/\rho V^2 DL$, which determines the mode of vibration, i.e. fundamental, second harmonic, etc. (T is the tension in the cable);
- Density ratio, $\rho_c/\rho = \frac{2}{\pi}\left(\frac{2m}{\rho D^2}\right)$, where ρ_c is the density of the cable material and m is the cable's mass per unit length.

In order to specify these and other parameters the following measurements were made during the experiments:

- In-line and transverse displacements along the span of the cable to characterize the various mode shapes;
- In-line (drag), transverse (lift) and tangential forces at one end of the cable;
- Static tension at the other end of the cable;
- Tow speed.

Three models (Double Armor Steel, Uniline and Small Diameter Cables) were fabricated to vary the cable density and length-to-diameter ratio; the physical characteristics of the models are listed in Table 3.1. The added mass and damping properties of these cables are discussed in Appendix C of this report. A rotatable twin strut assembly was used in which cables up to 4.4 m (14.5 ft) in length could be held at static tensions up to 2225N (500 lb) and towed at speeds up to 2.6 m/s (5 kt) at various angles to the tow direction between $\theta = 0$ and 90°. A sketch of the test rig is shown in Fig. 3.6. Two

sensors were used to measure displacements at selected points along the cable. Each sensor was comprised of two sets of electric dipoles, which were set 89 mm (3.5 in) apart; these were used to sense the position of the cable in terms of two vector signals R_1 and R_2. In later analysis of the data, the horizontal and vertical displacements were derived from R_1 and R_2. The accuracies obtained in the measurement and analysis processes were calculated and are discussed in detail together with equipment and data analysis techniques in references 49 and 50.

Table 3.1
Cable Model Physical Characteristics:
DTNSRDC Experiments

Model	Diameter	Length	Weight, N/m	
	mm	m	In Air	In Water
Double Armored Steel (DAS)	15.5	4.38	7.59	5.71
Uniline	15.2	4.35	2.77	1.01
Small Diameter	1.77	4.34	0.095	0.070

Experimental conditions were chosen for the three cables to vary the five dimensionless parameters discussed above and to bracket each resonant condition with several runs at various constant towing speeds. To select these speeds for each static tension setting, the tow carriage was slowly accelerated through a wide speed range. Strip chart recordings of the forces during a portion of a typical acceleration sweep are shown in Fig. 3.7 for the Double-Armored Steel cable oriented normal to the flow and under 1650N (370 lb) of static tension. As the carriage speed was increased from zero, a resonance appeared in the drag signal at about 0.1 m/s and then diminished at about 0.2 m/s (0.4 kt). This represents an in-line mode where the cable was oscillating in the direction of the flow. As the speed was increased from 0.4 to 0.8 m/s (0.7 to 1.5 kt) in Fig. 3.7, a fundamental-mode resonance appeared in the midspan displacements and in the forces. Within this range, higher harmonics of the motion begin to appear, especially in the flow direction. The displacement spectra for five speeds in this range, shown in Fig. 3.8, clearly illustrate the build-up of these harmonics. Over a still higher range of speeds, between 0.9 and 1.3 m/s (1.8 and 2.5 kts), a second harmonic resonance appeared in the displacements at the quarterspan and in the flow-induced forces (49,50).

The data from the DTNSRDC towing experiments are compiled in Table 3.2. In addition to the kind of results already discussed, these experiments reveal a number of interesting phenomena. Consider first the data from experiments 10, 7 and 23 in the table. These measurements were obtained on the Double Armor Steel Cable at a relatively low tension, T = 289N (65 lb); this condition corresponds to a slack cable (see Appendix B). The critical tension H below which slack cable effects become important is given by the equation

$$H_{crit} = 0.93\ (W^2EA)^{1/3}, \qquad (3.1)$$

where W is the *total* weight of the cable in water, E is Young's modulus of the cable material and A is the cable's cross-section area. These parameters are all known for the case of the Double-Armored Steel (DAS) cable. The computed and measured natural frequency-tension behavior is shown in Fig. 3.9. The critical tension H_{crit} is in the range 756 to 1112N (170 to 250 lb) based on the EA values given in the figure, so that the conditions for runs 10, 7 and 23 fall well within the slack cable regime. The natural frequency of the DAS cable in water is f_n = 4.2 Hz from Fig. 3.11, which falls within the frequency "crossover" range enclosed by the dashed lines in the figure. This modal crossover is a complex phenomenon associated with the dynamics of slack cables with small sag-to-span ratios. At the crossover *three* modes of the cable have the same natural frequency and include a symmetric in-plane mode, an anti-symmetric in-plane mode and an out-of-plane or sway mode. The symmetric modes contain an even number of nodal points along the cable while the anti-symmetric modes contain an odd number of nodes. The dynamics of slack marine cables are discussed further in Appendix B of this report.

It is sufficient to note here that although the results of runs 10, 7 and 23 fall within this complex regime, *the transverse vibration amplitudes for these runs are comparable to those measured under taut conditions.* The strumming waveform contains an appreciable in-line component at the *transverse vibration* frequency and there are large phase differences between the in-line and transverse components. Small or non-existent phase differences were exhibited during the taut cable strumming experiments.

Table 3.2
Results of The DTNSRDC Towing Tank Cable Strumming Experiments

Cable type	Experiment number	Cable tension, T (lb, N)	Vibration frequency, f (Hz)	Mode (Hz)	Natural frequency in water, f_n	Reduced velocity, $V\sin\theta/f_n D$ (deg)	Phase angle, ϕ_{xy} $2Y/D$	Double amplitude displacement $2R/D$†	
Double Armor	10 (Tow angle,	(65,290)	2.46	Fund	4.2	3.31	118.5	0.25	
steel;	7 $\theta = 90°$)		3.46	($n = 1$)	(slack cable)	5.04	121.2	0.91	
$D = 0.6$ in.	23		3.52			5.60	131.0	0.65	
15.2	36	(370,1640)	3.94	Fund	4.56	4.65			0.09
	37		4.62	($n = 1$)	(taut cable)	5.37			1.07
	30 ($\theta = 90°$)		4.77			6.17			1.28
	38		5.05			6.83			1.12
	41	(365,1620)	5.30			7.70			0.97
	42	(365,1620)	9.00	$n = 2$	9.18	7.25			0.89
	45	(375,1665)	9.28			7.58			1.08
	33 ($\theta = 90°$)	(370,1640)	9.51			8.19			1.12
	48	(375,1665)	9.83			8.33			1.05
	51		9.99			8.73			1.09
	109	(265,1180)	3.88	Fund	3.86	4.82	−1.4	0.62	0.64
	104		3.96	($n = 1$)		5.50	−1.8	1.22	1.35
	105 ($\theta = 60°$)		4.09			6.24	6.9	1.40	1.55
	108		4.43			7.06	–	0.99	1.12
	112		4.55			7.80	11.4	1.05	1.18
	115	(265,1180)	7.62	$n = 2$	7.72	7.35	−1.8	0.70	1.04
	121 ($\theta = 60°$)		1.13			7.87	−0.7	0.77	1.19
	124		8.31			8.24	−1.2	0.81	1.32
	127		8.48			8.52	−0.9	0.87	1.36
Uniline:	72	(216,960)	4.25	Fund	4.68	4.61			0.33
$D = 0.6$ in.	73		4.68	($n = 1$)		5.34			1.23
15.2 mm	59 ($\theta = 90°$)		4.75			5.70			1.09
	74		4.80			6.06			1.18
	76		5.14			6.86	−10.3		1.29
	64		11.08	$n = 2$	9.36	6.89		0.44	
	66		9.89			7.25			1.08
	68 ($\theta = 90°$)		11.66			7.58			0.41
	70		11.89			7.94			0.36
	62		12.01			8.37			0.38
Small diameter;	86	(20.89)	9.5	Fund	9.82	4.45			0.22
$D = 0.07$ in.	87		9.0	($n = 1$)		5.04			0.62
1.8 mm	88 ($\theta = 90°$)		9.9			5.93			1.07
	89		10.8			6.52			1.15
	90		11.0			7.12			0.99
	92	(20.89)	21.7	$n = 2$	19.64	6.07	−49.8	0.34	
	93						6.38	−70.4	0.43
	94 ($\theta = 90°$)		21.9			6.60	−43.8	0.48	
	95		22.3			6.82	−45.8	0.45	
	96		22.3			7.27	−44.9	0.46	

†See equation (3.4); displacement measured at the cable antinode.

The taut cable natural frequencies in Table 3.2 were calculated from the string equation

$$f_n = \frac{n}{2L}\sqrt{\frac{T}{m'}},\ n = 1,\ 2,\ 3\ \ldots \tag{3.2}$$

where n is the mode number, T is the static tension, L is the cable length (span) and m' is the cable's virtual mass. The added mass coefficients employed in computing the cable's natural frequencies were

measured for the three cables at NRL and are discussed in Appendix C. The measured displacements at the cable antinodes contain components in-line with the tow direction as well as in the transverse direction. These in-line components in all cases have a frequency *equal to* the transverse cable vibration frequency. For most of the tests conducted at the second harmonic of the fundamental frequency, however the in-line component of the displacement signal at the cable antinode *is equal to or greater than the transverse component.*

If the two components of the cable motion at the frequency $\omega = 2\pi f$ are

$$x = \bar{X} \sin(\omega t) \quad in-line \tag{3.3a}$$

$$y = \bar{Y} \sin(\omega t + \phi_{xy}) \quad transverse, \tag{3.3b}$$

then the results show that $\phi_{xy} = 0$ for most of the Double-Armored Steel and Uniline cable experiments. This suggests that the cable strumming waveform at the antinode takes the form

$$r = \sqrt{\bar{X}^2 + \bar{Y}^2} \sin(\omega t) = \bar{R} \sin(\omega t) \tag{3.4}$$

where $\bar{R} = \sqrt{\bar{X}^2 + \bar{Y}^2}$ is the resultant displacement. When the phase angle ϕ_{xy} is non-zero as in a number of cases, i.e., the slack cable conditions, a complex strumming waveform shape with time-varying displacement is obtained.

The displacements for several runs are plotted in Fig. 3.10 as a function of the reduced velocity $V_r = V \sin\theta / f_n D$, where the normal velocity component incident to the cable is given by $V \sin\theta$. (The legend on the figure lists the tension, inclination angle, structural log decrement, and the reduced damping k_s for the three cables.) Each run corresponds to a resonant, vortex-excited response over the lock-on regime between the vortex shedding and cable vibration frequencies. In the first mode ($n = 1$) results shown in Fig. 3.10, all three cables exhibit nearly the same maximum strumming displacement at $V_r \approx 6$, which is typical of vortex-excited oscillations of cables and bluff structures as shown by the results in Fig. 2.1 and Table 2. The peak displacement amplitude for the yawed DAS cable is higher by about 20% from the unyawed cable even though the yawed cable damping is apparently higher. The structural damping of the cable was dependent upon the orientation of the mounting struts (see Appendix C) as they were rotated to align with the tow direction. Thus there is some variation in the

measured structural damping due to changes in the strut stiffness with yaw angle, which may account for the response changes. The reduced damping k_s of the cables is very low, and the peak displacement changes only slightly with k_s except for the anomaly just mentioned. The peak displacements are slightly lower than one might expect from the limiting values at low damping in Fig. 2.2, but the measured strumming frequencies in Fig. 3.10 clearly show the constant frequency vs. flow velocity resonance (lock-on) that characterizes vortex-excited oscillations.

The second mode ($n = 2$) results for the three slack cables exhibited many of the strumming characteristics that are evident from the fundamental mode results shown in Fig. 3.10. The peak displacements and their corresponding reduced velocities are listed in Table 3.2. The resultant strumming amplitudes of the DAS and Uniline cables are nearly the same as in the fundamental mode, but the second-mode displacement for the small diameter cable is about half the fundamental mode response. This anomalous behavior (compared to taut cables) is very likely due to the complex strumming waveform in the $n = 2$ mode that is characterized by large values of the phase angle ϕ_{xy} (see Table 3.2) and the relatively large in-line components of the vibration at the strumming frequency. Based upon the results from the preceding section, one would expect the cable strumming in the second mode to exhibit slightly larger displacements than in the fundamental mode. The cable vibration frequencies in the second mode again are typical of the frequency vs. velocity dependence that characterizes the lock-on phenomenon as discussed in Sections 2 and 3.1 of this report.

As part of the overall CEL/NCBC cable dynamics research program MAR Incorporated conducted a program of experiments to investigate the effects of sensor housings (attached discrete masses) on the overall cable response. A first report on the results obtained has been given recently by Kline, Fitzgerald, Tyler and Brzoska (51). Some of these results are summarized briefly here and compared with the previous findings from the cable dynamics program shown in Fig. 3.10. The tests were conducted on the same "strumming rig" at the DTNSRDC that was employed in previous CEL-sponsored strumming experiments. The recent MAR Incorporated experiments and the experimental layout are described in detail in references (49) and (51).

Some of the results obtained in these experiments are plotted in Fig. 3.11. The attached masses in all cases were one or two aluminum sensor housings attached at various locations along the 4.57 mm (0.18 in.) diameter steel cable span of 4.42 m (14.5 ft). It can be seen from the results in the figure that the cable was tested at various conditions in the resonant, cross flow strumming regime during the experiments. It should be noted that *the attached masses did not deter or diminish the strumming,* but instead the system consisting of a bare cable plus attached masses reached higher cross flow displacement amplitudes than the bare cable alone. It should be noted that the conditions of MAR's bare cable reference experiment were at the onset of the resonant strumming regime while the attached mass experiments reached well into the resonant region as shown in Fig. 3.11. All of the tests were conducted in the range of cable and attached mass properties where hydrodynamic effects dominate (the left-hand portion of Fig. 2.2), and even the addition of concentrated masses does little to deter large-displacement cross flow strumming effects. All of the frequency spectra plotted in reference 51 give clear evidence of cross flow strumming at a single resonant frequency. Many of the dynamic properties of marine cables with attached masses can be calculated from the results of a study by Chung (52). Further studies of the behavior of cables with attached masses are continuing as part of the NAVFAC/CEL cable dynamics program.

3.3 Small-Scale Field Experiments. Field studies of the strumming behavior of marine cables were conducted over several summers at Castine Bay, Maine by staff members of the Ocean Engineering Department at MIT. The field test layout is shown in Fig. 3.12. Sections of faired and unfaired cables, nominally 23 m (76 ft) in length, were positioned normal to a spatially uniform tidal current which ranged in magnitude from 0 to 0.7 m/sec (0 to 1.36 kt). The earlier experiments have been reported in detail (53). The most recent experiments, performed during 1976, were concerned with detailed measurements of the strumming response of both unfaired and faired marine cables in an ocean environment (54). As with the DTNSRDC cables, measurements of the natural frequencies (in-air and in-water), the added mass, and the fluid dynamic damping of the cables were made at NRL and are discussed in Appendix C.

The strumming behavior of the cables tested during these experiments has been classified into three general categories: resonant lock-on, non-resonant lock-on and non-lock-on. The first of these categories, resonant lock-on, is characterized by very stable motion of the cable in one of its natural modes where the displacement is sinusoidal and the displacement amplitude is essentially constant. Non-resonant lock-on is characterized by small modulations in the cable vibration displacement and frequency. These two lock-on regimes are shown in Fig. 3.13 where two data records from the Castine Bay experiments are plotted. Non-lock-on occurs when the natural vortex shedding frequency is just outside of the synchronization range. The results obtained in this latter regime are discussed in a recent paper by Kennedy and Vandiver (55).

The results from the Castine Bay experiments that pertain to the case of resonant lock-on are now discussed. The actual vibration frequencies measured at currents between 0.2 and 0.6 m/sec (0.4 and 1.2 kt) with an unfaired polyester (Uniline) cable and an unfaired Kevlar cable positioned in the tidal flow are plotted in Figs. 3.14 and 3.15. The tension changed slightly (less than 5 percent) during the run time, so that the measured frequencies are scaled here by $[\text{Tension}]^{1/2}$ in order to account for the slight variations in the natural frequencies of the cable. When this adjustment is made, the natural modes of the Uniline cable are clearly highlighted as shown in Fig. 3.14. Five natural modes of the cable (n = 2, 4-7) appear over the range of tidal currents shown and all are characterized by resonant lock-on. In the case of the Kevlar cable, five natural modes (n = 3-7) also are shown in Fig. 3.15. The mode numbers were estimated from the taut cable equation

$$n \approx 2Lf_n\sqrt{\frac{m'}{T}} \tag{3.2a}$$

after taking into account the added mass of the cable. The frequency response of these relatively long cables (23 m or 76 ft) is similar to the strumming response of a meter-long cable employed by Dale, Menzel and McCandless (45) in their small scale experiments discussed in Section 3.1. The strumming response of the short sample of cable is shown in Fig. 3.1; the similarities between the field and the laboratory are evident.

Some indication of the reproducability in the field tests is given by Fig. 3.16 which shows the (scaled) frequencies measured at two different positions along the Kevlar cable during two different runs. The agreement between the two test runs is excellent. The resonant strumming displacements for two runs with the Kevlar cable ($n = 2$) and one run with the Uniline cable ($n = 5$) are plotted as a function of the reduced velocity V_r in Fig. 3.17. The measured displacements are shown on a relative scale. The data for the individual runs are divided by the maximum measured displacement for that run. The strumming results in Figs. 3.16 and 3.17 again clearly show the frequency and displacement amplitude resonances that are characteristic of the vortex-excited oscillations. As in the laboratory experiments discussed in Sections 2 and 3.1 and the towing tank results plotted in Fig. 3.10, the resonant cross flow displacements for the field tests occur at reduced velocities in the range $V_r = 5$ to 8, with maximum strumming displacements in the range $V_r = 6$ to 7.

3.4 Large Scale Field Experiments. FISHBITE is the name of a marine cable experiment conducted by Softley, Dilley and Rogers in 1976 (56). A wire rope 12 mm (0.47 in.) in diameter and 500 m (1640 ft) long was hung from a ship anchored in 1960 m (6430 ft) of water at the Tongue of the Ocean, located at 77° 52′ W and 25° 10′ N. The tidal flow varied both temporally and spatially from 0.1 to 0.4 m/s (0.2 to 0.8 knots). A current meter was attached at the halfway point, but no other lumped masses were attached to the cable. The cable response was measured at the top end only and the cable parameters resulted in a modal spacing of 0.025 Hz.

The response typically included more than one hundred modes between 8 and 12 Hz, with a center frequency of 10 Hz. An rms acceleration spectrum from the report of Softley et al. is given in Fig. 3.18. From a study of these data Kennedy and Vandiver (55) have noted that the rms response at the measurement point on the upper end of the cable was limited to less than one cable diameter. They attribute the bandwidth of the cable response to spatial and temporal variations of the current at the test site. No lock-on was observed during any of the FISHBITE experiments.

SEACON II was a major undersea construction experiment the chief goal of which was the measurement of the steady-state response of a complex three-dimensional cable structure to ocean currents.

The measured array responses were to be employed in a validation of analytical cable design models and computer codes (57). A second goal of the SEACON II experiment was to demonstrate and evaluate new developments in ocean engineering which were required to design, implant, operate, and recover fixed undersea cable structures.

The SEACON II structure consisted of a delta-shaped module with three mooring legs. It was implanted in 885 m (2900 ft) of water in the Santa Monica Basin by the Civil Engineering Laboratory during 1974 and was retrieved during 1976. The top of the cable structure was positioned 137 m (450 ft) below the water surface. The mooring legs were 1244 m (4080 ft) long and each arm of the delta was 305 m (1000 ft) long. An artist's view of the completed structure is shown in Fig. 3.19. Two mooring legs were attached to explosive anchors embedded in the sea floor and the third leg was attached to a 5680 kg (12500 lb) clump anchor. The entire cable structure was instrumented in order to collect water current and array position data.

The data were used to validate the computer code DECEL1 (previously called DESADE). This code was developed at NRL (58) and is discussed elsewhere in this report. The delta cables experienced uniform currents over their respective lengths and often were subject to cable strumming. These strumming oscillations led to increased steady drag coefficients and static deflections as discussed further in Section 4 of this report and by Skop, Griffin and Ramberg (59). Details of the SEACON II implantation, design and recovery are given by Kretschmer, Edgerton and Albertsen (57).

The drag coefficient C_D of the SEACON II cable was measured in two series of tests conducted for CEL. These measurements are plotted in Fig. 3.20. The tests conducted at the Naval Postgraduate School utitized a short segment of the cable that was restrained from oscillating. An average value of $C_D = 1.55$ was obtained. The DTNSRDC tests were conducted with a 4.6 m (15 ft) long cable segment. The resonance in the drag versus Reynolds number data in Fig. 3.20 was caused by cable strumming. The drag resonance is similar to that measured by Dale and McCandless (47) and plotted in Fig. 3.3.

A cable strumming experiment (the Bermuda Testspan) was conducted by the U.S. Navy from December 1973 to February 1974. The site of the experiment was near Argus Island, Bermuda. A 256 m (840 ft) long, 16 mm (0.63 in.) diameter electromechanical cable was suspended horizontally in the water at a depth of 28 m (92 ft). The cable had no strumming suppression devices attached, but it had numerous weights, instrumentation devices, and floats distributed over its length. The experimental arrangement is shown in Fig. 3.21. The unfaired cable and instrumentation were similar to the cables which made up the horizontal delta module of the SEACON II array. Two current meters were suspended near the mid-span point of the cable.

Kennedy and Vandiver (55) have analyzed the results of this experiment and have reached several conclusions. They found that the strumming response of the cable was typical of a broadband random process and that resonant and nonresonant lock-on were rare. The high modal density, which ranged from the 10th to the 150th mode, and extreme variations in current speed and direction were chiefly responsible for the broadband response of the test span. The peak rms cross flow displacement amplitude experienced by the Bermuda Testspan was estimated by Kennedy and Vandiver to be $\overline{Y} = \pm$ 0.5 D. A more thorough discussion of this large scale field experiment is given by Kennedy (60).

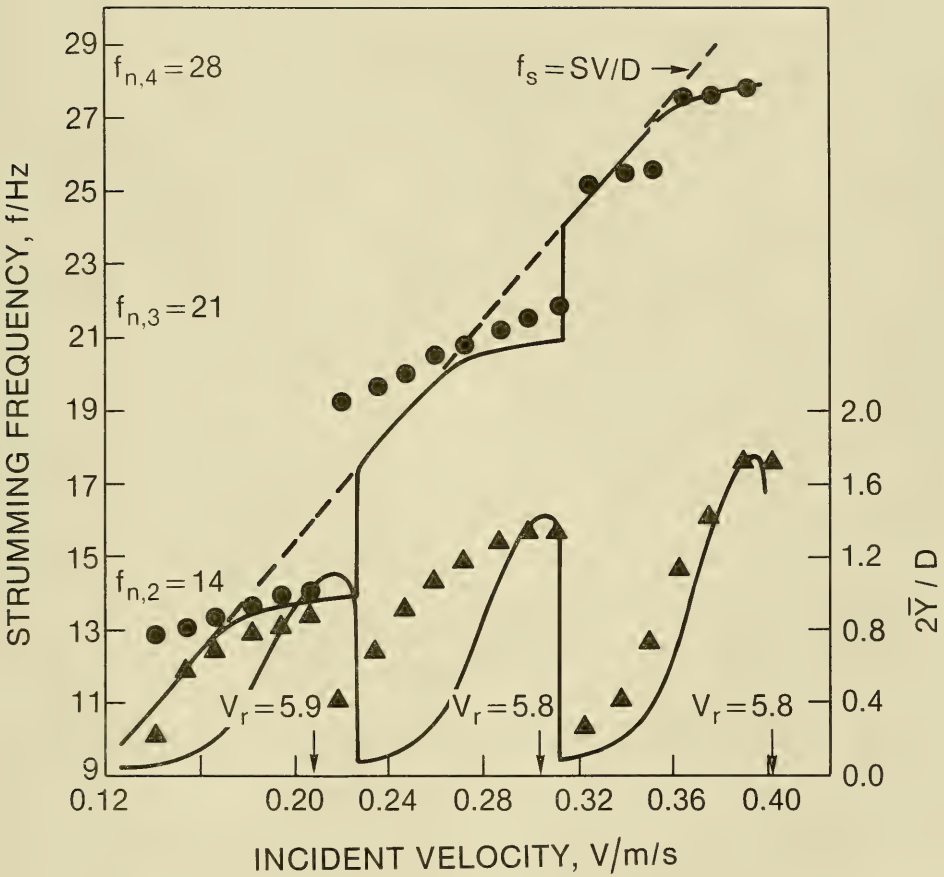

Figure 3.1 Vortex-excited strumming vibrations of a taut marine cable. The solid lines denote the predicted strumming response and the individual points denote the displacements (▲) and frequencies (●) measured by Dale, Menzel and McCandless (45). Cable length, L = 0.9 m; cable diameter, D = 2.5 mm. The frequencies of the three natural cable modes are noted on the left-hand vertical axis.

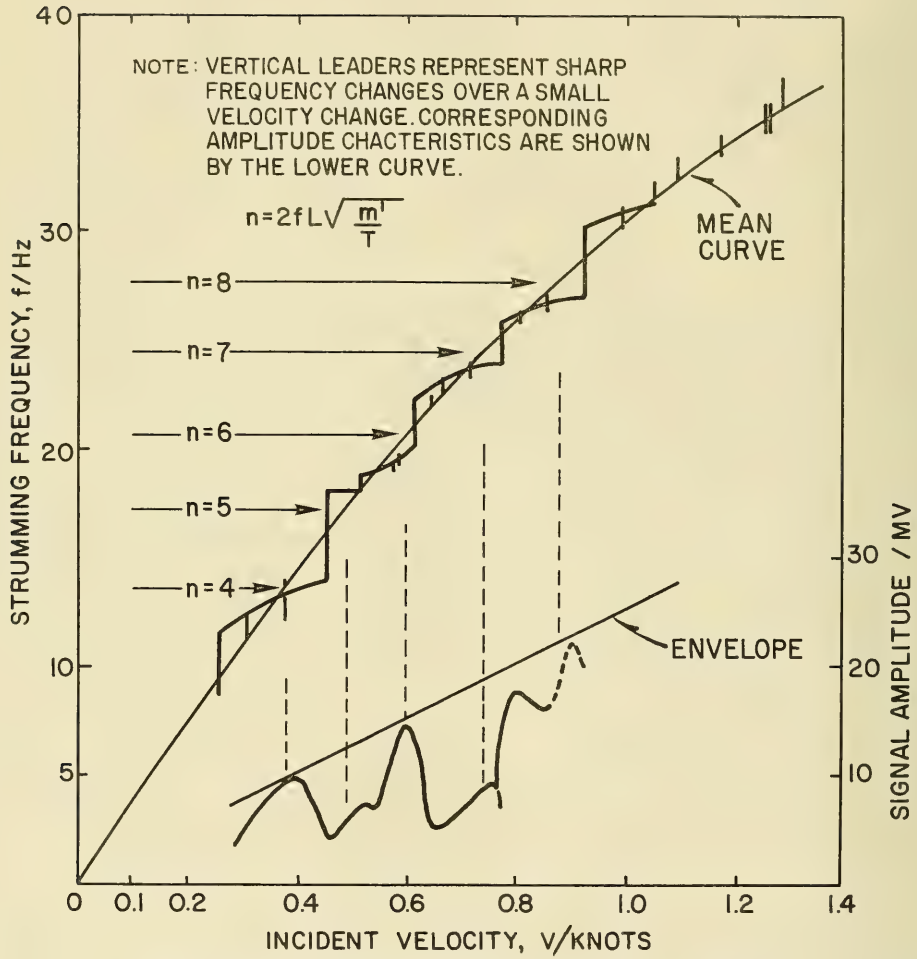

Figure 3.2 Vortex-excited strumming vibrations of a taut marine cable. Conditions as in Fig. 3.1 except $L = 1.8$ m.

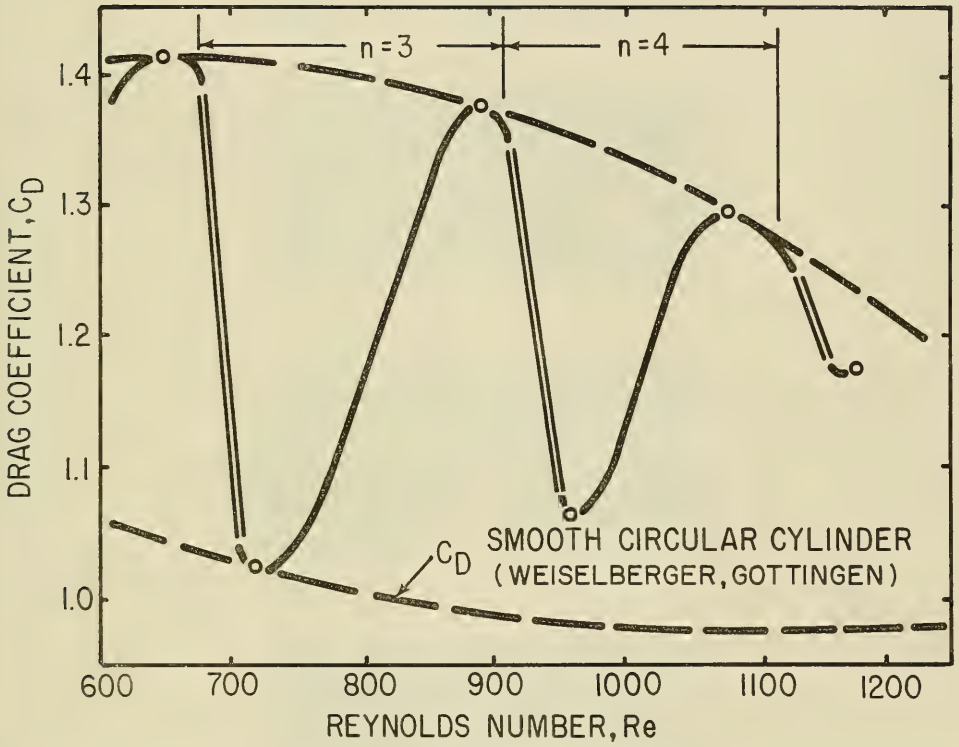

Figure 3.3 Strumming drag coefficient C_D for a smooth cable plotted against Reynolds number Re (incident relative flow speed); from Dale and McCandless (47). Cable length L = 0.9 m (3 ft), cable diameter D = mm (0.107 in.).

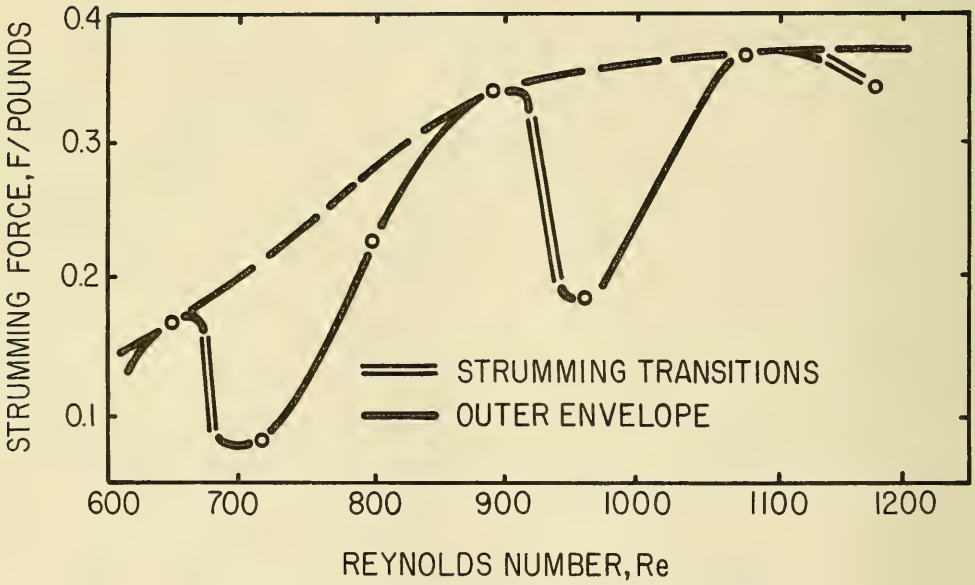

Figure 3.4 Strumming force (tension fluctuation)^2 for a smooth cable, from Dale and McCandless (47). Cable data as in Fig. 3.3.

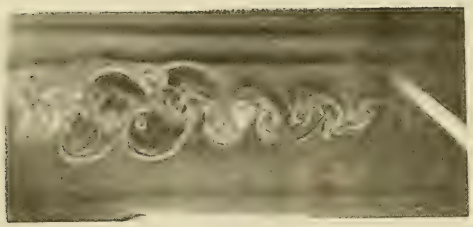

(a)

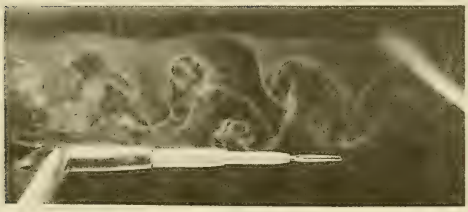

(b)

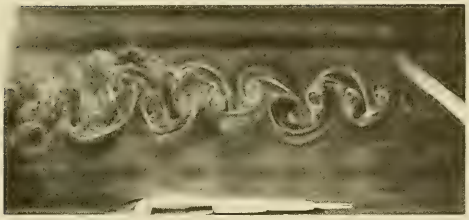

(c)

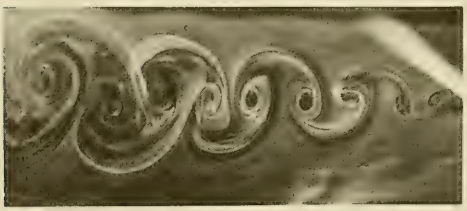

(d)

Figure 3.5 Flow visualization of vortex shedding at several spanwise ($\overline{z}$) locations along a stationary and vibrating flexible cable, at a Reynolds number of Re = 570, from Ramberg and Griffin (). (a) Stationary, $\overline{z} = 0.25\ L$. (b) Stationary, $\overline{z} = 0$. (c) Vibrating (node of the vibration pattern), $\overline{z} = 0.25\ L$ and $V_r = 5.2$. (d) Vibrating (antinode), $\overline{z} = 0$, $V_r = 5.2$ and $2\overline{Y}/D = 0.3$. The wavelength of the vibration pattern is denoted by L.

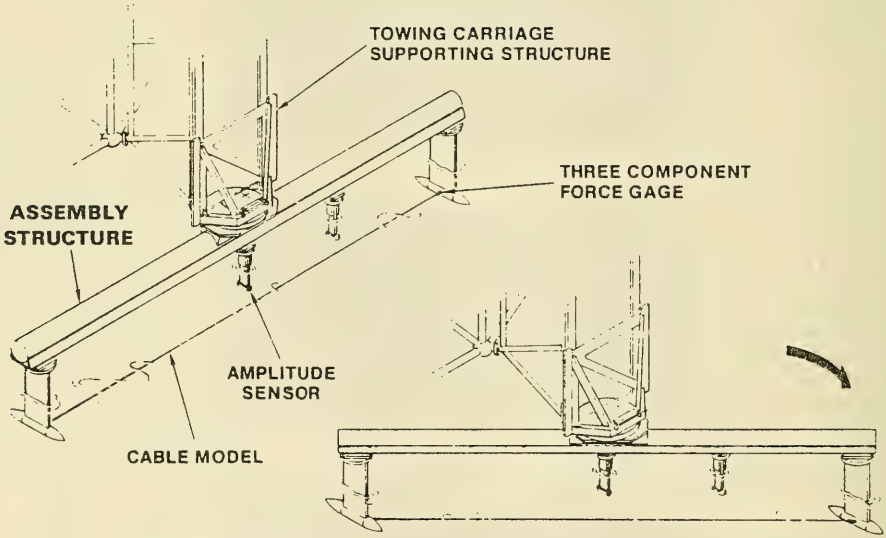

Figure 3.6 A drawing of the DTNSRDC experimental strumming test rig.

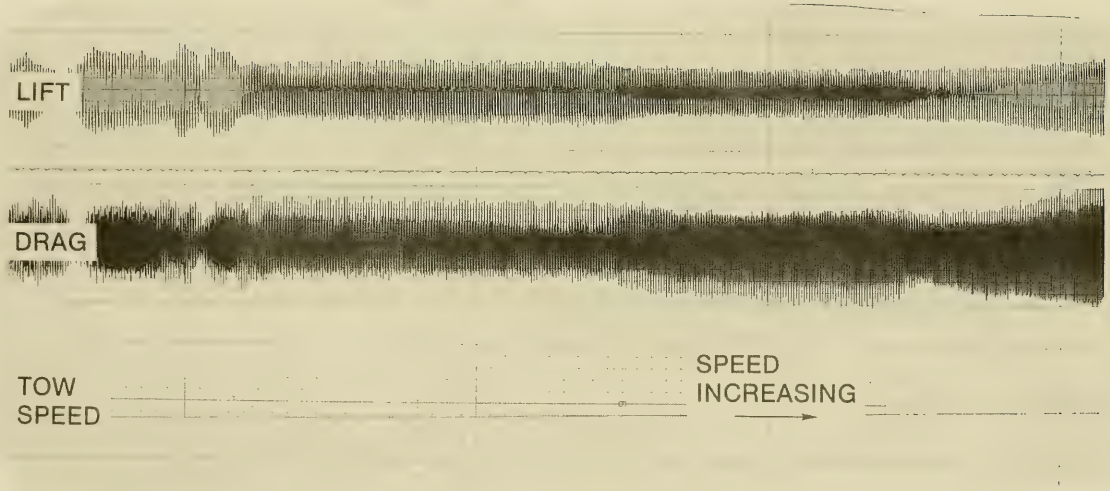

Figure 3.7 Typical force traces over a resonant portion of a cable towing acceleration sweep, from the DTNSRDC experiments. Double Armored Steel (DAS) cable, $T = 1650$ N (370 lb), $\Theta = 90°$.

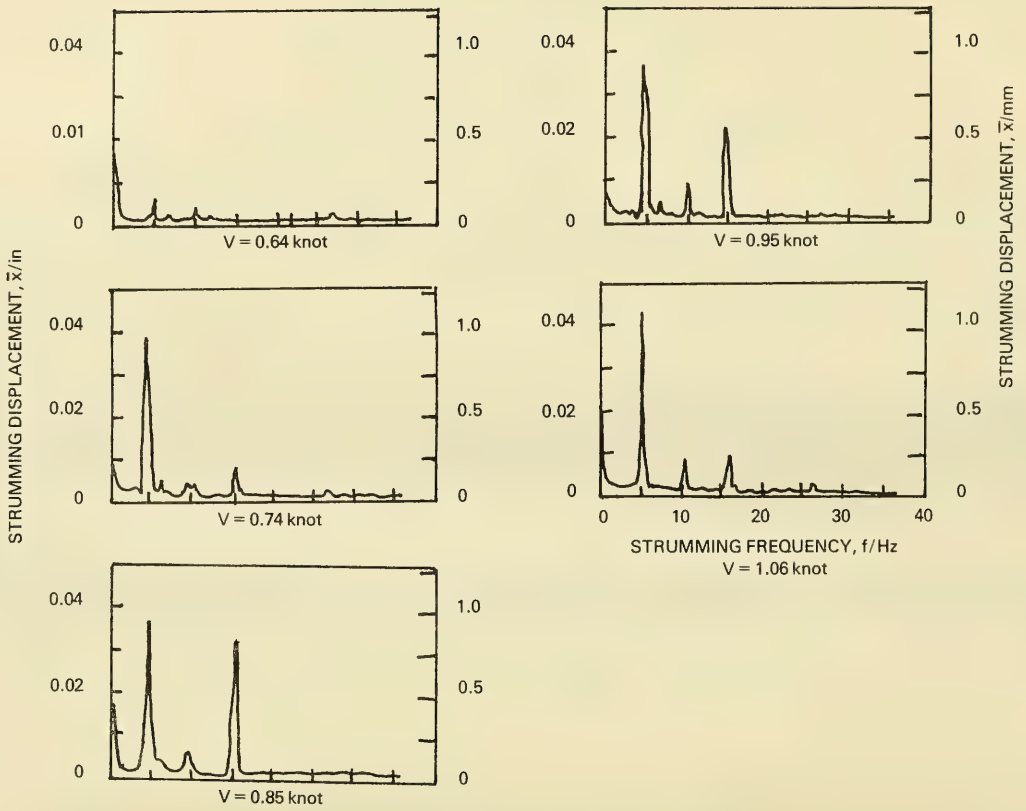

Figure 3.8a Horizontal displacement at midspan (1 kt = 0.51 m/s)

Figure 3.8 Strumming displacement spectra for a fundamental cable mode, from the DTNSRDC experiments. DAS cable, T = 1650 N (370 lbs), Θ = 90°.

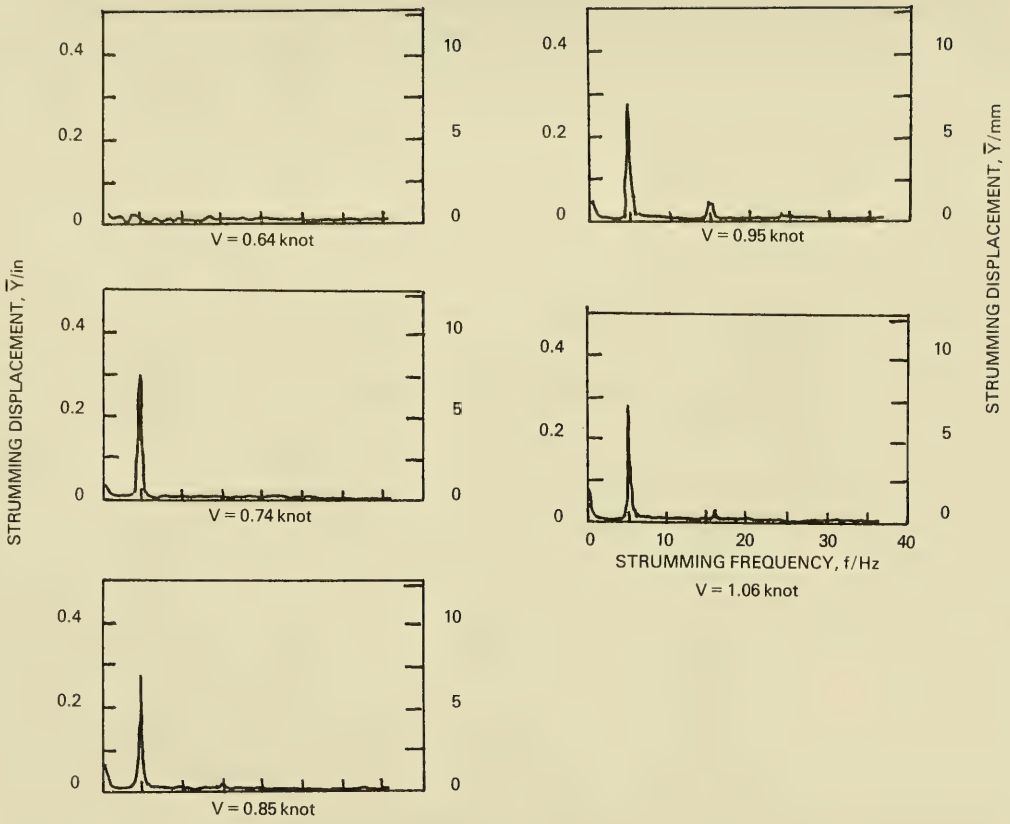

Figure 3.8b Vertical displacement at midspan (1 kt = 0.51 m/s)

Figure 3.8 (Continued) Strumming displacement spectra for a fundamental cable mode, from the DTNSRDC experiments. DAS cable, T = 1650 N (370 lbs), Θ = 90°.

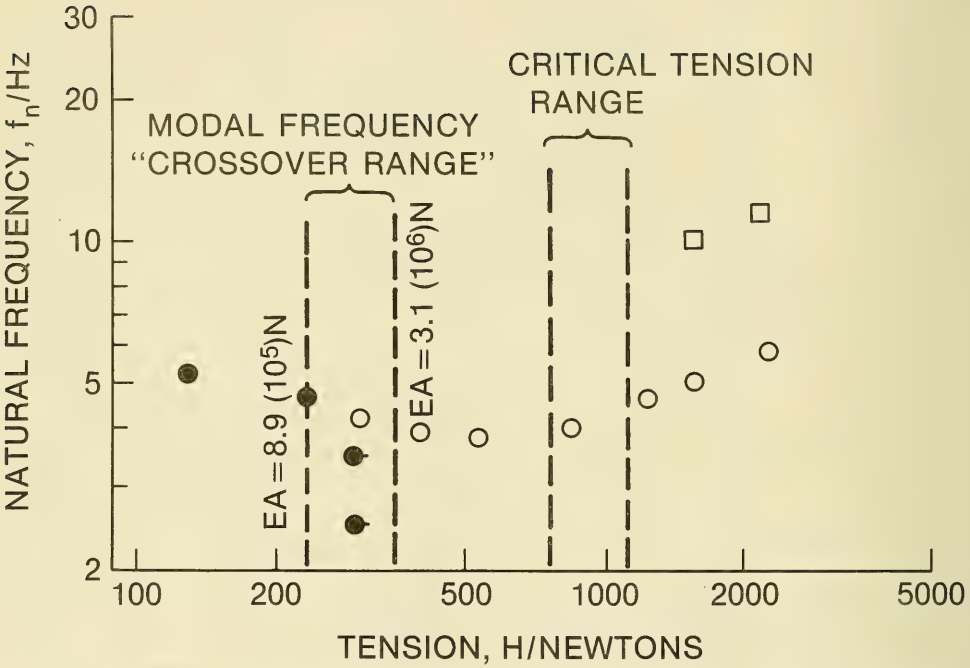

Figure 3.9 The measured vibration frequencies of a Double-Armored Steel cable in water as a function of the tension. The natural frequency "crossover" range for slack cables with small sag is predicted by the dashed lines for two values of the measured cable elastic modulus, EA. Legend for data points: ●, ○, Lowest symmetric mode of the slack DAS cable; □, Taut cable natural frequency in the second ($n = 2$) mode; ● —, experimental runs 10, 7, 23 from Table 3.2.

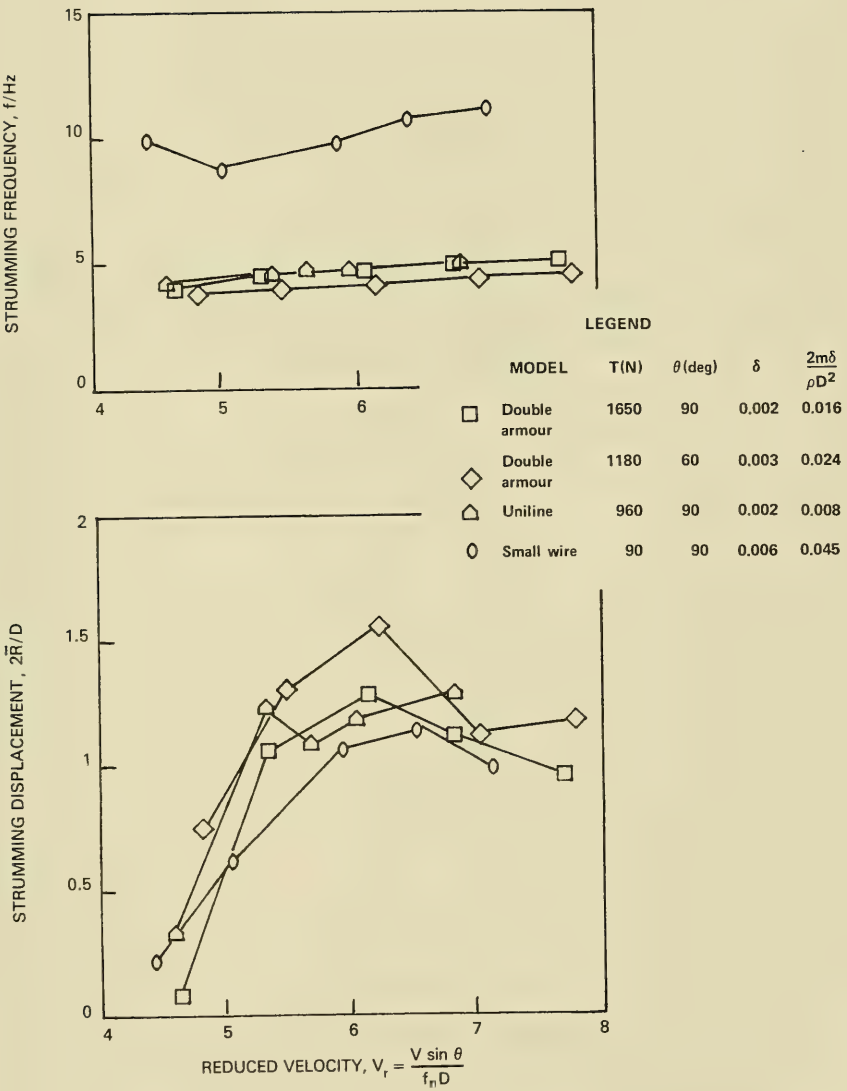

Figure 3.10 Strumming displacements and frequencies of marine cables in the fundamental mode as functions of the reduced normal velocity $V_r = V \sin\theta / f_n D$.

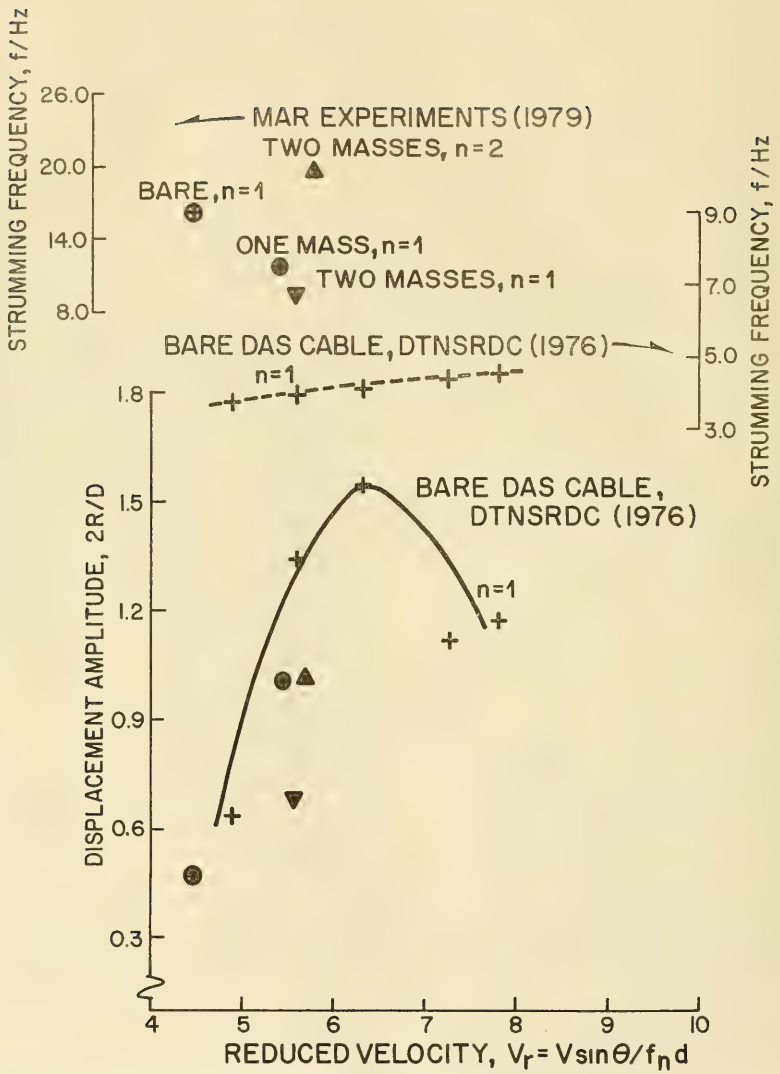

Figure 3.11 Strumming displacement amplitudes for cables with attached sensor housings. The data are plotted against a background of the bare cable data shown in Fig. 3.10.

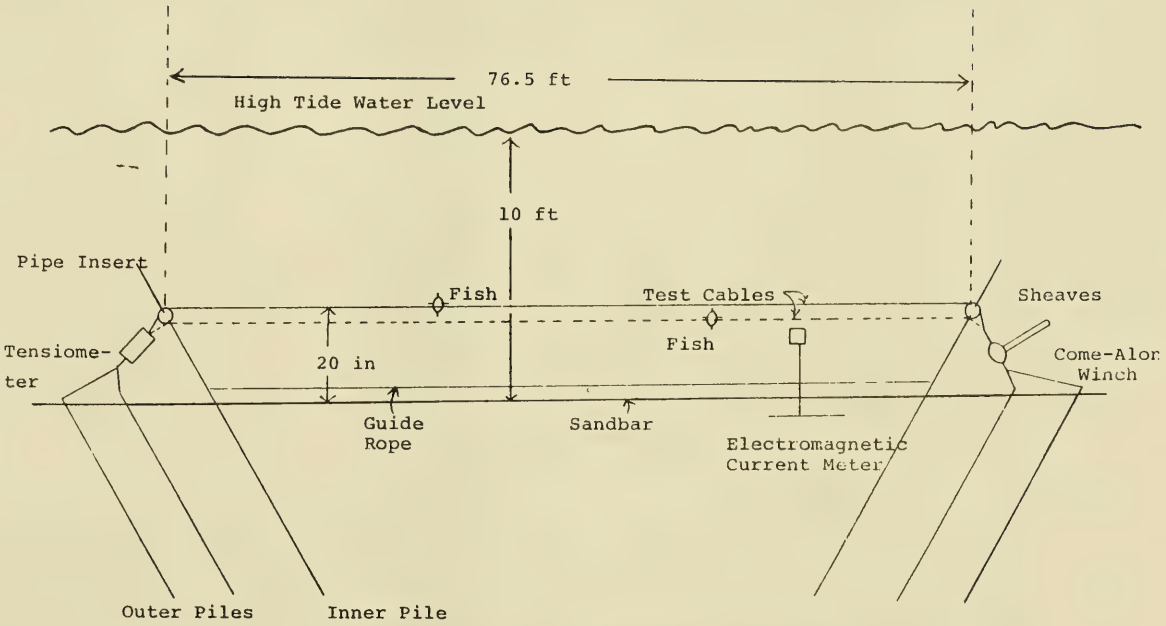

Figure 3.12 Layout of the Castine Bay cable strumming test set-up (54).

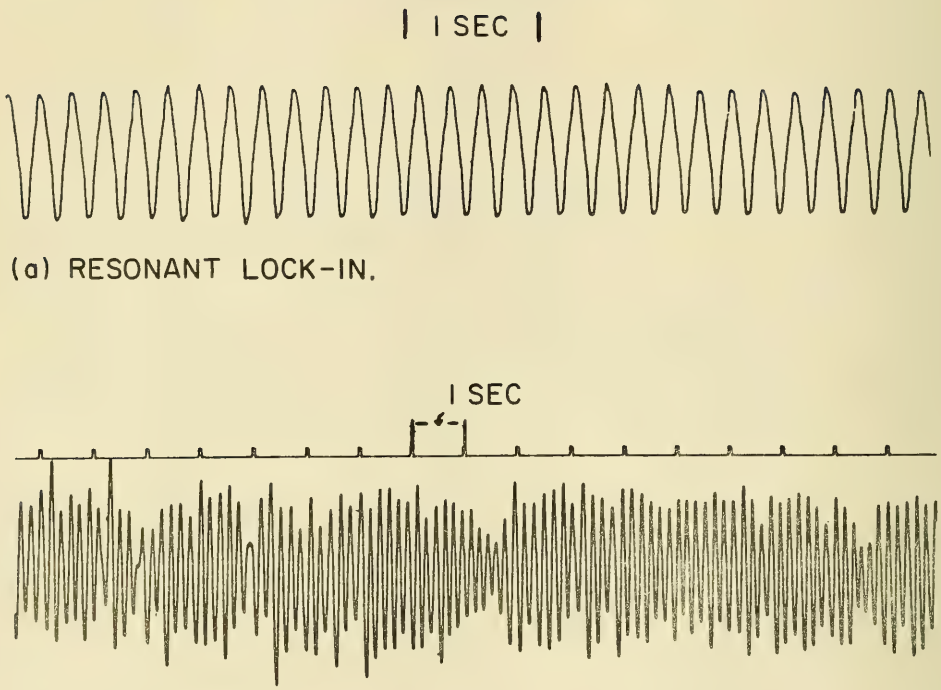

Figure 3.13 Sample displacement amplitude signal traces in the resonant and non-resonantt lock-on regimes, from the Castine Bay experiments (54).

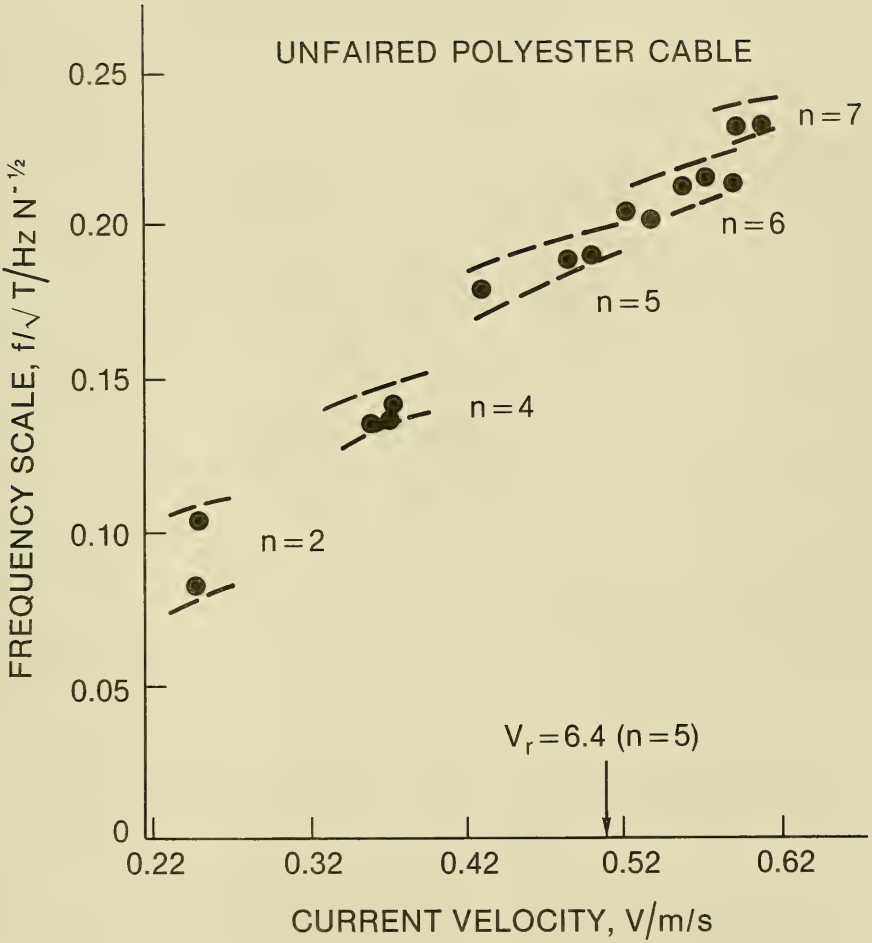

Figure 3.14 Measured resonant frequencies of cable strumming in the the ocean (54), normalized by the factor [Tension]$^{1/2}$, plotted against the tidal current speed V. Cable fundamental frequency, f_{no} = 1.2 Hz; Diameter, D = 13 mm; Specific gravity = 1.13 (Uniline polyester cable).

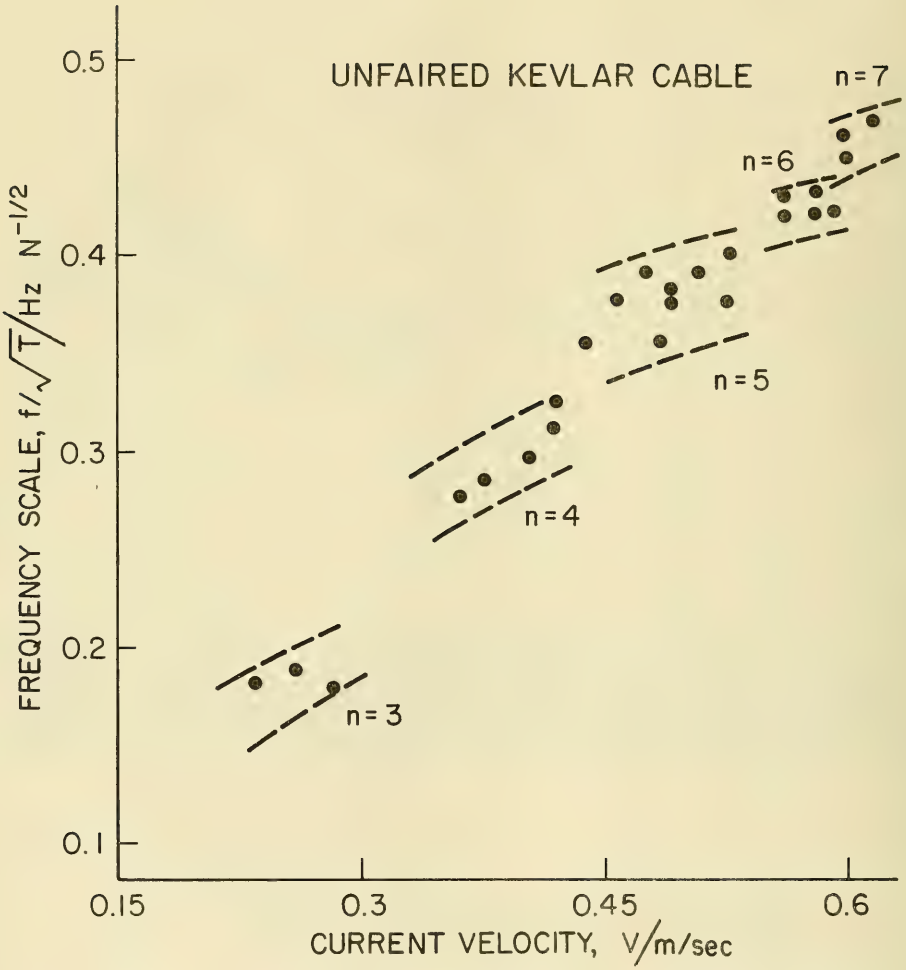

Figure 3.15 Measured resonant frequencies of cable strumming in the ocean (54), normalized by the fact [Tension]$^{1/2}$, plotted against the tidal current speed V. Cable fundamental frequency = f_{no} = 3 Hz; diameter D = 6.1 mm; specific gravity = 1.74 (Kevlar cable).

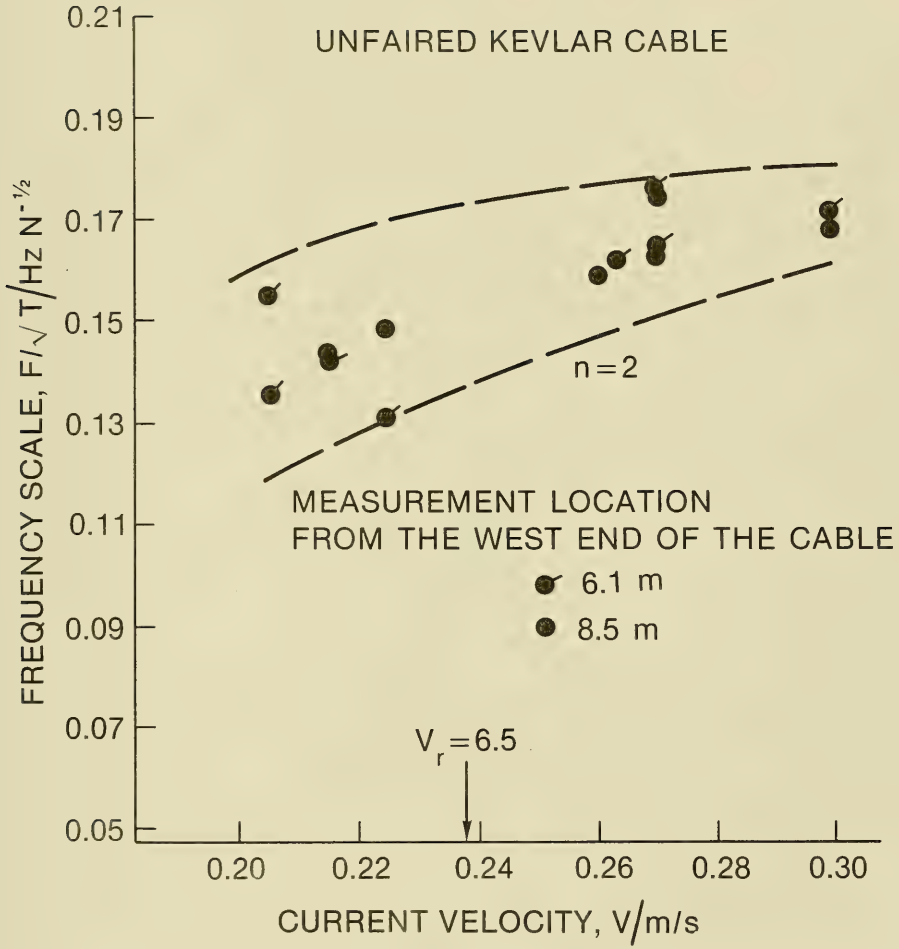

Figure 3.16 Measured resonant frequencies of cable strumming in the ocean (54) normalized by the factor [Tension]$^{1/2}$, plotted against the tidal current speed V. Case one, •: Cable fundamental frequency, f_n = 2.7 Hz. Case two, •—: Cable fundamental frequency, f_{no} = 30 Hz. Cable properties same as Fig. 3.15.

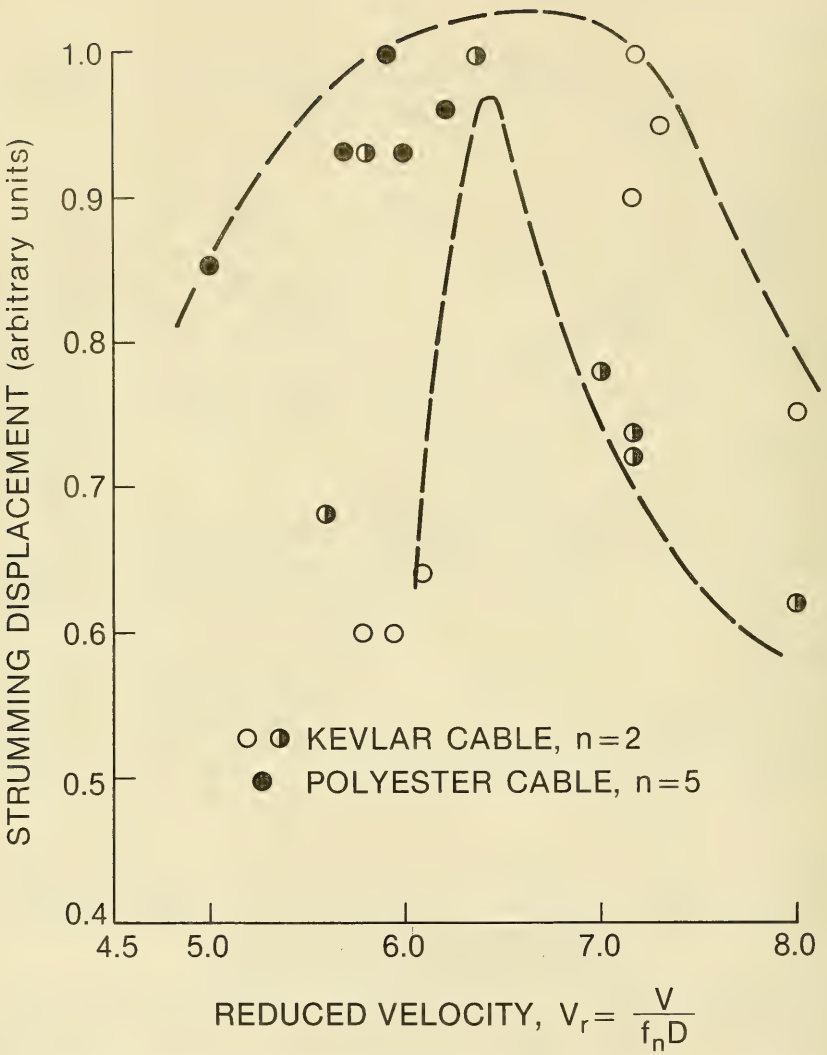

Figure 3.17 Measured resonant cable strumming displacements (54), normalized by the maximum value for each run, as a function of the reduced velocity V_r. For the Kevlar and polyester cable characteristics see Figs. 3.14 and 3.15.

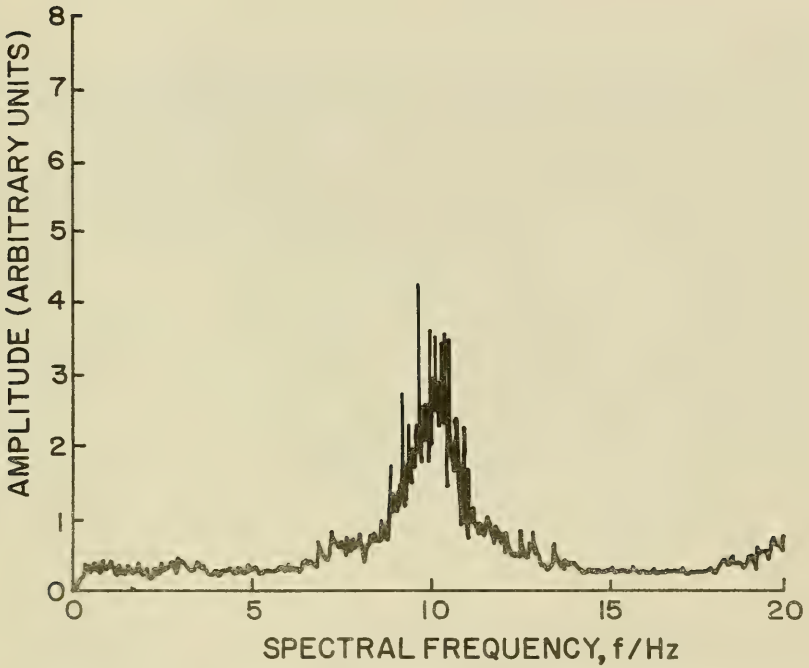

Figure 3.18 A root-mean-square acceleration spectrum of the cable strumming response measured during the FISHBITE experiments by Softley, Dilly and Rodgers (56); the figure is from reference 60.

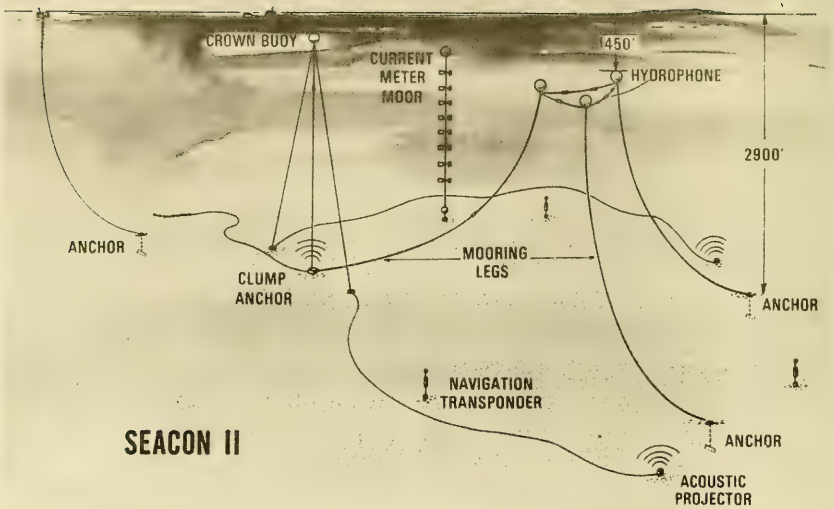

Figure 3.19 A schematic drawing of the SEACON II experimental mooring that was implanted and retrieved by the Civil Engineering Laboratory (57). The array was implanted in 885 m (2900 ft) of water in the Santa Monica Basin during 1974. The horizontal delta module of the array was approximately 137 m (450 ft) below the surface.

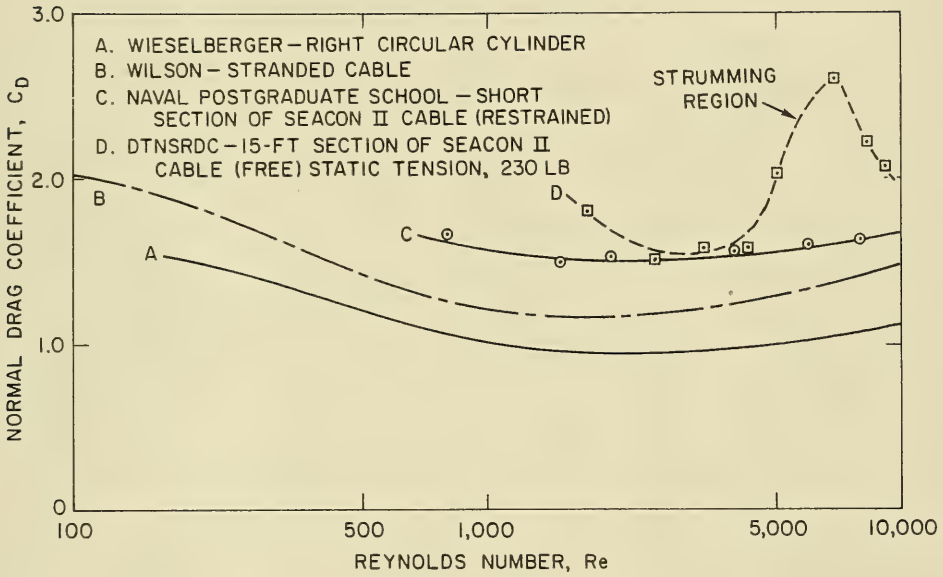

Figure 3.20 The measured normal drag coefficient C_D for the SEACON II cable plotted against the Reynolds number Re; from reference 57. Curves A and B are provided for reference purposes only.

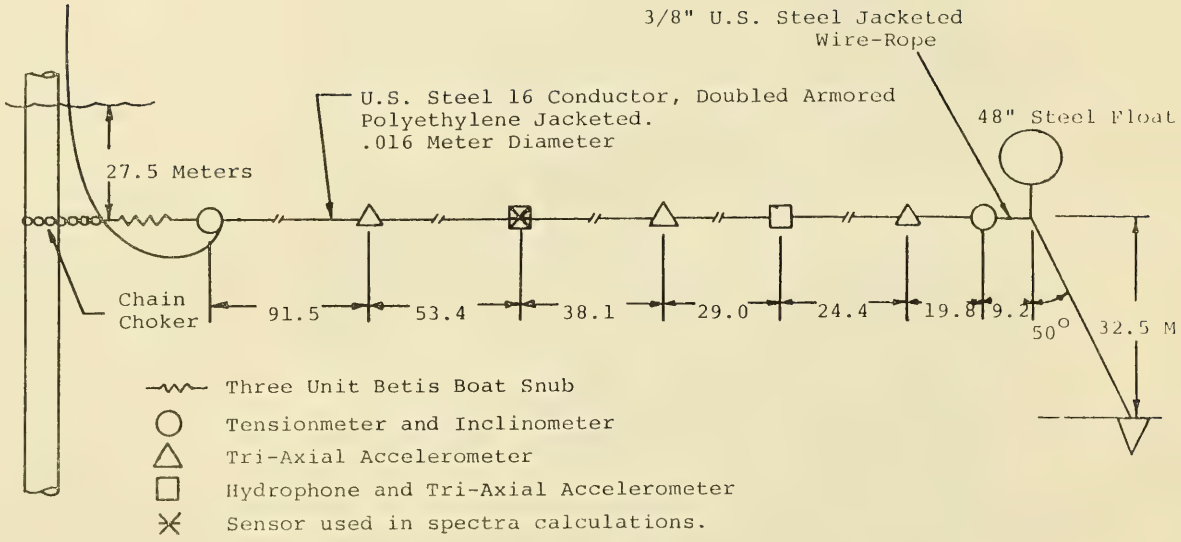

Figure 3.21 A sketch of the Bermuda Test span experimental arrangement; the figure is from reference 60. All dimensions are in meters unless noted otherwise.

4. STRUMMING CALCULATION METHODS

4.1 Analytical Models. A number of analytical models have been developed to predict the vortex-excited oscillations of general bluff, cylindrical structures. Application to cable strumming problems is but one specific example of the utility of the various methods. In general the models that have been developed fall into these categories:

- Nonlinear, or wake, oscillator models.
- Empirical models, which are based upon measured fluid dynamic force coefficients.
- Random vibration models.
- Discrete vortex models, which are based upon the insertion of arrays of small vortices to represent the overall features of the vortex shedding.
- Numerical models, which are based upon numerical integration of the governing equations of fluid motion.

The wake oscillator models have been developed because many features of the resonant interaction between the vibrations and the vortex shedding exhibit the characteristics of a nonlinear oscillation. This observation was first made by Bishop and Hassan (61) and the idea since has been developed by Skop and Griffin (9,62), Iwan and Blevins (8,63) and Hartlen and Currie (64), among others. The wake oscillator model most recently has been applied to marine riser vibration problems. Some limited success has been achieved as discussed by Fischer, Jones and King (40). The wake oscillator concept is discussed in further detail in Appendix D.

Random vibration models to predict vortex excited oscillations in general and cable strumming in particular have been developed by Blevins and Burton (21) and Kennedy and Vandiver (55), respectively. Some limited success has been achieved. A general model for employing measured force coefficients in an empirical formulation has been developed by Griffin (3,6) and Chen (65). Measured

force coefficients such as those reported by Sarpkaya (12) and Griffin and Koopmann (4) are used to predict the resonant crossflow oscillations. A discrete vortex model for predicting the vortex-excited oscillations of a flexibly-mounted rigid cylinder has been developed by Sarpkaya and Shoaff (66). A numerical integration of the time-dependent Navier-Stokes equations in the presence of an oscillating cylinder has been reported by Hurlbut, Spaulding and White (67). However this numerical scheme is limited to low Reynolds numbers, i.e. $Re < 200$. These four classes of predictive models are discussed in Appendix E.

4.2 General Design Procedures. Design procedures and prediction methods for the vortex-excited oscillations of structures and cable systems have been developed only recently. Previously a reliable experimental data base and accurate characterization of the phenomenon were relatively unavailable, and it is only since marine construction has moved into deeper water (and more harsh operating environments) and since the requirements of oceanographers and acousticians have become more sophisticated that the need for sophisticated design procedures has arisen. The need to design slender, flexible structures against problems due to vortex shedding in the atmospheric environment also has spurred renewed efforts to develop new wind engineering design procedures. It should be emphasized, however, that reliable data are now available only at subcritical Reynolds numbers.

The design procedures that are available have been reported by Hallam, Heaf and Wootton (68), King (2), and Skop, Griffin and Ramberg (59,69). These various approaches have been unified on a common basis by Griffin (3). The following discussion is structured similarly to those of Hallam et al. and King, whose primary applications thus far have been to the design of marine structures. The methods developed by Skop, Griffin, and Ramberg have been applied primarily to the analysis of marine cable systems, though many of their basic findings have been incorporated by others in the marine industry (70). Blevins (71) discusses design problems due to flow-induced vibrations in general, including heat exchangers, overhead transmission lines and marine structures and cables.

A general flowchart which lays out a calculation procedure for assessing the response of a structure or cable due to vortex shedding is given in Fig. 4.1. Both single members and arrays of members

are considered in the general procedure, but emphasis is placed here on the case of a single flexible cylinder or cable. The reader should consult references 2 and 68 for further discussions of arrays of structural members. A second flowchart that describes the steps necessary to compute the amplified drag forces and steady deflections is given in Fig. 4.2.

All of the methods developed thus far are in agreement that the following parameters determine whether large-amplitude, vortex-excited oscillations will occur (3):

- the *logarithmic decrement* of *structural* damping, δ
- the reduced velocity, $V/f_n D$
- the mass ratio, $m_e/\rho D^2$.

Here m_e is the *effective mass* of the structure which is defined as

$$m_e = \frac{\int_0^L m(x)\, y^2(x)\, dx}{\int_0^L y^2(x)\, dx} \tag{4.2.1}$$

where $m(x)$ is the mass per unit length including contributions due to internal water, fluid added mass, joints, sections of different material, etc.,

$y(x)$ is the modal shape of the structure or cable along its length,

L is the overall length of the structure or cable, measured from its termination.

The effective mass m_e defines an equivalent structure whose vibrational kinetic energy is equal to that of the real structure. In the context of cable strumming, this equation is generally applicable to bare cables and to cables with attached masses.

As described in the previous sections the mass parameter and the structural damping can be combined as

$$k_s = \frac{2m_e\delta}{\rho D^2} \quad \text{or} \quad \frac{\zeta_s}{\mu} = 2\pi St^2 k_s ,$$

which are called the reduced damping. As noted by Hallam, et al. (68), the reduced damping k_s is the ratio of the actual damping *force* (per unit length) and $\rho f_n D^2$, which may be considered as an inertial force (per unit length). The results in the preceding sections also suggest criteria for determining the critical incident flow velocities for the onset of vortex-excited motions. They are:

$$V_{crit} = (f_n D) V_{r,crit}$$

where $V_{r,crit} = 1.2$ for in-line oscillations and $V_{r,crit} = 3.5$ for cross flow oscillations at Reynolds numbers greater than about $5(10^5)$. For Reynolds numbers below 10^5, $V_{r,crit} = 5$, which is a typical value for cable strumming applications.

An increase in the reduced damping will result in smaller amplitudes of oscillation and at large enough values of ζ_s/μ or k_s the vibratory motion becomes negligible. Reference to Fig. 2.2 suggests that oscillations are effectively suppressed at $\zeta_s/\mu > 4$ (or $k_s > 16$), but cylindrical marine structures and marine cables fall well toward the left-hand portion of the figure. The measurements of in-line oscillations by King (46) have shown that vortex-excited motions in that direction are effectively negligible for $k_s > 1.2$. The results obtained by Dean, Milligan and Wootton (5) and others shown on Fig. 2.2 indicate that the reduced damping can increase from $\zeta_s/\mu = 0.01$ to 0.5 (a factor of *fifty*) and the peak-to-peak displacement amplitude is decreased only from 2 to 3 diameters to 1 diameter (a nominal factor of only *two or three*). At the small mass ratios and structural damping ratios that are typical of light, flexible structures in water, the hydrodynamic forces predominate; it is difficult to reduce or suppress the oscillations by means of mass and damping control in that range of parameters. Typical values of k_s for marine cables are given in Fig. 3.10.

Step-by-step procedures for determining the deflections that result from vortex-excited oscillations have been developed by Skop, Griffin and Ramberg (59,69), by King (2), by Hallam, et al. (68) and by Griffin (3). The steps to be taken are explained in detail in these references and generally should follow the sequence given most recently in reference (3):

- Compute/measure vibration properties of the structure or cable system (natural frequencies or periods, normal modes, modal scaling factors, etc.)

- Compute Strouhal frequencies and test for critical velocities, V_{crit} (in-line and cross flow), based upon the incident flow environment.

- Test for reduced damping, k_s, based upon the structural damping and mass characteristics of the structure or cable.

If the cable system or structure is vulnerable to vortex-excited oscillations, then

- Determine vortex-excited unsteady displacement amplitudes and corresponding steady-state deflections based upon steady drag augmentation according to the methods of reference (59), if applicable (see Fig. 4.2);

- Determine new stress distributions based upon the new steady-state deflection and the superimposed forced mode shape caused by the unsteady forces, displacements and accelerations due to vortex shedding.

- Assess the severity of the augmented stress levels relative to fatigue life, critical stresses, etc.

4.3 Practical Design Data. Several dynamic models of varying levels of sophistication have been developed to predict the displacement amplitudes that are excited by vortex shedding. One class of models, the so-called nonlinear "wake-oscillator" type, has been described briefly here and in more detail in Appendix D. None of the wake-oscillator formulations proposed thus far has been developed to the stage where it truly represents a practical procedure for detailed design of structures in both air and water, but, based upon a detailed study, Dean and Wootton (72) have suggested that the wake-oscillator model of Skop and Griffin (see Appendix D) is perhaps the most promising for additional development. At present the wake oscillator model of Appendix D has been used with considerable success in the derivation of scale factors such as those in equations (2.3) and (4.3.1).

Several empirical predictions of the dependence between the peak cross flow displacement amplitude and the reduced damping have been developed over the past several years. The three most widely

used are listed in Table 4.1. The prediction curve developed by Griffin, Skop and Ramberg (69) is a least-squares fit to those data points in Fig. 2.2 that were available in 1976 (about two-thirds of the points now appearing in the figure). The Iwan and Blevins curve was developed during a study of one wake-oscillator formulation (8) and Sarpkaya's result is based upon a modeling study (1) similar to the one described in Appendix E. The dimensionless mode shape factor γ is given by

$$\gamma_i = |\psi_i(z)|_{MAX}/I_i^{1/2}. \tag{4.3.1}$$

Representative maximum values of γ_i for different end conditions and mode shapes can be calculated from the results in Table E1 in Appendix E.

All of the equations in Table 4.1 correctly model the self-limiting displacement amplitude that is shown at small values of reduced damping in Fig. 2.2. It is also important to note that all of these models are based upon the *structural damping ratio,* typically *the still air value,* for whatever mode of the structure is excited (see Appendix E). The models in Tables 4.1 tend to overpredict the cross flow displacement amplitude at $\bar{Y}/D < 0.05$ to 0.1 where the vortex shedding is not fully correlated over the length of the cylinder, but these small-amplitude cross flow oscillations are of more concern in gas flows rather than in water.

Table 4.1. Predictions of Cross Flow Displacement Amplitude Due to Resonant Vortex-Excited Oscillations as a Function of the Reduced Damping

Investigator	Predicted Displacement Amplitude
Griffin, Skop and Ramberg (69)	$\bar{Y}/D = \dfrac{1.29\gamma}{[1 + 0.43(2\pi St^2 k_s)]^{3.35}}$
Blevins (71)	$\bar{Y}/D = \dfrac{0.07\gamma}{(1.9 + k_s)St^2}\left[0.3 + \dfrac{0.72}{(1.9 + k_s)St}\right]^{1/2}$
Sarpkaya (1)	$\bar{Y}/D = \dfrac{0.32\gamma}{[0.06 + (2\pi St^2 k_s)^2]^{1/2}}$

Legend: $\bar{Y}$ = displacement amplitude; D = cylinder diameter; m = mass or equivalent mass (equation (4.2.1)) per unit length; St = Strouhal number; k_s = reduced damping (equation 2.2)); γ = dimensionless mode shape factor (equation (4.3.1)), $\gamma = 1$ for a spring-mounted rigid cylinder, $\gamma = 1.3$ for the first mode of a cantilever, and $\gamma = 1.16$ for a sinusoidal mode shape (cable).

The drag coefficient C_D for a structure vibrating due to vortex shedding is increased as shown in Fig. 2.9. The ratio of C_D and C_{DO} (the latter is the drag coefficient for a cylinder, cable or other flexible bluff structure that is restrained from oscillating) is a function of the displacement amplitude and frequency as given by the response parameter (59)

$$w_r = (1 + 2\bar{Y}/D)(V_r St)^{-1}. \tag{4.3.2}$$

Here again $2\bar{Y}$ is the double amplitude of the displacement, V_r is the reduced velocity and St is the Strouhal number. The ratio of the drag coefficients is given by

$$C_D/C_{DO} = 1\ , \quad w_r < 1 \tag{4.3.3a}$$

$$C_D/C_{DO} = 1 + 1.16(w_r - 1)^{0.65},\ w_r \geq 1 \tag{4.3.3b}$$

which is a least-squares fit to the data in Fig. 2.9. The equation

$$\bar{Y}_{MAX}/D = \frac{1.29\gamma_i}{[1 + 0.43(2\pi St^2 k_s)]^{3.35}} \tag{4.3.4}$$

can be combined with equations (4.3.2) and (4.3.3) to compute the unsteady displacements, the drag amplification and the amplified static deflection that is due to the vortex excited oscillations. The local displacement amplitude along a flexible cylindrical structure (in the *ith* normal mode) is given by

$$\bar{y}(z) = \bar{Y}_i(z)\sin(2\pi ft).$$

where

$$\bar{Y}_i(z) = Y_{EFF,MAX}\ D\ \psi_i(z)/I_i^{1/2}$$

These equations are employed as outlined in Fig. 4.2 to iteratively compute the static deflection of a structure or cable due to vortex-excited drag amplification (the drag coefficient C_{DO} for the stationary cylinder or cable is assumed to be known).

Blevins and Burton (21) have developed a random vibration model for predicting vortex-excited cross flow displacement amplitudes. As noted in Section 4.1 and Appendix E, the model is based upon random vibration theory in order to incorporate the effects of varying correlation length on the resonant response of the structure and the flow-induced forces. The details of the model are given by Blevins and Burton (21,71), and will not be repeated here since the variable correlation length effects are more

applicable at cross flow displacements less that $\overline{Y}/D = 0.2$ and reduced dampings greater than $\zeta_s/\mu = 2$. This is somewhat beyond the range in Fig. 2.2 that is most applicable to marine structures and cable systems.

In order to specify the excitation component of the lift forces, Blevins and Burton fitted a quadratic curve to the data of Vickery and Watkins (1964) and Hartlen, Baines and Currie (1968) that are plotted in Fig. 2.7. The curve is given by

$$C_{LE}(z) = a + b|\psi_i(z)|\ Y_{MAX} + c|\psi_i(z)|^2\ Y_{MAX}^2 \tag{4.3.5a}$$

with $a = 0.35$, $b = 0.60$ and $c = -0.93$, and C_{LE} is evaluated from the equation

$$C_{LE} = \frac{\int_0^L C_{LE}(z)\,\psi_i(z)\,dz}{\int_0^L \psi_i(z)\,dz} \tag{4.3.5b}$$

which is discussed in Appendix E.1. Blevins (71) has carried out the necessary integrations for a rigid cylinder ($\psi(z) = 1$), a pivoted rod ($\psi(z) = z/L$) and a sine (taut cable) mode ($\psi_i(z) = \sin(i\pi z/L)$). The results are listed in Table 4.2 for the case where the correlation length l_c is much larger than the length L of the cylinder. The calculation of additional cases is straightforward.

Table 4.2 Excitation Force Coefficient C_{LE}^1 for Three Cylindrical Structures; from reference 71.

Structure	Mode Shape $\psi_i(z)$	C_{LE} $(l_c > L)^-$
Rigid cylinder	1	$a + b(\overline{Y}/D) + c(\overline{Y}/D)^2$
Pivoted rod	$\overline{z}/L$	$a + \frac{2}{3}\,b(\overline{Y}/D) + \frac{c}{2}(\overline{Y}/D)^2$
Sine (taut cable) mode, $i = 1$	$\sin(\pi\overline{z}/L)$	$a + \frac{\pi}{4}\,b(\overline{Y}/D) + \frac{2}{3}\,c(\overline{Y}/D)^2$

[1] C_{LE} is the average value calculated from equations (4.3.5a) and (4.3.5b). $\overline{Y}/D$ is the peak displacement amplitude for a given mode. $a = 0.35$, $b = 0.60$, $c = -0.93$

The coefficients for a cubic fit to the data in Fig. 2.7 have been computed and are based upon a fit to all of the data points shown there. This cubic equation is given by

$$C_{LE} = a_1 + b_1 Y_{EFF,MAX} + c_1 Y_{EFF,MAX}^2 + d_1 Y_{EFF,MAX}^3 \tag{4.3.6}$$

These new coefficients are listed as a_1, b_1, c_1 and d_1 in Table 4.3. This fitted curve to the data is considered to be valid between $Y_{EFF,MAX} = 0$ and $Y_{EFF,MAX} = 1.25$ ($2Y_{EFF,MAX} = 2.5$). The results in the table can be employed as inputs to a predictive model for the strumming oscillations of a flexible cable according to the methods described in Appendices D and E. However, it should be noted that the coefficient C_{LE} represents only the excitation force on the structure or cable. For vibrations in water it is necessary to have an accurate and precise representation of the coefficients of the added mass, hydrodynamic damping and hydrodynamic inertia forces. These coefficients are not as well characterized as C_{LE}, but they can be derived from the total force measurements of Sarpkaya (28), for example, as shown in Table 2.3 and Appendix E.

Table 4.3 Excitation Force Coefficient $C_{LE}^{\dagger}$; data from Fig. 4.9

Force coefficient: $C_{LE} = a_1 + b_1 Y_{EFF,MAX} + c_1 Y_{EFF,MAX}^2 + d_1 Y_{EFF,MAX}^3$
where $a_1 = 0.12$, $b_1 = 2.12$, $c_1 = -3.57$, $d_1 = 1.45$
and the standard deviation of the curve $\sigma = 0.1$.

Effective displacement: $Y_{EFF,MAX} = \dfrac{(\bar{Y}_{MAX}/D)}{\gamma_i}$, $\gamma_i = \dfrac{|\psi_i(z)|_{MAX}}{I_i^{1/2}}$

In terms of $\bar{Y}_{MAX}/D$,

$$C_{LE}|_{\bar{Y}_{MAX}} = a_1 + (b_1/\gamma_i)(\bar{Y}_{MAX}/D) + (c_1/\gamma_i^2)(\bar{Y}_{MAX}/D)^2 + (d_1/\gamma_i^3)(\bar{Y}_{MAX}/D)^3$$

where the factor γ_i is evaluated for a given set of end fixities, i.e. free-pinned, pinned-pinned, clamped-clamped, etc. Hence $\bar{Y}_{MAX}/D$ is the *peak* displacement along the beam. The factor γ_i can be calculated from the data listed in Table E1.

†Note that this form of the equation is slightly different than introduced by Blevins (71) as given in equation (4.3.5a)

Several handbooks and catalogues of relevant data are available to augment the results contained in this report. These include a survey of steady drag coefficients for cables subjected to cross flow currents (73), a detailed handbook of hydrodynamic coefficients for moored array components (74), and a book in which the practical aspects of moored cable and buoy engineering are discussed (75). The report by Dalton (73) is a compilation of steady drag coefficients for stranded steel and synthetic fiber cables. These data are tabulated according to the source and in each case a critical assessment is made concerning the reliability of the experimental findings. The report by Pattison, Rispin and Tsai

(74) is a lengthy and detailed compilation of hydrodynamic force coefficients for moored array components of various shapes (cylinders, spheres, spheriods, streamlined bodies, etc.) and for cables and cable fairings. The authors also make an assessment of the quality and quantity of the experimental data that they include in their report. Solutions to a number of example problems are given in order to illustrate the application of the data.

The book by Berteaux (75) is intended to serve as a text for a graduate course in buoy engineering. Topics that are discussed include the mechanics of floating bodies, and the static and dynamic analysis of mooring lines. Both single point moors and multi-leg systems are considered. The final section of the book is concerned with the design of moored and free drifting buoy systems. Problems due to corrosion, fatigue, strumming and fishbite also are discussed.

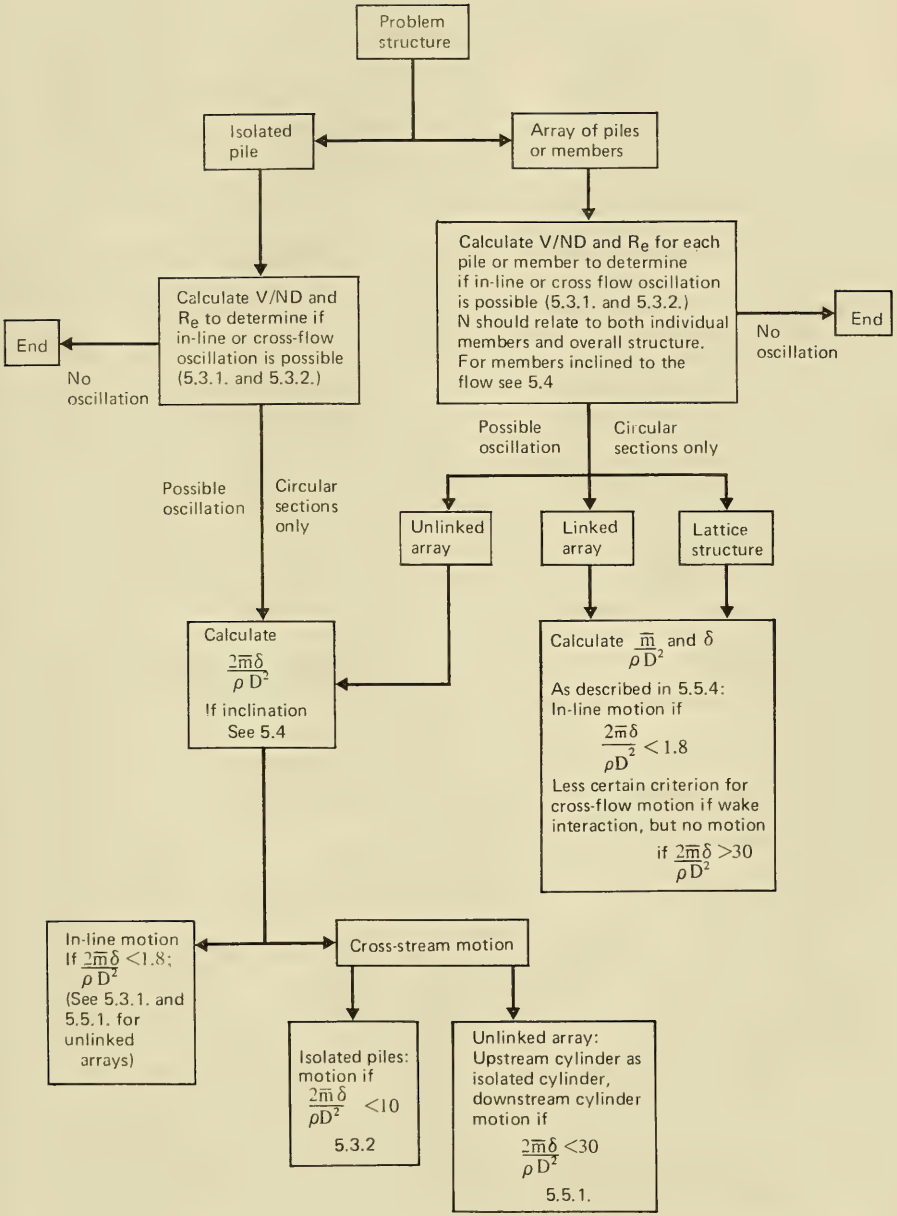

Figure 4.1 Flow diagram of the steps required for the calculation of the response of the structure due to vortex shedding; adapted from Hallam, and Wootton (68). Numbers in the boxes refer to relevant sections of reference 68. The same general procedures apply to an analysis of the strumming vibrations of marine cables.

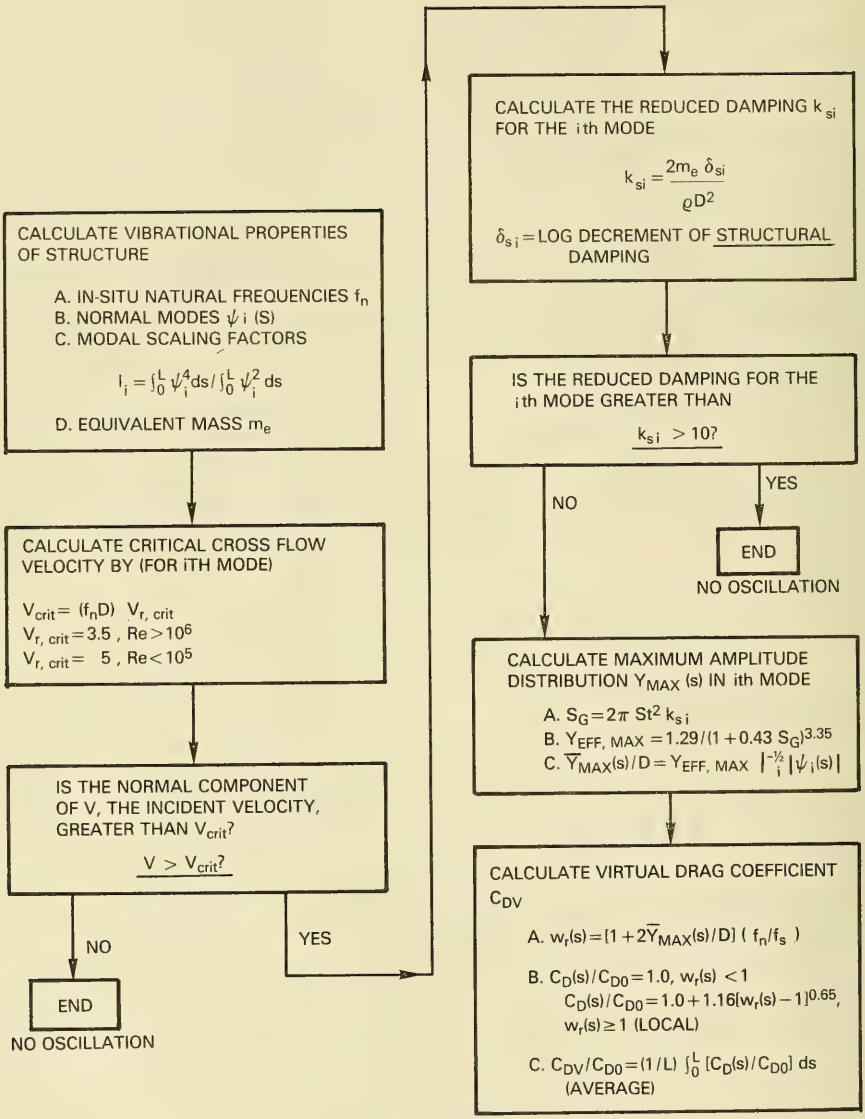

Figure 4.2 Flow diagram of the steps required for the calculation of the steady drag amplification due to vortex-excited oscillations; from Griffin (3). This procedure originally was developed for an analysis of the SEACON II experimental mooring (59).

5.0 NUMERICAL MODELS FOR STRUMMING ANALYSIS AND ASSOCIATED STRUCTURAL MODELING

As the state of the ocean engineering art steadily progresses, more and more stringent demands are being placed upon the performance of cable structures. In particular, displacement tolerances and constraints in response to currents are ever tightening; fatigue is becoming an important design consideration; and the sensitivity of acoustic sensors has become such that they cannot differentiate between legitimate acoustic targets and slight variations in their vertical position. All of these are problems that are aggravated by strumming.

In order for an engineer to be able to design a structure to meet the constraints imposed by his own and other disciplines, he must be able to assess the effect of strumming on the structure in question. Numerical techniques to predict strumming have been developed using the models described in this report as well as other models which account for the effect of strumming on cable structures. For the most part, the strumming and structural analysis models are separate; however, a few codes have integrated the two types of analyses. The earliest codes that accounted for strumming were static models that allowed the user to specify drag coefficients; other codes performed the strumming analysis and supplied the drag coefficients. Recently, the capability to do strumming calculations continuously has been incorporated into a dynamic model. This allows strumming effects to be modeled and updated virtually continuously as a cable system changes geometry.

5.1 NATFREQ, a Strumming Prediction Model. NATFREQ is being developed by CEL for calculating natural frequencies, mode shapes, and drag amplification factors for taut cables with attached masses. Drag amplification factors calculated by NATFREQ using the Skop-Griffin strumming model are used as inputs to the DESADE and DECEL1 structural analysis models. The solution technique is based on a new, efficient iterative algorithm (76). The computed results have been compared to simple laboratory experiments with good agreement. Mode shapes generated by the algorithm for modes 5 and 7 of the experimental cable with six unequally spaced attached masses are given in Fig. 5.1. One of the cases analyzed using the algorithm was a 4700 m (15,400 ft) cable with 380 attached bodies. The

calculated mode shape for mode number 162 is shown in Fig. 5.2. This mode is excited by current velocities near one knot and thus is likely to occur in practice. The complexity of the response is evident.

An accurate prediction of the strumming-induced drag amplification depends upon accurate knowledge of the natural frequencies and mode shapes of the cables in their higher modes. When the cable system has large numbers of attached masses, the prediction of the cable modes and frequencies must be done numerically. NATFREQ is ideally suited to this type of analysis.

5.2 Static Cable Structure Analysis Models.

5.2.1 The DESADE Code. DESADE was developed by NRL for computing the current-induced static deflections of cable structures (58). The solution technique is the method of imaginary reactions. This is a powerful method that usually converges rapidly; however, it has been shown to be sensitive to problems where the cable tension is low and/or the current velocity is high. DESADE can accommodate a complex cable structure with multiple interconnections and a variety of cable materials. An option exists to perform parametric studies to determine the effect of structural changes or various current regimes on the deformation response. Strumming of the cables can be handled by specifying increased drag coefficients obtained from other models.

A simplified approach to the drag amplification routine in DESADE has been described for application to mooring system design (77). The code also has been employed recently in a design study (78) of the riser power cable segment that provides the link between a floating OTEC power plant and the bottom-resting cable segment that transmits electric power to shore. The required input to the program is listed in detail in reference 58, and the code is available to interested users from NRL or CEL.

The importance of including increased drag due to strumming was made apparent in a comparison between the DESADE model and data from an at-sea cable structure experiment. This was the SEACON II structure; it is discussed in reference 57 and in Section 3.4 of this report. Results from the comparison with the SEACON II data are shown in Fig. 3.19.

The cables comprising the delta module of the SEACON array had uniform currents incident over their lengths and were found to be subject to cable strumming. As shown in Section 4.3, the strumming vibrations lead to increases in the effective steady drag coefficients. Since the steady drag coefficient is a basic parameter in all array motion computations, an accurate knowledge of its value is required in order to validate the various models for the analysis of cable structures.

The calculated steady drag coefficient was frequently 150 to 230% greater than the value of the nominal stationary-cable drag coefficient C_{DO} because of strumming of the SEACON II array. Large increases in the resulting drag loads would be expected to have a significant effect on the magnitude of the predicted array motions. In Fig. 5.3 the measured motions of a point near the intersection of two cables on the horizontal delta of the SEACON II array are compared to the predicted motions during a semi-diurnal tidal cycle. The calculated motions were obtained using the computer code DESADE. The magnitude and direction (predominantly from the southeast) of the current during the cycle can be inferred from the movement of the measurement point from its zero current location designated by "*X*." The North direction is shown on the plot as a reference.

The measured motion of the point is shown in Fig. 5.3 by the solid line, and the predicted motion using a constant stationary-cable drag coefficient $C_{DO} = 1.55$ (measured in water (57) on a sample of the SEACON II cable) is given by the dashed line with circles (---0---). Finally, the predicted motion using $C_D = (C_D/C_{DO})C_{DO}$, with C_D/C_{DO} calculated from equation (4.3.3) and $C_{DO} = 1.55$, is shown by the dashed line (-----). Excellent agreement was obtained between the predicted and measured motions when the strumming-amplified steady drag coefficients were employed. It was also apparent, for the larger current magnitudes, that the displacement amplitudes predicted using the nominal stationary-cable drag coefficient ($C_{DO} = 1.55$) were considerably smaller than the measured displacements. As noted in Section 3.4, the delta cables of the SEACON II array did not undergo a pure mode, resonant lock-on response to the strumming forces. However, the strumming-amplified drag coefficients measured during well-controlled laboratory experiments that were characterized by resonant lock-on have been validated for applications in practice by the SEACON II computations and measured array motions.

5.2.2 Variations of DESADE. CEL has made modifications to its version of DESADE resulting in the re-named program DECEL1. The modifications include: user conveniences; plotting of structure shape and current field; iteration limits to prevent unexpected high execution costs; and three dimensional current field specification using data from up to four current meter strings. A new users manual (79) has been prepared that includes experience gained from using the program.

5.3 Other Computer Codes. DESADE is one of two existing cable structure models that explicitly takes account of strumming-induced hydrodynamic force amplifications of marine cables. However, other codes to predict vortex-excited oscillations are being developed because of the importance of vortex shedding-related problems in marine applications. VORTOS is a computer code developed by Atkins Research and Development in the the United Kingdom. The essential features of the code are described in a recently published report (80). This program predicts the dynamic response of a flexible cylinder to vortex-excited oscillations in steady flow. The vibration amplitude and frequency response in a steady flow may be calculated for flexible cylindrical members of a variety of marine structures. The calculation is based upon experimental measurements of the cross flow response and the excitation forces using spring-mounted rigid cylinders and flexible cylinders (5).

The program is based upon the well-founded assumption that the lift force at each position along the length of a cylinder in steady flow is a sinusoidal function of time and is dependent upon the local incident flow velocity and the displacement amplitude. This point is discussed in Section 2 of this report. The structure is represented by simple finite elements (at this stage up to eleven in number) and the appropriate mass and stiffness matrices. The vortex shedding frequency is determined from the reduced velocity V_r for each element and is assumed to lock-on close to the natural frequency of the structure at the critical velocities described in Sections 2, 3 and 4 of this report. More specifically, lock-on is assumed to occur if the Strouhal frequency ω_s is between 0.8 ω_n and 1.6 ω_n (80). The resonant, vortex-excited lift forces as a function of displacement amplitude for each vibrating element are derived from experimental data. An iterative procedure is employed to calculate the steady-state deflected shape of the cylindrical member and the maximum bending stress are determined from the

curvature. A typical comparison between the VORTOS prediction and experimental measurements taken with a long, flexible circular beam is plotted in Fig. 5.4.

The flexible cylinder of diameter $D = 25$ mm (1 in.) employed in this example was very much like a cable since it had an aspect ratio of $L/D = 240$ and a low value of structural damping. The important features of the code are described in more detail in reference 80, which also includes a worked example problem with output and a listing of the input data required to exercise the code.

A computer code, MARISE, for the analysis of marine riser dynamics has been developed by the Shell Development Company. This code recently was modified to accommodate a wake-oscillator type of vortex shedding analysis (40). Predictions have been made of the oscillatory behavior of Cognac platform piles in various configurations during lowering and driving operations (16,40). Fair agreement was obtained between the MARISE predictions and model test results such as those shown in Fig. 2.24. Several additional marine riser dynamics codes that model the resonant vortex/structure interaction are discussed briefly in reference 3.

5.4 SEADYN, a Dynamic Analysis Model. SEADYN is a nonlinear finite element cable system model being developed by CEL. Both the static and dynamic behavior of cable systems can be simulated. A wide variety of situations can be modeled, including: pay-out and reel-in, time varying current fields, point loads and surface excitations.

The Skop-Griffin strumming model has been incorporated into SEADYN. Strumming calculations are updated in a dynamic simulation whenever the relative velocity of the cable through the water changes by 10%. This is an arbitrary interval and can be changed by the user. To date, the strumming calculation option has been used infrequently because of the disparity between the relatively small number of nodes required for adequate hydrodynamic modeling as compared to the large number required to obtain an adequate description of mode shape for the strumming model. Modeling with a large number of nodes results in a large cost penalty in computing the gross response of the cable. A

more efficient, fast algorithm such as the one used in NATFREQ could be adapted to perform cost effective strumming calculations. SEADYN has a default, Reynolds number-dependent drag coefficient builtin, but this can be over-ridden if the user specifies a drag coefficient or function based on other independent knowledge or calculations.

5.5 The SLAK Code. A finite element code for predicting the natural frequencies and mode shapes of slack cables has been developed from a previously existing code as part of this cable dynamics research program. A finite element formulation is employed and the range of validity is not limited to small sag-to-span ratios, ($s/l < 0.12$) as are most existing linear theories. The code is also valid for arbitrary locations of the end points (i.e. an inclined cable), it is three-dimensional, and it permits concentrated applied loads (attached discrete masses) at various locations along the cable. The principal results that are obtained from the code in its present form are the (in-air) natural frequencies, the support reaction forces, the equilibrium shape of the cable, and the natural mode shapes with respect to the equilibrium shape. The code is called SLAK and it is discussed in further detail in Appendix B of this report.

These numerical models represent the first generation of cable strumming analyses. As more experience is gained using these models, other ideas and techniques for improving the state of the art of calculating the effects of strumming on marine structures undoubtedly will evolve. At the present time, these models represent the current understanding of strumming effects.

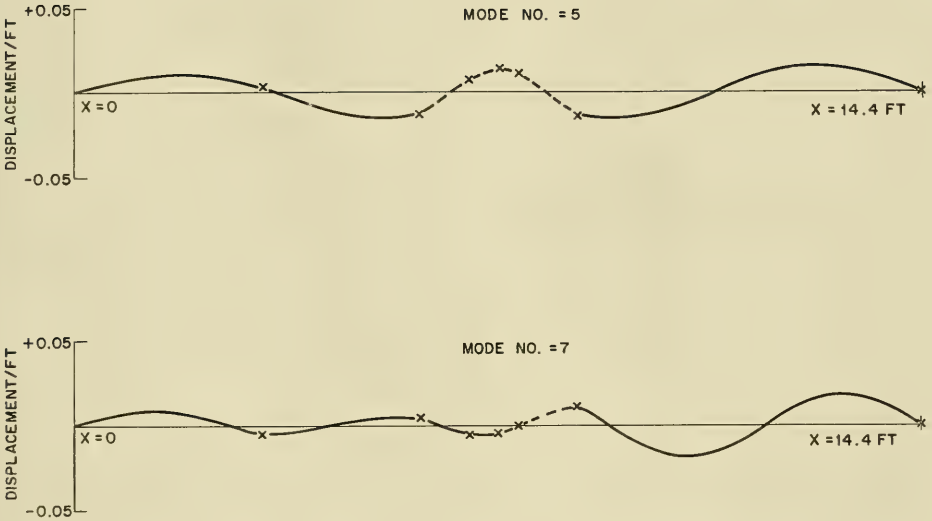

Figure 5.1 The computer representation of the $n = 5$ and $n = 7$ modes of an experimental cable with six unequally-spaced attached masses; from Sergev and Iwan (76).

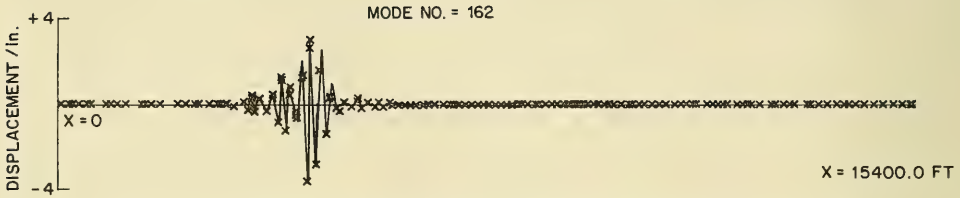

Figure 5.2 The calculated mode shape (mode number $n = 162$) for a 4700 m (15400 ft) long marine cable with 380 attached masses; from Sergev and Iwan (76).

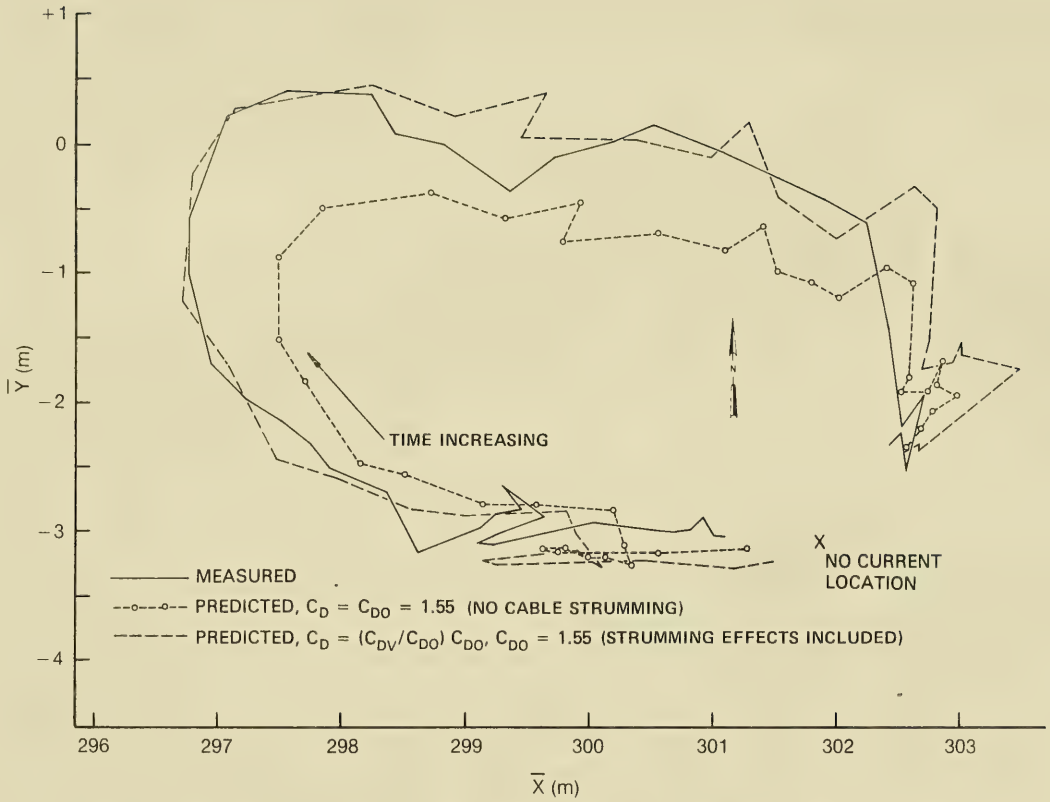

Figure 5.3 A comparison of the measured and predicted motions of a point near the intersections of cables 1 and 3 on the SEACON II delta (59). The time period covered is a semidiurnal tidal cycle from 2120, 12/11/75 to 0920, 12/12/75. The drag coefficient C_{DO} was measured in water on a short segment of the SEACON delta cable, $D = 18.5$ mm (0.75 in.).

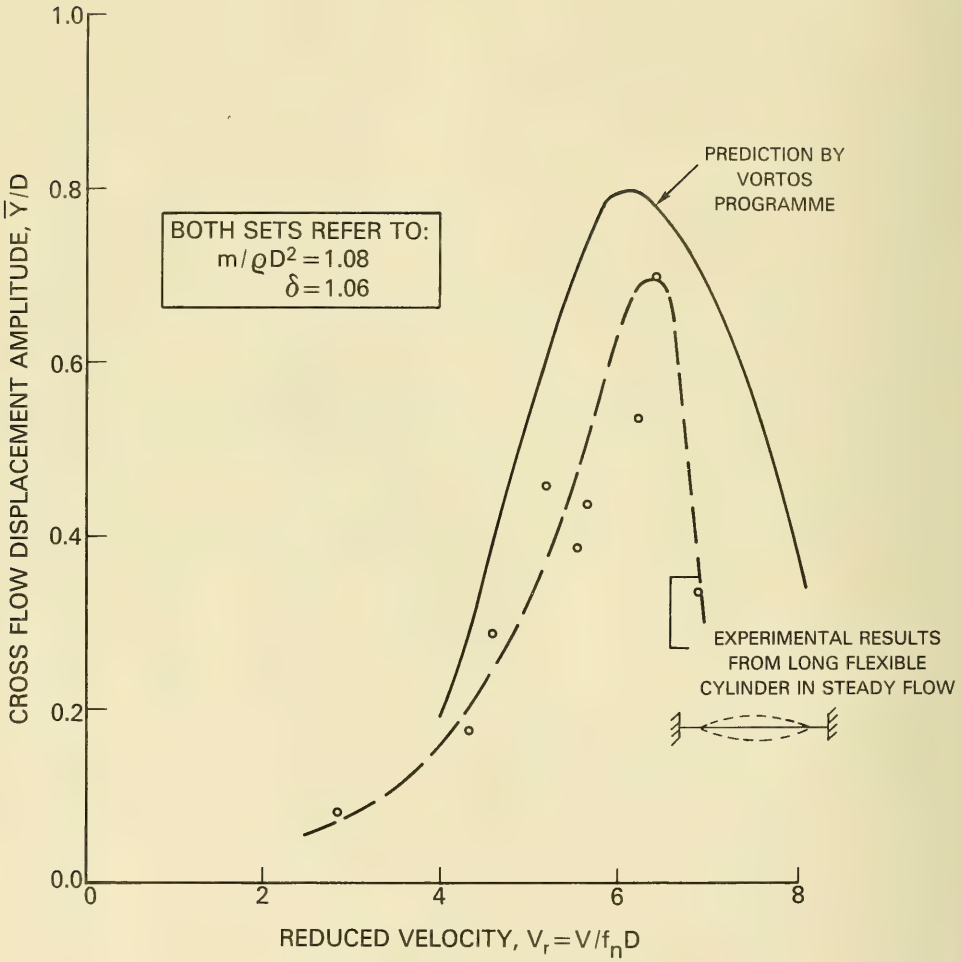

Figure 5.4 A comparison of the measured cross flow oscillations (from equilibrium) of a flexible cylinder with the predicted response from the VORTOS code; from Dean and Wootton (72).

6. SUMMARY

6.1 Findings and Conclusions. Problems associated with the shedding of vortices often have been overlooked or crudely approached on an ad hoc basis in the past in relation to the design of marine structures and cable systems, largely because reliable experimental data and design procedures have not been available. However, the dynamic analysis of marine structures and cable systems has become increasingly important and sophisticated in order to accurately predict stress distributions and operational lifetimes in the ocean environment. The strumming of marine cables has serious consequences because these vibrations are a potential cause of fatigue for system components and they are a cause of increased hydrodynamic drag. Strumming vibrations also introduce acoustic noise in sensor components attached to the cable and they cause abrasion and wear of fittings and of the cables themselves.

This report has summarized the present state-of-the-art concerning the strumming vibrations of marine cables. Reliable data now are in hand for the dynamic response of and hydrodynamic forces on model-scale structures and cables, and based upon these findings empirical and semi-empirical prediction models have been developed and calibrated for use in practice. Many, if not most, of these findings have come from the marine cable dynamics program of the Naval Facilities Engineering Command. The results of this program are reported in detail in the various sections and appendices of this report and others (1,12).

Detailed information now is available for the resonant vortex-excited response of model cylindrical structures and cables that oscillate at subcritical Reynolds numbers, i.e. $Re < 2(10^5)$. There also is reasonably detailed knowledge of the steady drag amplification that accompanies vortex-excited oscillations. This force amplification causes increased static deflections of the structure or cable and practical design methods have been developed to predict this static deflection, as shown in this report. Unsteady hydrodynamic strumming force coefficients have been measured at moderate Reynolds numbers, $Re = 10^3$ to 10^4, and these coefficients have been employed in the development of the practical design procedures that are described here. Virtually all of the measurements of cylinder and cable dynamic

responses and forces have been made in the Reynolds number range that is directly applicable to cable strumming problems.

6.2 Recommendations. Though reasonable engineering approximations must be made, the procedures and experimental data base presented in this report are recommended for use in cable system design practice. Procedures are described for predicting a particular system's vulnerability to vortex-excited strumming oscillations. In addition, a reasonable data base from dynamic response and force coefficient measurements is also provided to aid in detailed calculations of the system response, if that is necessary. A number of computer codes also are available to assist the designer and some have been calibrated against both field-scale and laboratory-scale test data.

7. REFERENCES

1. T. Sarpkaya, "Vortex-Induced Oscillations, A Selective Review" Transactions of ASME, Journal of Applied Mechanics, Vol. 46, pp. 241-258, 1979.

2. R. King, "A Review of Vortex Shedding Research and Its Application," Ocean Engineering, Vol. 4, pp. 141-171, 1977.

3. O.M. Griffin, "OTEC Cold Water Pipe Design for Problems Caused by Vortex-Excited Oscillations," Naval Research Laboratory Memorandum Report 4157, March 1980.

4. O.M. Griffin and G.H. Koopmann, "The Vortex-Excited Lift and Reaction Forces on Resonantly Vibrating Cylinders," Journal of Sound and Vibration, Vol. 54, pp. 435-448, 1977.

5. R.B. Dean, R.W. Milligan and L.R. Wootton, "An Experimental Study of Flow-Induced Vibration," E.E.C. Report 4, Atkins Research and Development, Epsom (U.K.), 1977.

6. O.M. Griffin, "Vortex-Excited Cross Flow Vibrations of a Single Cylindrical Tube", Transactions of ASME, Journal of Pressure Vessel Technology, Vol. 102, pp. 158-166, 1980; see also *Flow-Induced Vibrations,* S.S. Chen and M.D. Bernstein (eds.), ASME: New York, 1-10, 1979.

7. B.J. Vickery and R.D. Watkins, "Flow Induced Vibration of Cylindrical Structures," Proceedings of the First Australian Conference on Hydraulics and Fluid Mechanics, R. Silvester (ed.), Pergamon Press: New York, 1964.

8. W.D. Iwan, "The Vortex-Excited Oscillations of Elastic Structural Elements," Transactions of ASME, Journal of Engineering for Industry, Vol. 97, pp. 1378-1382, 1975.

9. R.A. Skop and O.M. Griffin, "On a Theory for the Vortex-Excited Oscillations of Flexible Cylindrical Structures" Journal of Sound and Vibration, vol. 41, 263-274, 1975; see also "The Vortex-Excited Oscillations of Structures," Journal of Sound and Vibration, Vol. 44, pp. 303-305, 1976.

10. R. King, "Vortex Excited Oscillations of Inclined (Yawed) Cylinders in Flowing Water," BHRA Fluid Engineering Report RR 1214, January 1975.

11. R. King, M.J. Prosser and D.J. Johns, "On Vortex Excitation of Model Piles in Water," Journal of Sound and Vibration, Vol. 29, pp. 169-188, 1973.

12. T. Sarpkaya, "Transverse Oscillation of a Circular Cylinder in Uniform Flow," Proceedings of ASCE, Journal of the Waterways, Port, Coastal and Ocean Division, Vol. 104, pp. 275-290, 1978.

13. J.A. Mercier, "Large Amplitude Oscillations of a Circular Cylinder in a Low-Speed Stream," Ph.D. Thesis, Stevens Institute of Technology, Hoboken NJ, 1973.

14. P.W. Bearman and I.G. Currie, "Pressure Fluctuation Measurements on an Oscillating Circular Cylinder," Journal of Fluid Mechanics, Vol. 91, pp. 661-678, 1979.

15. O.M. Griffin, R.A. Skop and G.H. Koopmann, "The Vortex-Excited Resonant Vibrations of Circular Cylinders" Journal of Sound and Vibration, Vol. 31, pp. 235-249, 1973.

16. R. King, "Model Tests of Vortex Induced Motion of Cable Suspended and Cantilevered Piles for the COGNAC Platform," BHRA Fluid Engineering Report RR 1453, January 1978.

17. G.H. Koopmann, "The Vortex Wakes of Vibrating Cylinders at Low Reynolds Numbers," J. Fluid Mech., Vol. 28, 501-512, 1967.

18. G.H. Toebes, "The Unsteady Flow and Wake Near an Oscillating Cylinder," Transactions of ASME, Journal of Basic Engineering, Vol. 91, pp. 831-838, 1969.

19. M. Novak and H. Tanaka, "Pressure Correlations on a Vibrating Cylinder," in *Proc. Fourth Int. Conf. on Wind Effects on Buildings and Structures,* Heathrow (U.K.), September 1975.

20. J.F. Howell and M. Novak, "Vortex Shedding from a Circular Cylinders in Turbulent Flow" in *Proc. Fifth Int. Conf. Wind Engrg.,* Paper V-11, July 1979.

21. R.D. Blevins and T.E. Burton, "Fluid Forces Induced by Vortex Shedding" Transactions of ASME, Journal of Fluids Engineering., Vol. 98, pp. 19-24, 1976.

22. S.E. Ramberg and O.M. Griffin, "Velocity Correlation and Vortex Spacing in the Wake of a Vibrating Cable," Transactions of ASME, Journal of Fluids Engineering, Vol. 98, pp. 10-18, 1976.

23. S.E. Ramberg and O.M. Griffin, "The Effects of Vortex Coherence, Spacing and Circulation on the Flow-Induced Forces on Vibrating Cables and Bluff Structures," Naval Research Laboratory Report 7945, January 1976.

24. L.R. Wootton, "The Oscillation of Large Circular Stacks in Wind," Proceedings of the Institution of Civil Engineers, Vol. 43, pp. 573-598, 1969.

25. O.M. Griffin, "A Universal Strouhal Number for the 'Locking-on' of Vortex Shedding to the Vibrations of Bluff Cylinders," Journal of Fluid Mechanics, Vol. 85, pp. 591-606, 1978.

26. O.M. Griffin, "Universal Similarity in the Wakes of Stationary and Vibrating Bluff Bodies," Transactions of ASME, Journal of Fluids Engineering, Vol. 103, in press, March 1981.

27. A. Roshko, "On the Wake and Drag of Bluff Bodies," Journal of the Aeronautical Sciences, Vol. 22, pp. 124-132, 1955; see also A. Roshko, "Experiments on the flow past a circular cylinder at very high Reynolds numbers," Journal of Fluid Mechanics, Vol. 10, pp. 345-356, 1961.

28. S.E. Ramberg, "The Influence of Yaw Angle Upon the Wakes of Stationary and Vibrating Cylinders," Naval Research Laboratory Report 3822, August 1978.

29. O.M. Griffin, J.H. Patterson, R.A. Skop, S.E. Ramberg and D.J. Meggitt, "Vortex-Excited Vibrations of Marine Cables," Proceedings of ASCE, Journal of the Waterways, Port, Coastal and Ocean Division, Vol. 106, pp. 183-204, 1980.

30. T. Sarpkaya, "Effect of Surface Roughness on the Transverse Oscillations of a Circular Cylinder," Naval Postgraduate School Report NRS-69SL-79085-IR, August 1979.

31. R.D. Peltzer and D.M. Rooney, "The Effect of Upstream Shear and Surface Roughness on the Vortex Shedding Patterns and Pressure Distributions Around a Circular Cylinder in Transitional *Re* Flows," Virginia Polytechnic Institute and State University Report VPI-Aero-110, April 1980.

32. G. Buresti and A. Lanciotti, "Vortex Shedding From Smooth and Roughened Circular Cylinders in Cross Flow Near a Plane Surface," Aeronautical Quarterly, Vol. 28, pp. 305-321, February 1979.

33. N. Alemdaroglu, J.C. Rebillat and R. Goethals, "An Aeroacoustic Coherence Function Method Applied to Circular Cylinder Flows," Journal of Sound and Vibration, Vol. 69, 427-440, 1980.

34. E. Szechenyi, "Supercritical Reynolds Number Simulation for Two-Dimensional Flow over Circular Cylinder," Journal of Fluid Mechanics, Vol. 70, 529-542 (1975).

35. Y. Nakamura, "Some Research on Aeroelastic Instabilities of Bluff Structural Elements," in *Proc. Fourth Int. Conf. on Wind Effects on Buildings and Structures,* Heathrow (U.K.), 359-368, 1976.

36. B.L. Miller, "The Hydrodynamic Drag of Roughened Circular Cylinders," Transactions of the Royal Society of Nava Architects, Vol. 119, 55-70, 1977.

37. D. Hove, W. Shih and E. Albano, "Hydrodynamic Design Loads for the OTEC Cold Water Pipe," Science Applications, Inc. Report SAI-79-559-LA, September 1978.

38. K.C.S. Kwok and W.H. Melbourne, "Cross-Wind Response of Structures Due to Displacement Dependent Lock-in Excitation," in *Proc. Fifth Int. Conf. on Wind Engrg. (Preprints),* Vol. II, Fort Collins, Co., VI-4, July 1979.

39. P.K. Stansby, "The Locking-on of Vortex Shedding Due to the Cross-Stream Vibration of Circular Cylinders in Uniform and Shear Flows," Journal of Fluid Mechanics, Vol. 74, 641-667, 1976.

40. F.J. Fischer, W.T. Jones and R. King, "Current-Induced Oscillation of Cognac Piles During Installation: Prediction and Measurements," in *Proc. Symp. Practical Experiences with Flow-Induced Vibrations (Preprints),* Karlsruhe, Vol. 1, 216-228, September 1979.

41. J.A. Peterka, J.E. Cermak and H.G.C. Woo, "Experiments on the Behavior of Cables in a Linear Shear Flow," Progress Report on Contract No. N68305-78-C-0055 for the Civil Engineering Laboratory, Naval Construction Battalion Center; Colorado State University (May, August 1980).

42. O.M. Griffin, "Vortex Shedding from Stationary and Vibrating Bluff Bodies in a Shear Flow," Naval Research Laboratory Memorandum Report 4287, August 1980.

43. J. Cermak (ed.), *Proceedings of the Fifth International Conference on Wind Engineering (Preprints),* Colorado State University: Fort Collins, Colorado, July 1979.

44. K.J. Eaton (ed.), *Proceedings of the Fourth International Conference on Wind Effects on Buildings and Structures,* Cambridge University Press: Cambridge, UK, 1976.

45. J.R. Dale, H. Menzel and J. McCandless, "Dynamic Characteristics of Wire Rope: Flow Induced Transverse Vibrations," Naval Air Development Center Report NADC-AE-6620, 1966.

46. R. King, "Vortex-Excited Structural Oscillations of a Circular Cylinder in Steady Currents," Offshore Technology Conference Preprint 1948, 1974.

47. J.R. Dale and J.M. McCandless, "Water Drag Effects of Flow Induced Cable Vibrations," Naval Air Development Center Report NADC-AE-6731, 1967.

48. O.M. Griffin and S.E. Ramberg, "Wind Tunnel Flow Visualization with Liquid Particle Aerosols," in *Flow Visualization*, T. Asanuma (ed.), Hemisphere Publishing Company: Washington, D.C., 65-74, 1979.

49. J.H. Pattison, "Measurement Technique to Obtain Strumming Characteristics of Model Mooring Cables in Uniform Currents," David Taylor Naval Ship Research and Development Center Report SPD 766-01, April 1977.

50. J.H. Pattison, "Measurement Technique to Obtain Strumming Characteristics of Model Mooring Cables in Uniform Currents, Data Supplement," David W. Taylor Naval Ship R & D Center Supplement to Report SPD 776-01, April 1977.

51. J.E. Kline, E. Fitzgerald, C. Taylor and T. Brzoska, "The Dynamic Response of a Moored Hydrophone Housing Assembly Subjected to a Steady Uniform Flow," MAR Inc., Technical Report No. 237, February 1980.

52. B.S. Chung, "Dynamic Properties of Several Wire Ropes Subjected to Axial Load," Ph.D. Dissertation, Catholic University of America; Washington, D.C., 1971.

53. J.K. Vandiver, "A Field Study of Vortex-Excited Vibrations of Marine Cables," Offshore Technology Conference Preprint 2491 (May 1976).

54. J.K. Vandiver and T.P. Pham, "Performance Evaluation of Various Strumming Suppression Devises," MIT Ocean Engineering Department Report 77-2, March 1977.

55. M. Kennedy and J.K. Vandiver, "A Random Vibration Model for Cable Strumming Prediction," Proceedings of CIVIL ENGINEERING IN THE OCEANS IV, ASCE: New York, 273-292, 1979.

56. E.J. Softley, J.F. Dilley and D.A. Rogers, "An Experiment to Correlate Strumming and Fishbite Events on Deep Ocean Moorings," GE Document 77SDR 2181, General Electric Co.: Re-Entry and Environmental Systems Division, 1977.

57. T.R. Kretschmer, G.A. Edgerton and N.D. Albertsen, "Seafloor Construction Experiment, SEACON II; An Instrumented Tri-Moor for Evaluating Undersea Cable Structure Technology," Civil Engineering Laboratory Technical Report R-848, December 1976.

58. R.A. Skop and J. Mark, "A Fortran IV Program for Computing the Static Deflections of Structural Cable Arrays," Naval Research Laboratory Report 7640, August 1973.

59. R.A. Skop, O.M. Griffin and S.E. Ramberg, "Strumming Predictions for the SEACON II Experimental Mooring," Offshore Technology Conference Preprint OTC 2884, 1977.

60. M.B. Kennedy, "A Linear Random Vibration Model for Cable Strumming, Ph.D. Thesis, Massachusetts Institute of Technology, May 1979.

61. R.E.D. Bishop and A.Y. Hassan, "The Lift and Drag Forces on a Circular Cylinder Oscillating in a Flowing Fluid," Proceedings of the Royal Society (London) Series A, Vol. 277, 51-75, 1964.

62. R.A. Skop and O.M. Griffin, "A Model for the Vortex-Excited Oscillations of Bluff Structures," Journal of Sound and Vibration, Vol. 27, 225-233, 1973.

63. W.D. Iwan and R.D. Blevins, "A Model for the Vortex-Induced Oscillation of Structures," Transactions of ASME, Journal of Applied Mechanics, Vol. 41, 581-585, 1975.

64. R.T. Hartlen and I.G. Currie, "A Lift-Oscillator Model for Vortex-Induced Vibrations," Proceedings of the ASCE, Journal of Engineering Mechanics, Vol. 69, 577-591, 1970.

65. S.S. Chen, "Crossflow-Induced Vibrations of Heat Exchanger Tube Banks," Nuclear Engineering and Design, Vol. 47, 67-86, 1978.

66. T. Sarpkaya and R.A. Shoaff, "Numerical Modeling of Vortex-Excited Oscillations," CIVIL ENGINEERING IN THE OCEANS IV, ASCE: New York, 504-517, 1979.

67. S.E. Hurlbut, M.L. Spaulding and F.M. White, "Numerical Solution of the Time Dependent Navier-Stokes Equations in the Presence of an Oscillating Cylinder," in *Numerical Solution of Non-steady Flows,* ASME: New York, 201-206, 1978.

68. M.G. Hallam, N.J. Heaf and L.R. Wootton, *Dynamics of Marine Structures,* Construction Industry Research and Information Association (London) Report UR8, 1978.

69. O.M. Griffin, R.A. Skop and S.E. Ramberg, "The Vortex-Excited Resonant Vibrations of Structures and Cable Systems," Offshore Technology Conference Preprint OTC 2319, 1975.

70. "Wind and Water-Current-Induced Oscillations in Tubulars," Petroleum Engineer International, Vol. 51, No. 12, 46-62, October 1979.

71. R.D. Blevins, *Flow-Induced Vibrations,* Van Nostrand — Reinhold: New York, 1977.

72. R.B. Dean and L.R. Wootton, "An Analysis of Vortex Shedding Problems in Offshore Engineering," Report No. 77/14, Atkins Research and Development, Epsom (V.K.), 1977.

73. W.L. Dalton, "A Survey of Available Data on the Normal Drag Coefficient of Cables Subjected to Cross Flows," Civil Engineering Laboratory Report CR 78.001, Port Hueneme, CA, August 1977.

74. J.H. Pattison, P.P. Rispin and N.T. Tsai, "Handbook on Hydrodynamic Characteristics of Moored

Array Components," David Taylor Naval Ship Research and Development Center Report SPD-745-01, March 1977.

75. H.O. Berteaux, *Buoy Engineering,* Wiley-Interscience: New York, 1979.

76. S. Sergev and W.D. Iwan, "The Natural Frequencies and Mode Shapes of Cables with Attached Masses," Civil Engineering Laboratory, Technical Memorandum M-44-79-3, April 1979.

77. R.A. Skop and F. Rosenthal, "Some New Approximation Techniques for Mooring System Design," Marine Technology Society Journal, Vol. 13, No. 6, 9-13, 1979.

78. R.A. Lindman, J.C. Oliver, W.L. Jawish and P.L. Steiner, "OTEC Riser Cable Loads Analysis and Ocean Engineering Design Criteria," Giannotti and Associates Report No. 79-045-005, May 1980 (Preliminary Report).

79. S. Sergev, "DECEL 1 Users Manual — A Fortran IV Program for Computing the Static Deflections of Structural Cable Arrays," Civil Engineering Laboratory, Technical Note N-1584, August 1980.

80. W.A. Evers and R.B. Dean, "VORTOS — A Program for the Calculation of Vortex-Induced Oscillations in Steady Flow," Atkins Research and Development Report 1978/APR/2, Epsom (V.K.), April 1978.

Appendix A

DYNAMICS OF TAUT MARINE CABLES

A.1 Equation of Motion for a Taut (Stretched) Cable. Consider a uniform cable stretched between rigid supports a distance L apart with an equilibrium position along the x axis and equilibrium tension T_0. The cable has a virtual mass density ρ, cross-sectional area A, elastic modulus E, and a moment of inertia I about the neutral axis z. For simplicity it is assumed transverse oscillations take place only in the xy plane. To account for the damping, we assume a term in the equation linearly proportional to the transverse velocity by a damping coefficient ζ. The coefficient ζ is taken as the damping of the system as measured in still air. This is the usual approach to specifying the *structural damping.* A further discussion of structural and hydrodynamic damping is given in Appendices C and E. Longitudinal displacements are neglected and the transverse displacement at the position x is taken to be $y(x,t)$. Further, for typical cables and the frequencies of flow-induced vibrations, shear deformations and rotary inertia are negligible. The potential energy of the cable is then a sum of bending and stretching potential energies. From elementary beam theory the bending energy is given by

$$1/2 \int_0^L EI \frac{\partial^2 y}{\partial x^2} \, dx. \tag{A1}$$

The approach developed by Murthy and Ramakrishna (A1) is employed here to determine the stretching contribution for the nonlinear vibrations of strings. This is a good approximation for cables that undergo flow-induced "strumming" motions in water. As an element of cable dx is deformed into the planar element ds, the stretched length of the element is

$$ds = (dx^2 + dy^2)^{1/2} = dx \left[1 + \left(\frac{\partial y}{\partial x} \right)^2 \right]^{1/2} \tag{A2}$$

and the local strain is given by

$$\epsilon = \frac{ds - dx}{dx} = \left[1 + \left(\frac{\partial y}{\partial x} \right)^2 \right]^{1/2} - 1. \tag{A3}$$

If the amplitudes are small enough for Hooke's law to be valid, then the local tension is

$$T = T_0 + EA\epsilon \tag{A4}$$

and the local potential energy is equal to the product of the average local tension and the local strain. Expanding the local strain in a power series of $\partial y/\partial x$ and neglecting terms higher than fourth order results in

$$\left[1/2T_0\left(\frac{\partial y}{\partial x}\right)^2 + \frac{EA - T_0}{8}\left(\frac{\partial y}{\partial x}\right)^4\right] dx, \tag{A5}$$

the local potential energy due to stretching. For all practical cases $EA >> T_0$ and the contribution to potential energy from stretching is

$$\int_0^L \left[1/2T_0\left(\frac{\partial y}{\partial x}\right)^2 + \frac{EA}{8}\left(\frac{\partial y}{\partial x}\right)^4\right] dx. \tag{A6}$$

The kinetic energy of the cable in terms of the virtual mass density ρ is given by

$$1/2\int_0^L \rho A\left(\frac{\partial y}{\partial t}\right)^2 dx \tag{A7}$$

and the generalized work due to structural damping per unit length is

$$\int_0^L -\zeta_s \frac{\partial y}{\partial t}\delta y\, dx. \tag{A8}$$

After Hamilton's principle is applied, the final equation of planar cable motion becomes

$$EI\frac{\partial^4 y}{\partial x^4} + \rho A\frac{\partial^2 y}{\partial t^2} - \left[T_0 + \frac{3EA}{2}\left(\frac{\partial y}{\partial x}\right)^2\right]\frac{\partial^2 y}{\partial x^2} + \zeta_s\frac{\partial y}{\partial t} = 0. \tag{A9}$$

It is convenient to transform this equation by

$$\hat{x} = \frac{n\pi x}{L},\ \hat{y} = \frac{y}{Y},\ \hat{t} = \omega t \tag{A10}$$

where n is the mode number, Y is the antinode amplitude, and ω is the frequency of vibration. The resulting equation is

$$\frac{\partial^2 \hat{y}}{\partial t^2} + \frac{EIn^4\pi^4}{\rho A\omega^2 L^4}\frac{\partial^4 \hat{y}}{\partial \hat{x}^4} - \left[\frac{T_0 n^2\pi^2}{\rho AL^2\omega^2} + \frac{3EY^2 n^4\pi^4}{2\rho\omega^2 L^4}\left(\frac{\partial \hat{y}}{\partial \hat{x}}\right)^2\right]\frac{\partial^2 \hat{y}}{\partial \hat{x}^2} + \frac{\delta}{2\pi}\frac{\partial \hat{y}}{\partial \hat{t}} = 0, \tag{A11}$$

in which δ is the log decrement of the vibration ($\delta = 2\pi\zeta_s$ for small damping). The fluid forces that act on a resonantly vibrating, taut cable are usually included on the right hand side of the equation of

motion. Specification of these force terms is discussed in Section 2 and Appendices D and E of this report.

The above equation is quite general since it includes both cable bending stiffness and finite amplitude vibrations, i.e. tension fluctuations. We now will examine the relative importance of these effects for marine cables. First, consider the ratio of the fluctuating tension to the equilibrium tension,

$$\frac{3}{2}\frac{EA}{T_0}\frac{Y^2}{L^2}n^2\pi^2.$$

It is reasonable to assume that $EA/T_0 = E/\sigma \approx 6 \times 10^3$ and $Y \approx D/2$ for actual cables that undergo flow-induced vibrations. Furthermore $L/D \approx 10^3$ is a conservative estimate, particularly for $n > 2$, and this ratio therefore becomes proportional to $n^2 \times 10^{-1}$. Using these estimates and the additional fact that the moment of inertia $I \approx (D/2)^4$, one then finds that the ratio of bending stiffness to equilibrium tension is on the order of $n^2 \times 10^{-2}$. The justification for treating the cable as an equivalent homogeneous string is thus apparent, as well as an ordering of the assumptions inherent in this approximation. The natural frequencies for a taut cable under the homogeneous linear string assumption are given by the simple classical relations

$$f_n = \frac{\omega_n}{2\pi} = \frac{n}{2L}\sqrt{\frac{T}{\rho A}}. \tag{A12}$$

Since the nonlinearity is small, a first approximation to the nonlinear tension fluctuation T_f can be obtained by substituting the linear string equation solution into the nonlinear expression, which yields the result

$$T_f = \frac{3\pi^2 Y^2 n^2 EA}{2L^2}\cos^2\frac{n\pi x}{L}\sin^2\omega t. \tag{A13}$$

The transverse motion of a particular cable now can be adequately predicted if the required cable properties are known. The virtual mass (the sum of the structural mass and added mass contributions) and damping are available, based upon recent experiments. The experimental characterization of the structural damping, the added mass, and the hydrodynamic damping is discussed in Appendix C. This discussion has been limited to taut cables; the dynamics of slack cables and the development of criteria for delineating the two regimes are discussed in Appendix B.

References

A1. G.S.S. Murthy and B.S. Ramakrishna, "Nonlinear Character of Resonance in Stretched Strings," Journal of the Acoustical Society of America, Vol. 38, pp. 461-471, 1965.

Appendix B

DYNAMICS OF SLACK MARINE CABLES

B.1. The Linear Theory for a Slack Cable. The vibrations of taut cables are described appropriately by the classical taut string equations. This approach neglects the cable's bending stiffness and finite amplitude vibration effects, but it is accurate to within 2-4 percent for many cables over a wide range of conditions (see Appendix A and references B1 and B2). As the tension is relaxed, a cable eventually assumes the configuration shown in Fig. B1. H is the horizontal component of tension at the supports and each vertical component V is equal to half of the total cable weight. The limiting sag-to-span ratio $s/l \rightarrow 0$ is accompanied by $H \approx T$ since the cable weight becomes a negligible fraction of the tension. At the other extreme, when s/l becomes large, V is comparable to or larger than H and the cable assumes a classical catenary shape. The natural vibrations of catenaries are known (B3) for $\frac{s}{l} > 1{:}10$, but until recently they could not be reconciled with the taut string theory as the ratio of sag to span vanished. This difficulty has been overcome by Irvine and Caughey (B4) as a result of including the extensional behavior of the cable in the theory.

A summary is given here of Irvine and Caughey's recent development and the results applicable to marine cables are discussed. The equilibrium shape of an *inextensible* cable is given by

$$y = \frac{mgl^2}{2H}\left[\frac{x}{l} - \left(\frac{x}{l}\right)^2\right] \tag{B1}$$

for $d/l < 1{:}8$ where $d = mgl^2/8H$ is the midspan sag. The length of this cable is $L \approx l\left[1 + +\frac{8}{3}\left(\frac{d}{l}\right)^2\right]$, so that if three of the quantities mg, H, d, l and L are known, the other two can be found. However, owing to stretch, the sag and length of a *real* cable are greater than the inextensible values while the horizontal component of tension of the stretched cable is less. If this new sag is s while the new horizontal component of tension is $(H - \Delta H)$, then equilibrium dictates that

$$\frac{s-d}{d} = \frac{H_*}{1-H_*} \tag{B2}$$

where $H_* = \Delta H/H$. Compatibility of the cable displacement requires, in addition, that

$$(1-H_*)^3 = \frac{\lambda^2}{24}(2H_* - H_*^2) \tag{B3}$$

where

$$\lambda^2 = \left(\frac{mgl}{H}\right)^2 \frac{l}{\left(\frac{HL_e}{EA}\right)} = 64\left(\frac{d}{l}\right)^2 \frac{l}{\left(\frac{HL_e}{EA}\right)} \tag{B4}$$

and

$$L_e = \int_0^l \left[1 + \left(\frac{dy}{dx}\right)^2\right]^{3/2} dx \approx l\left[1 + 8\left(\frac{d}{l}\right)^2\right] \tag{B5}$$

The quantity EA is the product of the elastic modulus and the cross-sectional area of the cable while L_e is the stretched cable length to the order of the linear theory approximation. According to Irvine and Caughey the dimensionless variable λ^2 is the fundamental parameter of the extensible cable because it accounts for both the elasticity and equilibrium geometry of the cable. In the subsequent notation H will be taken to mean the horizontal component of tension in the extensible profile, i.e. the measured tension.

In the study of natural vibrations, the equations of motion can be linearized about the equilibrium configuration and then the out-of-plane motions are decoupled to first order. The remaining in-plane modes then fall into two classes. In the first class there are no first-order tension fluctuations induced at the supports, whereas the second class induces first-order tension fluctuations. The two cases are characterized respectively by mode shape symmetry and antisymmetry about the cable midpoint. The antisymmetric motions of the sagging cable have the same frequency equation as the taut string, but the symmetric modes obey a different eigenvalue equation. This means that the classical equation for a taut cable is valid for $0 < s/l < 1{:}8$ if n is even, whereas the symmetric mode frequencies are given by

$$\tan\left(\frac{\beta l}{2}\right) = \frac{\beta l}{2} - \frac{4}{\lambda^2}\left(\frac{\beta l}{2}\right)^3 \tag{B6}$$

$$\beta = \left(\frac{m\omega^2}{H} \right)^{1/2} \tag{B7}$$

The result simplifies to the taut cable equation in the limit $s/l = 0$ when $mgl << H$ in equation (B4). In that case λ^2 approaches zero and equation (B6) reduces to

$$\lim_{s/l \to 0} \left[\tan \frac{\beta l}{2} \right] = -\infty \tag{B8}$$

and

$$(\beta l)_k = (2k - 1)\pi, \quad k = 1, 2, 3... \tag{B9}$$

or

$$f_n = \frac{n}{2l} \sqrt{\frac{T}{m}}, \quad n \text{ odd.} \tag{B10}$$

A graphical solution to equation (B9) is presented in Fig. B2 for several values of the parameter λ^2. The arrows indicate the values of $\frac{\beta l}{2}$ which correspond to the natural frequencies of a taut string. For small λ^2 the symmetric mode frequencies approach those of a taut string. However, as λ^2 increases the first symmetric mode frequency increases toward the first antisymmetric frequency. They coincide for $\lambda^2 = 4\pi^2$ and thereafter the first symmetric mode frequency is greater than the first antisymmetric mode frequency. At still larger values of λ^2 these frequency crossovers occur at the higher symmetric modes.

As an example consider $\lambda^2 = 36\pi^2$. The antisymmetric mode values of $\frac{\beta l}{2}$ are given by $\frac{n\pi}{2}$, $n = 2,4,6$, etc. as before while the first four symmetric mode solutions are indicated by the encircled intersections in Fig. B2. The lowest two symmetric mode frequencies have crossed over and lie above the lowest two antisymmetric frequencies. The frequencies of the third symmetric and antisymmetric modes are equal (crossover is occuring) while the fourth symmetric mode frequency is quite close to the $n = 7$ frequency of a string. For the modes higher than $n = 7$ the natural frequencies are essentially those of the taut string. The catenary effects progress into the higher modes as λ^2 increases, but for finite λ^2 some unaffected modes remain. Returning to the first symmetric mode frequency of the

example, there is little difference between $\lambda^2 = 36\pi^2$ and $\lambda^2 = \infty$ so that the first mode is nearly inextensible. For $\lambda^2 = \infty$, equation (B6) reduces to

$$\tan\left(\frac{\beta l}{2}\right) = \left(\frac{\beta l}{2}\right) \tag{B11}$$

which is also plotted in Fig. B2. With this frequency equation the symmetric natural frequencies are again well ordered and alternate with antisymmetric frequencies, but there is a shift of between 0.93π and π in these symmetric mode frequencies with respect to the taut string symmetric mode frequencies.

The modes shapes are affected by the frequency crossover in a very interesting manner. A symmetric mode must possess an even number of nodes. The mode shape acquires two additional nodes in crossing over, thus altering its form while preserving symmetry. The transition is smooth as shown in Fig. B3 which is adapted from a related numerical study by West, Geschwindner and Suhoski (B5). A dashed line which corresponds to the example $\lambda^2 = 36\pi^2$ is included in Fig. B3a.

Some recent NRL experiments (B2) demonstrated this behavior as shown in Fig. B4. To the right of the crossover the mode shapes were identifiable with the $n = 1$ (0) and $n = 2$ (□) mode shapes of a taut cable, although the natural frequencies of the $n = 1$ curve deviate from those of a taut string. To the left of the crossover the $n = 2$ mode was essentially unchanged while the mode shape for the other curve (●) acquired two additional nodes and thus resembled an $n = 3$ mode of a taut cable. The observed modal transitions were of the form predicted by Irvine and Caughey and are indicated in Fig. B3(b). According to the theory the first crossover occurs at $\lambda^2 = 4\pi^2$ and this provides a means for comparison with the data. Since the product EA is not a simple material constant for cables, particularly at low tensions, a range of values for EA was found from curves of elongation versus tension measured at NRL. The crossover range computed in this way is included in Fig. B4 and is in good agreement with the experimental observations. The in-water tests with the same cable afforded another opportunity for comparison. The same range of EA was employed, but the linear weight was adjusted to reflect the buoyancy. The result is shown in Fig. B5 and again there is good agreement with the theory.

B.2 The Onset of Catenary Effects. An expression for the "critical" tension corresponding to the onset of catenary behavior can be obtained from equation (B4). The result is

$$H_{crit} = \left(\frac{mg}{\lambda_{crit}}\right)^{2/3} \left(\frac{EA}{L_e}\right)^{1/3} l. \tag{B12}$$

By requiring the cable frequency to be within 5 percent of the taut string, an approximation consistent with the accuracy of the string equation, one obtains

$$\lambda^2_{crit} = 1.26. \tag{B13}$$

Since $d \approx s$ for typical cables when λ^2 is small, equation (B5) becomes

$$L_e = l\,(1 + 8\,(s/l)^2) < 9/8\,l. \tag{B14}$$

The onset of slack effect occurs near the limit of $s/l \to 0$, so that a slightly conservative estimate is established by putting $L_e \approx l$ to obtain

$$H_{crit} = 0.93(W^2EA)^{1/3}, \tag{B15}$$

where $W = mgl$ is the *total* weight of the cable to the accuracy of the linear theory. The corresponding critical sag is

$$s_{crit} = 0.134\left(\frac{W}{EA}\right)^{1/3} l. \tag{B16}$$

For the Double Armor Steel (DAS) cable, equation (B15) yields

$$H_{crit} = 200 - 300 \text{ lbs } (890 - 1340 \text{ N}) \text{ in air}$$

and

$$H_{crit} = 167 - 254 \text{ lbs } (743 - 1130 \text{ N}) \text{ in water.}$$

When they are compared to the data in Figs. B4 and B5, these tensions correspond well to the regions where the cables begin to deviate from a taut string behavior, i.e. where $f \sim (T)^{1/2}$. It should be emphasized that this criterion applies only to the initiation of catenary effects in only the symmetric modes, since the antisymmetric modes are unaffected for $s/l < 1{:}8$ and $H > W$. Furthermore, at $H = H_{crit}$ the only affected mode will be the $n = 1$ mode. If one is interested in the onset of slack effects at the higher symmetric modes, then the expression becomes

$$H_{crit} = \left(\frac{W^2EA}{\lambda_n^2}\right)^{1/3} \tag{B17a}$$

where

$$\lambda_n^2 = \frac{4\alpha^3}{\alpha - \tan\alpha}, \quad \alpha = 0.525\, n\pi, \quad n = 1, 3, 5, \text{ etc.} \tag{B17b}$$

Additional experimental results are discussed in a recent paper which deals with marine cable applications (B6).

B.3. The Inclined Slack Cable. The linear theory just described has proven to be a valuable tool in the analysis of marine cable vibrations. A shortcoming of the original analysis is a restriction to horizontal cables or, more precisely, to cables with supports at the same elevation. The simplest way to extend the theory to cables with inclined chords is to view the cable in a coordinate system inclined with the cable (B7). In order to retain symmetry about the cable midpoint, an essential feature of the linear analysis, one must ignore the effect of the chordwise component of gravity. The problem then reduces to the previous analysis except that the weight per unit length is given by $w = mg \cos\theta$ where θ is the chord inclination angle from the horizontal.

According to the linear theory, the horizontal (or chordwise) component of tension H is constant along the cable,

$$H = mg \cos\theta\, l^2/8s. \tag{B18}$$

However, the chordwise component of gravity produces a change in H from one end to the other of an inclined cable by an increment ΔH given by

$$\Delta H = mg\, l \sin\theta. \tag{B19}$$

Thus the modified linear analysis for inclined slack cables is subject to

$$\epsilon = \frac{\Delta H}{H} \ll 1$$

or

$$\epsilon = 8\,(s/l)\tan\theta \ll 1. \tag{B20}$$

This condition places rather stringent limits on the sag-to-span ratio as the chord inclination angle steepens.

Experiments were conducted at NRL to examine the natural vibration of inclined slack cables. Essentially, the earlier Double Armor Steel (DAS) cable experiments were repeated in the DTNSRDC

test frame except that the frame could be rotated to angles up to $\theta = 34°$ from the horizontal. Three angles, $\theta = 0°$, 20° and 34°, were selected for the experiments. An important feature of the inclined cable analysis described above is that all frequencies should collapse onto a single curve if the span and sag are measured in the appropriate inclined coordinates (B7). This was indeed the case in the present experiments as shown in Fig. B6 and this finding justifies the simplified approach. If these same frequencies are plotted against the tension H, then a separate curve for each inclination angle is obtained as indicated by equation (B18).

Although the ranges of the inclination angles and the sag-to-span ratios are somewhat restricted, one can generalize the present results to larger angles by using the quantity ϵ. In the tests conducted at NRL ϵ was as large as 0.48, which includes substantially greater values of s/l and θ than are implied by equation (B18). For example, $\epsilon \leqslant 0.48$ implies that the linear analysis is adequate for sag-to-span ratios at least as large as 0.06 and 0.035 at $\theta = 45°$ and $\theta = 60°$ respectively.

B.4. The Slack Cable Computer Code. The finite element slack cable code which was originally written by Henghold, Russell and Morgan (B8) has been adapted for marine cable studies. The resulting FORTRAN source program, called SLAK, is available to interested users. The remainder of this appendix is devoted to a further discussion of the slack cable problem and to brief descriptions of the method, code, the input and some typical results. Extensive comparisons between numerical, theoretical, and experimental results for inclined slack cables are contained in the final section of this appendix.

A sketch of an inclined slack cable is presented in Fig. B7 along with the appropriate nomenclature. The numerical problem is defined by the locations of the two ends of the cable (left end always at $x = y = z = 0$), by the unstretched initial length of the cable L, by the physical properties of the cable grouped together as AE/mgL, and possibly by the number and location of (any) applied loads and attached discrete masses. The loads and masses must be concentrated at the nodes of the finite element model. Important derived parameters are the cable span l (i.e. chord length) and the cable inclination angle θ (i.e. chord inclination). The principal results are the equilibrium shape of the cable,

often characterized by the maximum or midspan sag s, the support reaction forces, the natural frequencies, and the mode shapes with respect to the equilibrium position. It should be noted that the SLAK code is three-dimensional and permits applied loads in the z-direction and computes the out-of-plane or sway modes of the cable. Additional information concerning the code itself, the numerical method, and the required input data is available from NRL.

B.5. Inclined Slack Cable Comparisons. This section compares numerical, theoretical, and experimental results for inclined slack cables. The purposes of the comparisons are twofold. First, an attempt is made to account for some discrepancies between the experimental data and the theoretical predictions at moderate sag-to-span ratios. Second, and more important, the extension of the linear theory to inclined slack cables (B7) is tested against the finite element code calculations so that engineering limits for the simple extension can be determined. The slack cable problem is defined in the preceding pages where descriptions of the theory and the finite element code are given. This section deals only with comparisons and with an analysis of the results.

The discrepancy just mentioned is illustrated in Fig. B6. For sag-to-span rations s/l greater than 0.02 the experimental data no longer follow the theoretical prediction. Earlier attempts to identify the mode shape(s) in these instances were frustrated by the complex construction of the DAS cable specimen near its ends. It is in these segments of the cable that additional loops in the mode shape are known to form during and after the "modal cross-over". The complex construction can also directly influence the dynamics by abrupt changes in the mass per unit length, by abrupt changes in the cable stiffness and by a number of lesser effects. Neither the theory nor the finite-element code provides for cable stiffness and it was felt that this might be the largest source of error because of the relatively large amount of local curvature required by the forming loops as compared to the significant stiffness of the cable segment and of its aluminum terminations.

An important feature of the simplified inclined cable analysis is that all frequencies should collapse onto a single curve if the span and the sag are measured in the appropriate inclined coordinates

and if the cable parameter AE/mgL is adjusted to reflect the change in the body force. This was the case in the NRL experiments shown in Fig. B6 and this finding justified the simplified approach for that range of conditions. In order to search for the limits to the theoretical approach implied by equation (B20) a number of numerical cases were run for different sag-to-span ratios at several inclination angles up to $\theta = 75$ degrees from the horizontal. The results are plotted in Fig. B8 in the appropriate coordinates, but with the numerical code parameter AE/mgl held constant. The frequencies collapse onto the proper curves everywhere except at crossover. This behavior is correct since λ^2 (or AE/mgl) also must be adjusted to reflect the cable inclination. Several runs were made which verified that the use of $AE/mgl \cos\theta$ will collapse the crossover data up to inclination angles of $\theta = 75°$. The point to be made here is that the limitations imposed by equation (B20) are far less stringent than they appear and, within a numerical accuracy of a few percent, the horizontal cable limitation of $s/l \leqslant 1/8$ holds equally well for inclination angles up to $\theta = 75°$. This range of angles includes virtually all structural applications and most mooring cases as well.

References

B1. S.R. Heller and B.S. Chung, "On the Transverse Vibrations of Wire Rope," Catholic University Report 72-7, 1972.

B2. S.E. Ramberg and O.M. Griffin, "Some Transverse Vibration Properties of Wire Rope with Application to Flow-Induced Cable Vibrations," Naval Research Laboratory Report 7821, 1974.

B3. D.S. Saxon and A.E. Cahn, "Modes of Vibration of a Suspended Cable," Quarterly Journal of Mechanics and Applied Mathematics, Vol. 6, pp. 273-285, 1953.

B4. H.M. Irvine and T.K. Caughey, "The Linear Theory of Free Vibrations of a Suspended Cable," Proceedings of the Royal Society of London, Series A, Vol. 341, pp. 299-315, 1974; See also California Institute of Technology Dynamics Lab Report DYNL-108, 1974.

B5. H.H. West, L.F. Geschwinder and J.E. Suhoski, "Natural Vibrations of Suspension Cables," Proceedings of the ASCE, Journal of the Structural Division, Vol. 101, pp. 2277-2291, 1975.

B6. S.E. Ramberg and O.M. Griffin, "Free Vibrations of Taut and Slack Marine Cables," Proceedings of the ASCE, Journal of the Structural Division, Vol. 103, pp. 2079-2092, 1977.

B7. H.M. Irvine, "Free Vibrations of Inclined Cables," Proceedings of the ASCE, Journal of the Structural Division, Vol. 104, pp. 343-347, 1978.

B8. W.M. Henghold, J.J. Russell and J.D. Morgan, "Free Vibrations of a Cable in Three Dimensions, Proceedings of the ASCE, Journal of the Structural Division, Vol. 103, pp. 1127-1136, 1977.

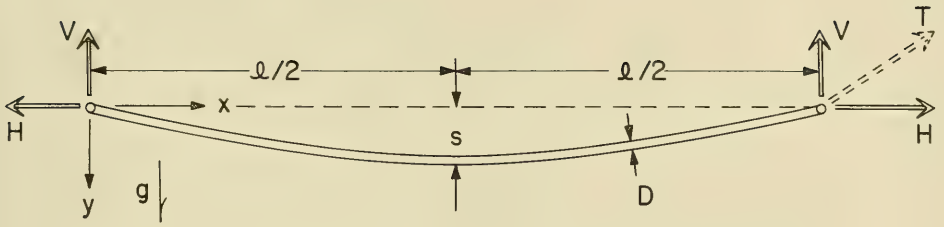

Figure B1 The geometry and nomenclature for a slack cable of length L and mass per unit length m.

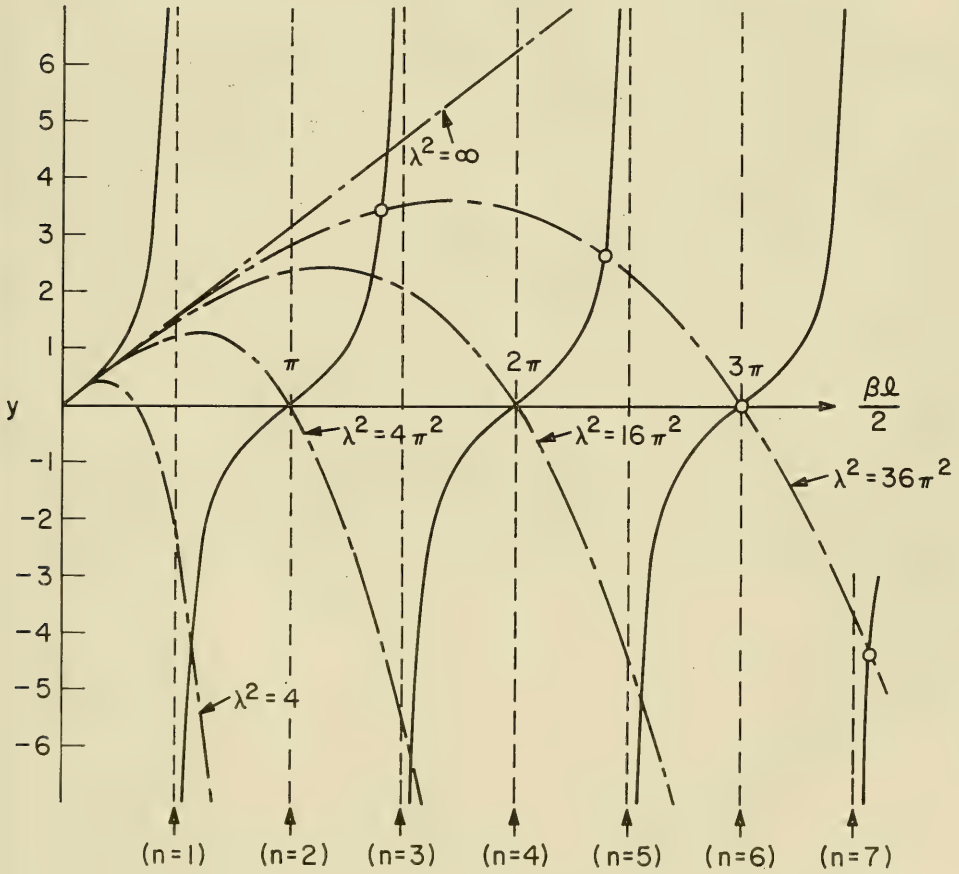

Figure B2 Graphical solutions to equation (B9) for the lowest symmetric-mode natural frequencies of a flat-sag cable. The effects of cable sag and extension are included in the parameter λ^2 (see equation (B4)). For $\lambda^2 = \infty$ the cable is inextensible, and for $\lambda^2 = 0$ the cable is taut.

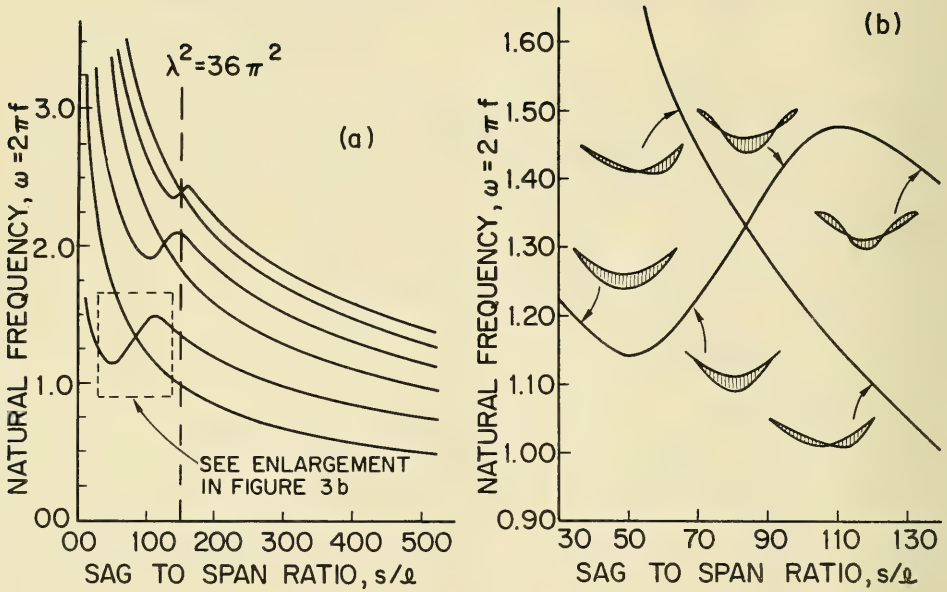

Figure B3 Two figures adapted from reference B5 showing (a) the natural frequencies versus the variation in sag including modal crossovers, and (b) an indication of the mode shape transitions during a crossover of the lowest modes of Figure B3(a)

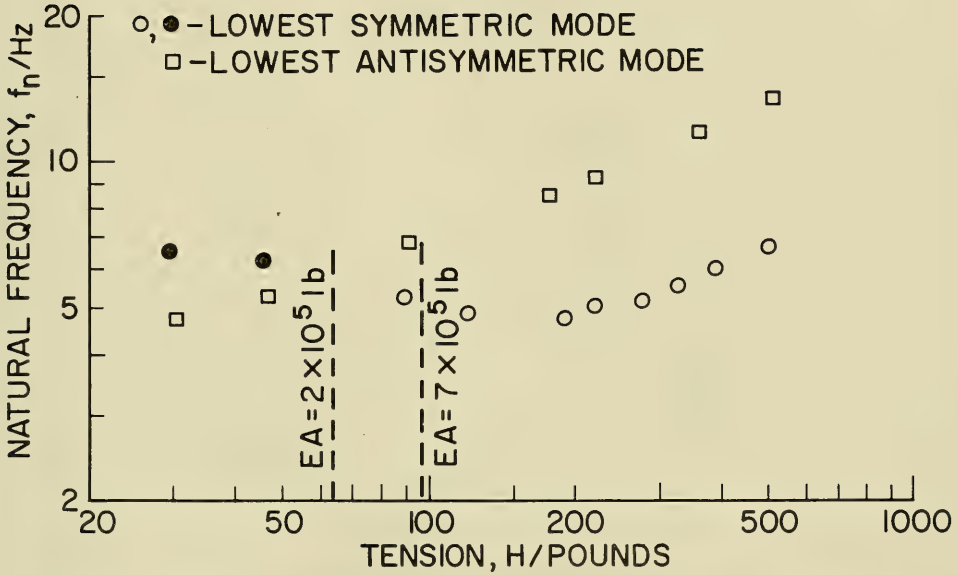

Figure B4 The measured natural frequencies f_A of a Double Armor Steel cable in air. Cable diameter = 5/8 in. (1.59 cm). (1 lb = 4.45 N)

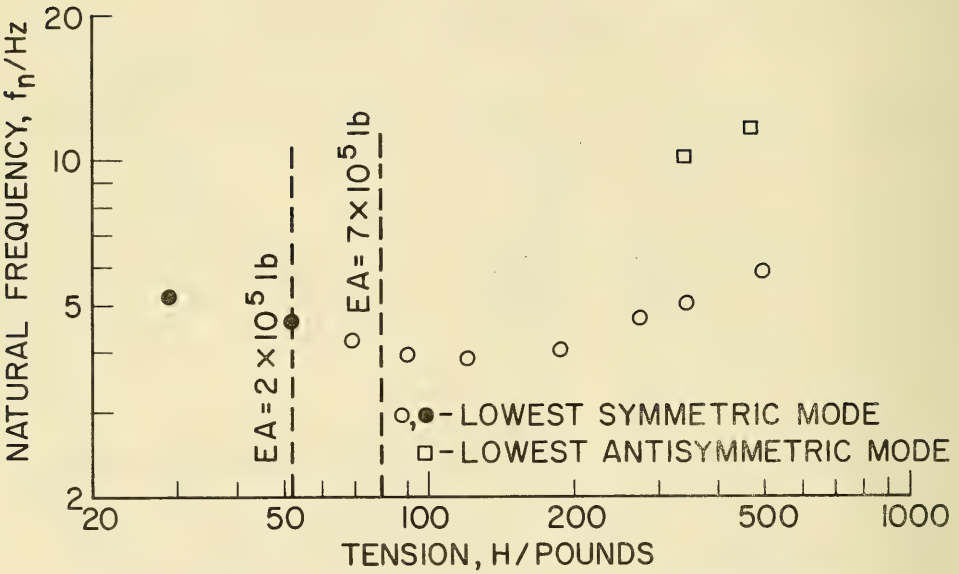

Figure B5 The measured natural frequencies f_w of a Double Armor Steel cable in water. (1 lb = 4.45 N)

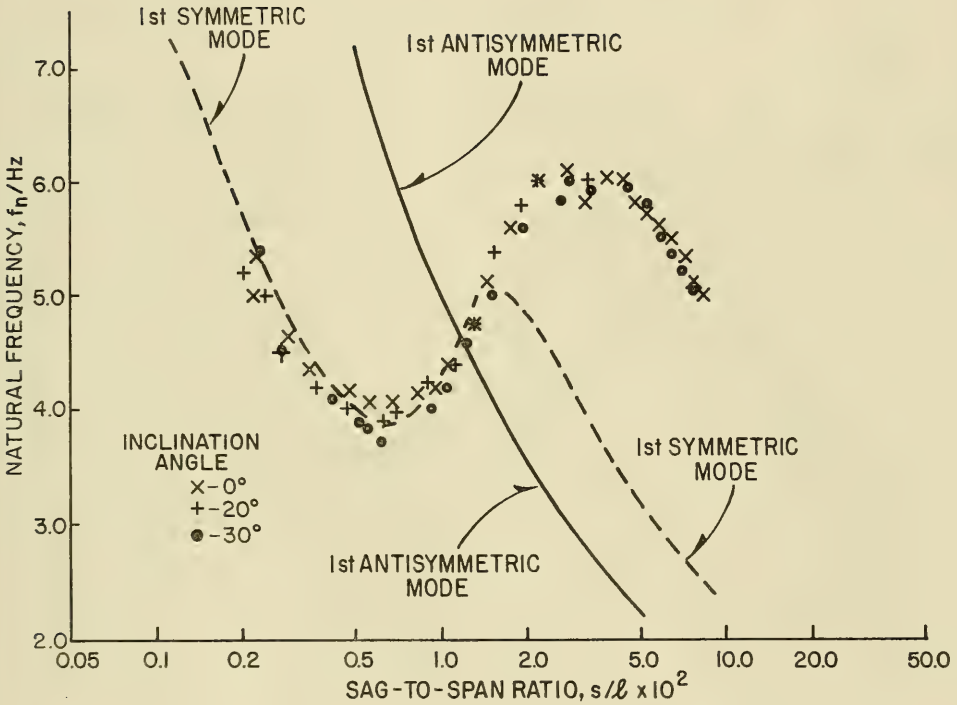

Figure B6 Measured and calculated natural frequencies for an inclined, slack Double Armor Steel (DAS) cable. Cable diameter $D = 1.55$ cm (0.61 in.).

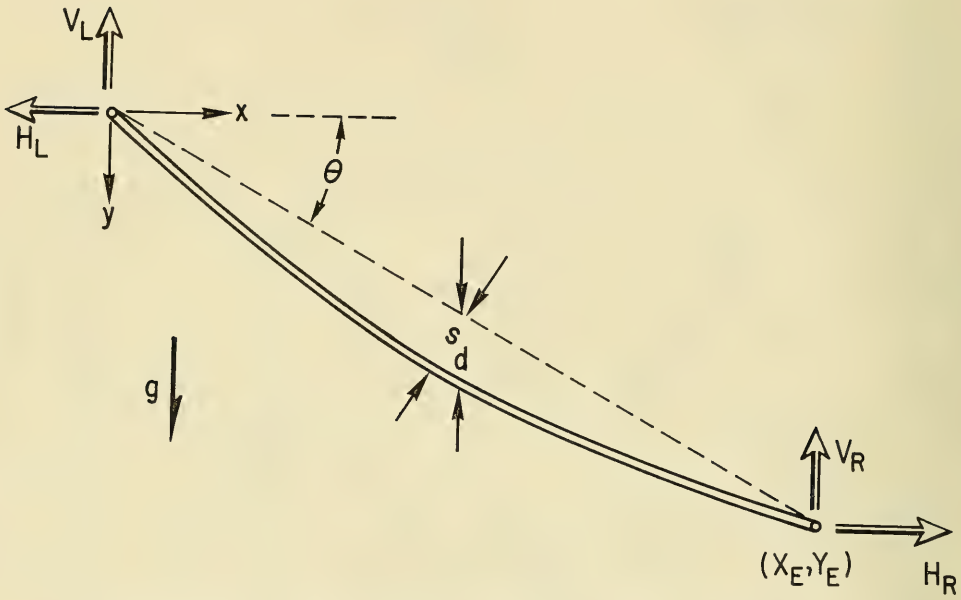

Figure B7 The geometry and nomenclature for an inclined slack cable of length L and mass per unit length m.

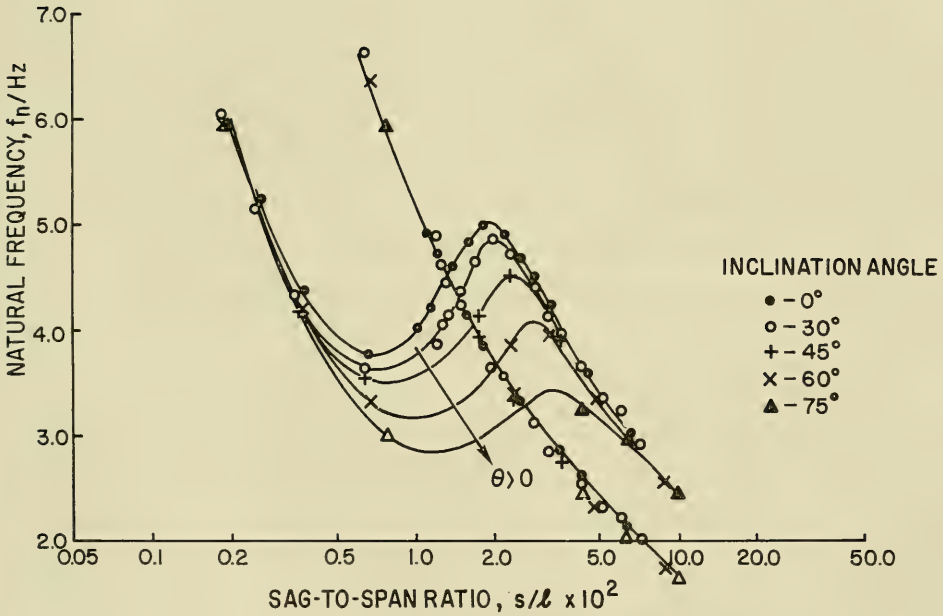

Figure B8 Numerical results for the lowest two in-plane modes of an inclined, slack cable.

Appendix C

ADDED MASS AND DAMPING COEFFICIENTS

C.1 Structural Damping of Marine Cables. In order to quantify the coefficients in the equation for the resonant vibrations of marine cables, both the *structural* and the *hydrodynamic* damping coefficients must be specified. These damping coefficients have been measured for a variety of marine cables as part of the NAVFAC research program in cable dynamics. Some typical, but limited, measurements of the structural damping, from experiments conducted at NRL, are now discussed. Free vibration experiments with the DTNSRDC test cables (C1) and the CEL-supplied small diameter cables were conducted and the results are summarized here. The characteristics of the DTNSRDC cables are listed in Table C1.

The measured in-air natural frequencies for two representative test cables are plotted in Figs. C1 and C2. In the DTNSRDC test apparatus that was employed in the experiments discussed here (see Fig. 3.6), the cable span was maintained while the length was varied to accommodate changes in the tension. The differences between the various test spans and cable lengths were small, but they did account for some of the apparent discrepancies between the two sets of experiments. Another difference between the two sets of experiments was due to changes in the rigidity of the cable supports. The stiffness of the DTNSRDC cable mounting struts (see reference C1 for a detailed description of the test apparatus), as seen by the cable, depends on the relative orientation of the two struts. Strut motions were quite evident during the tests when the DTNSRDC test apparatus was configured for the cable axis normal to the towing direction. The stiffness of the struts was increased by rotating them until their longest dimension was nearly aligned with the cable axis. As indicated in the accompanying figures, an increase in the support rigidity raised the measured cable natural frequency at a given tension. This effect diminishes with increasing tension as the vibration-induced tension fluctuations

drop to second order from the larger first order tension fluctuations that are characteristic of slack cables. The influence of strut rigidity upon the measured in-air (structural) damping is discussed in further detail later in this Appendix.

The measured in-air damping is generally referred to as the structural damping because it is assumed that external energy losses to the air or supports are negligible when compared to the cable's internal losses. The validity of this assumption depends upon the magnitude of the measured damping and upon the compliance of the cable supports. Estimates of the fluid losses in air can be used to check that part of the assumption, but losses to the supports are difficult to determine or even to estimate. In the present experiments, test runs with the same cable for two strut rigidities made it possible to identify changes in the damping due to the very different support conditions. This task was complicated by the nonlinear behavior of the in-air damping, and to discount this nonlinearity the log decrements for the Uniline and DAS cables are presented in Figs. C3 and C4 for approximately the same initial amplitude (0.1″ or 2.5 mm). In both cases the data generally correspond to taut cable conditions, although at the lowest tensions the DAS cable behavior is in the range of slack cable effects (see Appendix B). From the results in Fig. C3 it appears that the Uniline cable is not influenced by variations in the rigidity of the struts. The DAS cable behavior is significantly dependent on the rigidity and, as shown in Fig. C4, the measured damping is lower when the struts are more flexible. The relative importance of strut rigidity in each case is consistent with the natural frequency measurements in Figs. C1 and C2.

Any influence of the initial amplitude could not be detected in one or even several cycles of the vibration decay. The procedure adopted was to take 150 to 450 consecutive vibration cycles and to compute the log decrement of the damping over various segments of the record. The lengths of the record and therefore the lengths of the segments were dictated by the resolution of the measuring system and the rate of the vibration decay.

The structural log decrements obtained in this manner appeared to be a simple linear function of cable amplitude, but it is quite possible that this linear behavior is due to the limited range of

displacement amplitudes tested. Also, the DAS and Uniline cables were very different in terms of their response characteristics. For example, the log decrements for the Uniline cable decreased by about 0.001 as the amplitude dropped from 0.1 inches to 0.02 inches; this was independent of the tension. On the other hand, the change in structural damping of the DAS cable depended on the tension. For tensions less than 200 pounds the log decrement increased by as much as 70-90 percent for amplitudes between 0.02 and 0.1 in., whereas the increase was 30 percent or less for tensions above 200 pounds. Some of the differences are undoubtedly due to the onset of slack cable conditions, but it should be noted that the DAS cable damping increases were always dependent upon the tension even when the cable was essentially taut. This discussion pertains only to the taut or nearly taut cases for which the mounting struts were perpendicular to the cable axis; a similar analysis for other strut orientations and/or lower tensions was not attempted because of the uncertainties involved.

This discussion has shown the difficulties encountered in attempting to measure the structural damping of marine cables. One inescapable conclusion, however, is that the structural damping of cables is small as shown here, in Fig. 3.10 and in reference C2. This small structural damping places most cable strumming conditions well toward the left-hand portion of Fig. 2.2 where the reduced damping is very small and *hydrodynamic forces predominate in controlling the strumming response.*

C.2 Hydrodynamic Added Mass and Damping. The added mass effect due to the unsteady relative motion between the surrounding fluid and the cable is customarily treated as being proportional, by the added mass coefficient C_{am}, to the mass of the fluid displaced by the body. Therefore the ratio of virtual mass density in water to the body's mass density in air is given by

$$\frac{\rho_W}{\rho_A} = 1 + C_{am}/S \tag{C1}$$

in which S is the specific gravity of the cable. It is assumed that the fluid loading in air is negligible. In addition, the ratio of the in-air resonant frequency, f_A, to the in-water resonant frequency, f_W, at the same load and mode shape is given by (using the taut string approximation, as in Appendix A)

$$\frac{f_A}{f_W} = \left[\frac{\rho_W}{\rho_A}\right]^{1/2} \tag{C2}$$

The added mass coefficient is determined from experimental measurements by means of equations (C1) and (C2) which combine to give

$$C_{am} = S\left[\left(\frac{f_A}{f_W}\right)^2 - 1\right]. \tag{C3}$$

Since f_A and f_W are usually close, particularly at low frequencies, a small error (1 or 2%) in one or both often results in relatively large variations in C_{am}(~10-40%). For this reason it is helpful to also consider the ratio of the virtual and actual masses which, according to equation (C2), is the square of the frequency ratio $\frac{f_A}{f_W}$. Most of the conclusions in this section related to the added mass effect for marine cables are based on the measured values of $\frac{f_A}{f_W}$.

The added mass coefficient C_{am} was determined from equation (C3) for a variety of marine cable materials and constructions. The results are plotted against the "vibration Reynolds number," $\mathrm{Re}_v = fD^2/2\nu$ in Fig. C5 and the legend for the data points is given in Table C2. The cables were taut for all of the conditions tested and discussed here. The dashed line in Fig. C5 represents the classical added mass prediction developed by Stokes (see Rosenhead, reference C3). This predicted value of C_{am} is given by the equation

$$C_{am} = 1 + 2\sqrt{\frac{2}{\mathrm{Re}_v}}. \tag{C4}$$

Table C1
Marine Cable Model Physical Characteristics
DTNSRDC Towing Tank Experiments (C1,C2)

Cable Model/Type	Nominal Diameter		Nominal Length		Weight In Air		Weight In water		Virtual Mass	
	(ft)	(cm)	(ft)	(m)	(lbs/ft)	(N/m)	(lbs/ft)	(N/m)	(slugs/ft)	(kg/m)
Double Armored Steel (DAS)	0.051	1.55	14.38	4.38	0.520	7.59	0.391	5.71	0.0202	0.967
Uniline	0.050	1.52	14.27	4.35	0.190	2.77	0.069	1.01	0.00967	0.463
Small Diameter (Piano wire)	0.0058	0.177	14.25	4.34	0.0065	0.095	0.0048	0.070	0.00025	0.012

The measured and predicted values of C_{am} show considerable deviation at small Re_v, but reasonable agreement is exhibited at $Re_v = 2000$ and above. However, the predicted curve is valid only as a guide since most of the simplifying assumptions under which it was derived are not applicable to large amplitude vibrations of marine cables.

The hydrodynamic damping is considered in the form

$$k_s = \frac{\pi}{2}(S + C_{am})\delta = \frac{\pi}{2}\left(\frac{f_A}{f_W}\right)^2 \delta. \tag{C5}$$

The values of k_s measured by vibrating the cables listed in Table C2 in still water are plotted in Fig. C6. The parameter k_s usually termed the reduced damping, commonly appears in the study of flow-induced oscillations of cables and structures (C2) and is related to the linear damping coefficient c by

$$c = \rho D^2 f k_s. \tag{C6}$$

In either form the total damping is the sum of the structural and hydrodynamic damping contributions. For taut cable conditions, however, the structural contribution is very small and the results in Fig. C6 are essentially equal to the fluid contribution to the total damping. The same dependence of the added mass and fluid damping on the vibration Reynolds number was obtained by Chen, Wambsganss and Jendrejczyk (C4) and by Skop, Ramberg and Ferer (C5) during experiments conducted with vibrating cylinders in water.

Table C2
Cable Added Mass and Damping;
Legend for the Data in Figures C5 and C6

Cable type and specifications	Fig. C5	Fig. C6
3/32 inch (2.4 mm) steel wire cable, three modes:	□ Δ ▲	O, ◐, ●
3/32 inch (2.4 mm) hydrophone cable		Δ
1/4 inch (6.4 mm) steel wire, two modes:	■	□ ◨
3/8 inch (9.5 mm) jacketed kevlar fiber:	O	X
7/16 inch (11.1 mm) polyester fiber:		+
0.6 inch (15.5 mm) Double Armor Steel cable:		
0.6 inch (15.5 mm) Uniline cable:	▷	▷
0.6 inch (15.5 mm) Seacon cable:	◁	◁

The hydrodynamic contributions to changes in the natural frequency (added mass) and in the damping also can be determined for slack cables. The method is approximate, but it demonstrates the applicability of the data in Figs. C5 and C6 to slack cable vibrations in water. Computations were carried out for the Double Armor Steel (DAS) cable because a range of EA was available only for that particular cable construction. A single value of EA was chosen for the computations despite the likelihood that it was tension-dependent. This value of EA was selected to give a good representation of the measured frequencies in air and of the observed modal crossover (see Appendix B) in particular.

The natural frequencies were predicted from equations (B4) and (B6) for two equilibrium positions corresponding to the in-air and in-water tests. Thus, the difference between the predictions shown by the dashed lines in Fig. C7 represents a change in the natural frequency due to a reduction in the linear weight of the cable. Subtracting this buoyancy contribution from the total difference between the frequency measurements yields the added mass effect of the water. From the computations, this correction disappears, as it should, when the cable becomes taut ($\lambda^2 \rightarrow 0$). The predictions are about 5 percent below the in-air measurements at large tensions, most likely due to the neglected bending stiffness of the cable. At the lowest tensions there is a large discrepancy between the predictions and the measured points that raised some doubt as to the validity of the measurements represented by those data points; it was later determined that this anomaly was probably a result of the particular cable configuration (see Appendix B, Section B5). The added mass coefficients nevertheless were computed from the data and with the exception of the results obtained at the lowest two tensions, the coefficients in Table C3 are comparable to the added mass results in Fig. C5.

Estimates of the fluid damping involved additional approximations but good results were obtained. After calculating the approximate in-air and in-water values of δ, the fluid damping contribution was estimated by taking the difference between the log decrements measured in the two media at the same sag-to-span (s/l) ratios. In this way the significant contribution of the structural damping for slack cables was discounted from the measured total damping in water, and the fluid damping was compared

to earlier measurements for taut cables and cylinders. These results and their corresponding values of k_s are listed in Table C3, and they agree quite well with the measurements shown in Fig. C6.

Table C3
Flat-Sag Cable Results for Added Mass and Damping
Double Armor Steel (DAS) Cable

Natural frequency in water, f_n/Hz	Added mass coefficient, C_{am}	Hydrodynamic decrement, δ	Vibration Reynolds number, Re_v	Reduced fluid damping, k_s
5.2 (29)*	2.48	0.21	1920	2.16
4.65 (52)	2.40	0.07	1720	0.71
4.24 (69)	1.14	0.08	1570	0.73
3.93 (90)	1.06	0.07	1450	0.56
3.83 (100)	1.06	0.09	1420	0.72
4.02 (187)	1.10	0.05	1485	0.41

*Tension in pounds (1 pound = 4.45 Newtons)

Sarpkaya (C6) discusses an alternate method for calculating the added mass and damping coefficients from force coefficients measured in periodic flows of water over stationary cylinders. However, care should be taken in interpreting these force coefficients because the added mass coefficient C_{am} is not equal to the inertia coefficient C_{mh} or C_{ml} as measured in a periodic flow of water. There is an additional pressure gradient generated by the acceleration of the fluid in the latter case which produces the so-called Froude-Krylov force. Under potential flow or ideal fluid conditions C_{mh} or C_{ml} is unity plus C_{am}.

References

C1. J.H. Pattison, "Measurement Technique to Obtain Strumming Characteristics of Model Mooring Cables in Uniform Currents," David W. Taylor Naval Ship Research and Development Center Report SPD 766-01, April 1977.

C2. O.M. Griffin, J.H. Pattison, R.A. Skop, S.E. Ramberg and D.J. Meggitt, "Vortex Excited Vibrations of Marine Cables," Proceedings of ASCE, Journal of the Waterways, Port, Coastal and Ocean Division, Vol. 106, No. WW2, pp. 183-204, 1980.

C3. L. Rosenhead, *Laminar Boundary Layers,* Oxford University Press: London, 1966, pp. 390-393.

C4. S.S. Chen, M.W. Wambsganss and J.A. Jendrejczyk, "Added Mass and Damping of a Vibrating Rod in Confined Viscous Fluids," Transactions of ASME, Journal of Applied Mechanics, Vol. 43, pp. 325-329, 1976.

C5. R.A. Skop, S.E. Ramberg and K.M. Ferer, "Added Mass and Damping Forces on Circular Cylinders," Naval Research Laboratory Report 7970, March 1976; see also ASME Petroleum Division Paper 76-Pet-3.

C6. T. Sarpkaya, "Vortex-Induced Oscillations, A Selective Review," Transactions of ASME, Journal of Applied Mechanics, Vol. 46, 241-258, 1979.

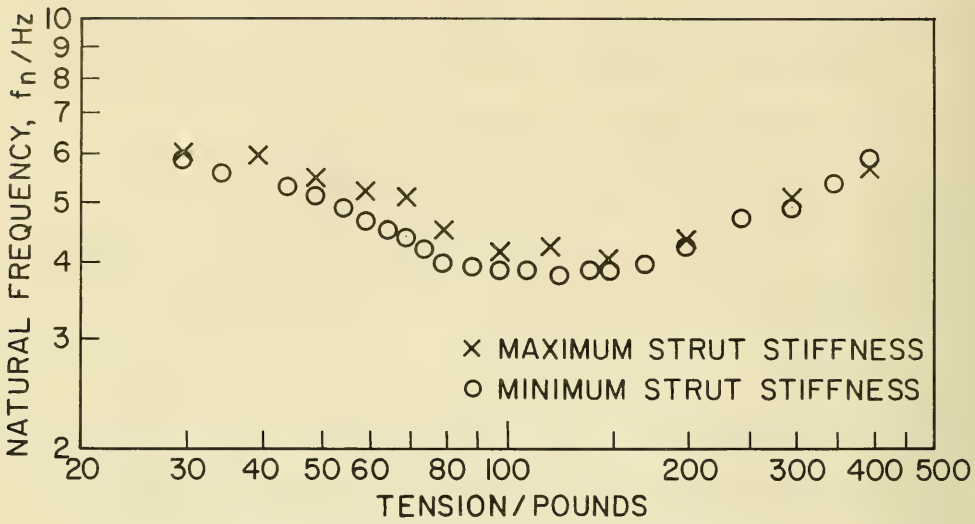

Figure C1 Measured natural frequencies for the Double-Armored Steel (DAS) cable (see Table C1) mounted in the DTNSRDC test apparatus.

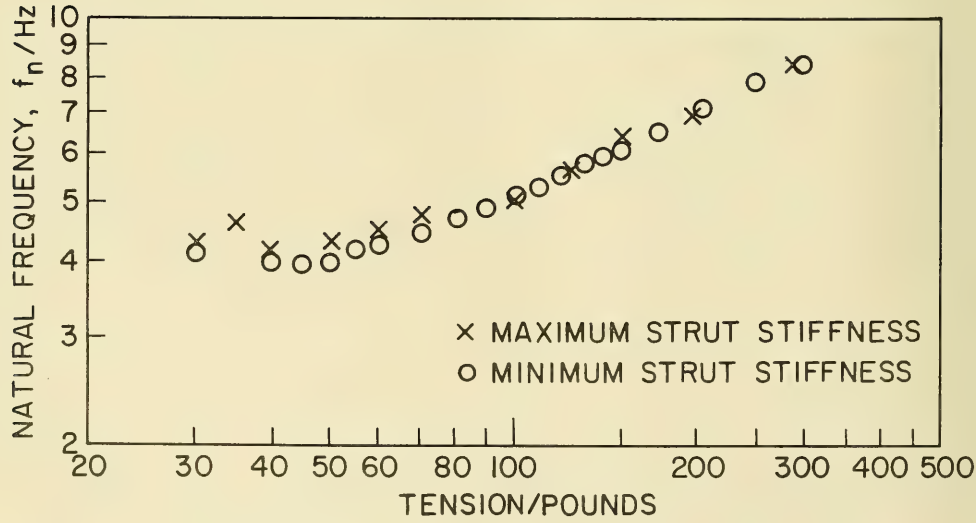

Figure C2 Measured natural frequencies for the Uniline cable (see Table C1) mounted in the DTNSRDC test apparatus.

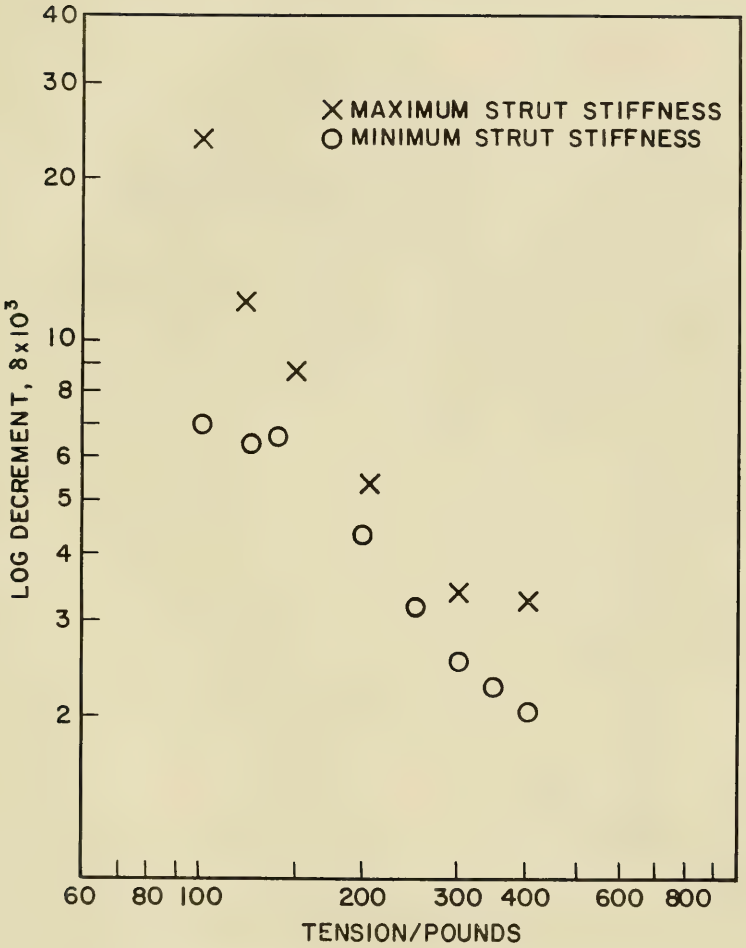

Figure C3 The measured in-air (structural) log decrements δ of the Uniline cable in the DTNSRDC test apparatus. Initial amplitudes are all approximately 0.1 in. (2.5 mm).

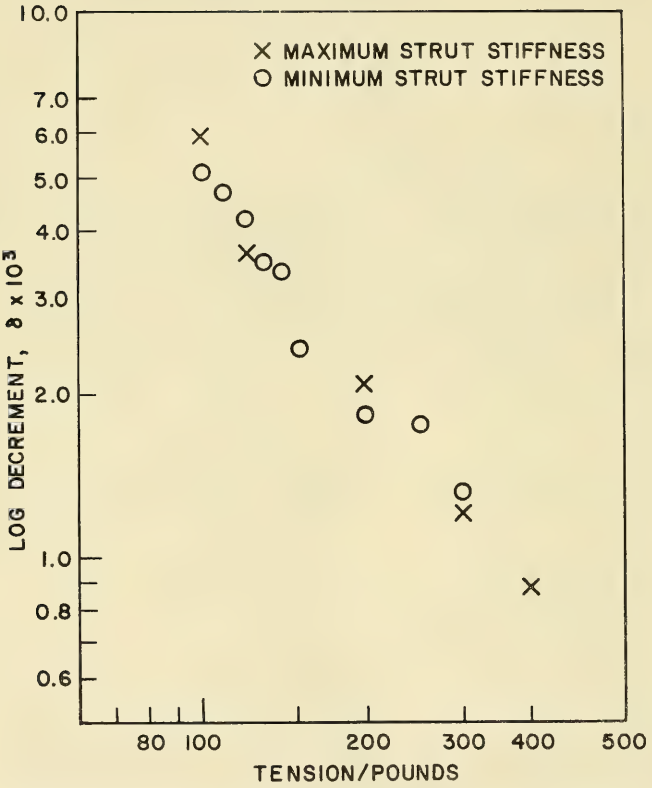

Figure C4 The measured in-air (structural) log decrements δ of the DAS cable in the DTNSRDC test apparatus. Initial amplitudes are all approximately 0.1 in. (2.5mm).

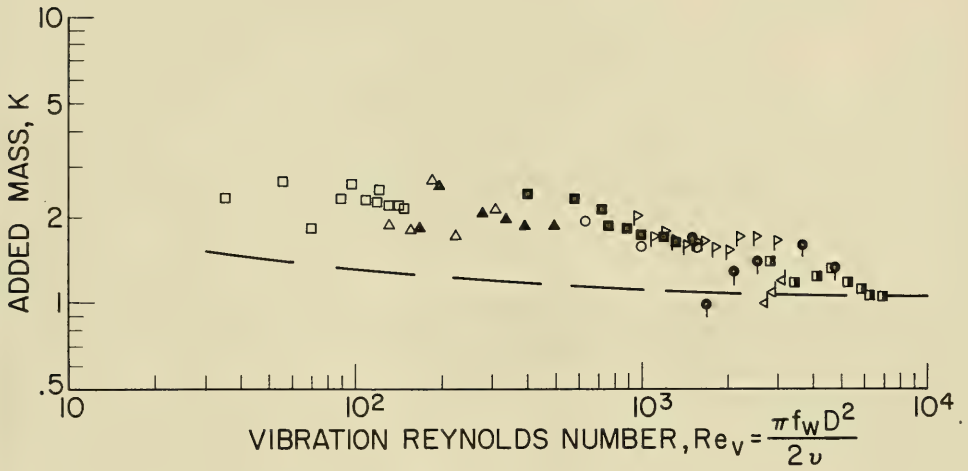

Figure C5 Added mass coefficient C_{am} plotted against vibration Reynolds number Re_v (see Table C2 for legend).

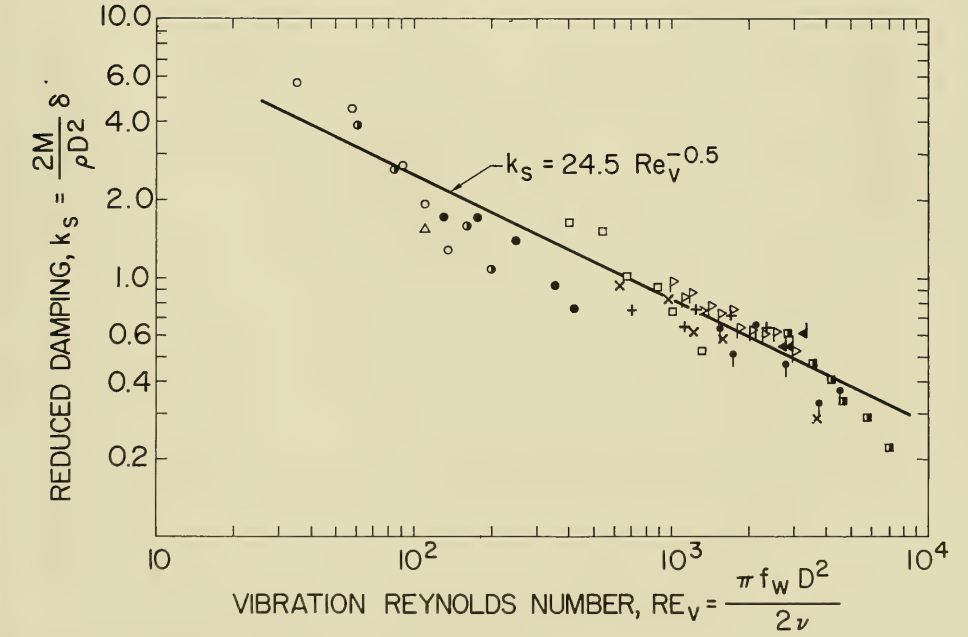

Figure C6 Reduced damping k_s plotted against vibration Reynolds number Re_v (see Table C2 for legend).

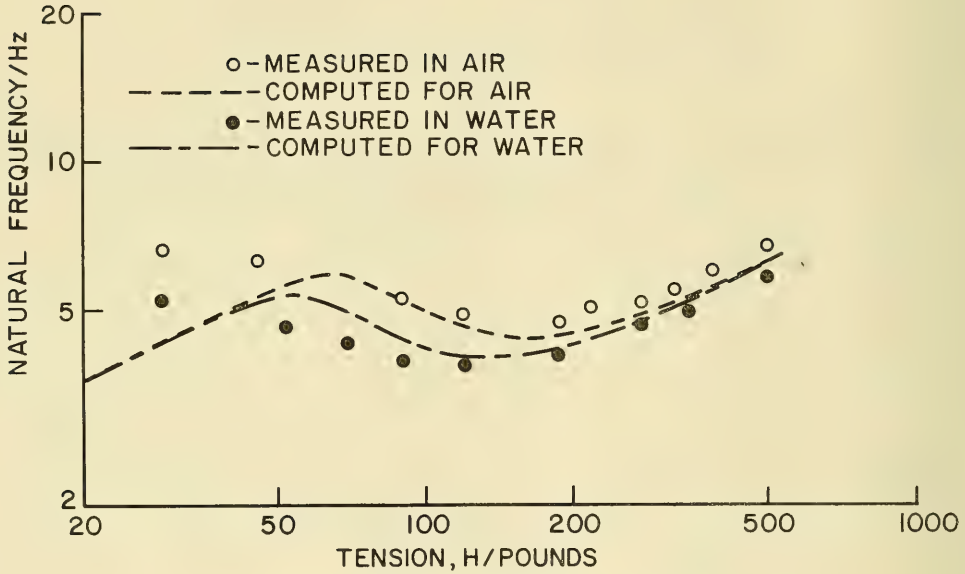

Figure C7 A comparison of the computed natural frequencies of the Double Armor Steel (DAS) cable with measured frequencies in air and in water.

Appendix D

THE "WAKE-OSCILLATOR" MODEL FOR PREDICTING VORTEX-EXCITED OSCILLATIONS

The periodic lift force F_L, characterized by a lift coefficient C_L† which acts on a bluff structure as a result of vortex shedding, is assumed to respond during lock-on or wake capture as would a modified van der Pol oscillator (D1,D2). The governing equation for C_L, in the form employed most recently by Skop and Griffin (D3,D4), is

$$\ddot{C}_L + \omega_S^2 C_L - \left[C_{LO}^2 - C_L^2 - \left(\dot{C}_L/\omega_S\right)^2\right](\omega_S G\dot{C}_L - \omega_S^2 HC_L) = \omega_S F(\dot{\bar{Y}}/D). \tag{D1}$$

Here, a dot denotes differentiation with respect to time t, $\bar{Y}$ is the transverse displacement amplitude of the cylinder due to the incident flow of velocity V, and D is a characteristic transverse dimension (diameter) of the cylinder. The frequency coefficient ω_S (rad/sec) and the four dimensionless coefficients C_{LO}, G, H, and F represent parameters which are to be evaluated from experimental results. It is interesting to note that Iwan and Blevins (D5) and Iwan (D6) have justified the introduction of models similar to equation (D1) from a consideration of the momentum equation for the fluid/structure system.

For flow over a stationary cylinder (that is, for $\bar{Y} = 0$), equation (D1) exhibits a self-excited, self-limited solution given by

$$C_L = C_{LO} \sin \omega_S t. \tag{D2}$$

This result leads to the interpretations of C_{LO} and ω_S as, respectively, the fluctuating lift amplitude and shedding frequency from a stationary cylinder. The shedding frequency ω_S is determined from the Strouhal relation

$$\omega_S = 2\pi StV/D \tag{D3}$$

where St is the Strouhal number.

†The lift force F_L (per unit length along the structure) is normalized by $F_L = 1/2\,\rho V^2\, DC_L$.

The equation of motion of a rigid, spring-mounted cylinder is

$$\ddot{\bar{Y}}/D + 2\zeta\omega_n \dot{\bar{Y}}/D + \omega_n^2 \bar{Y}/D = (\rho V^2 L/2m)\ C_L = \mu\omega_S^2 C_L \tag{D4}$$

where, as noted earlier in the report, $\mu = \rho D^2/8\pi^2 St^2 m$. The natural frequency ω_n and damping ratio ζ are taken for the purpose of modeling as those values measured in a *stationary* fluid having the same physical properties as the flowing fluid.† The solution to the above equations in the entrainment region where resonant oscillations occur is sought as

$$\bar{Y}/D = A \sin \omega t, \tag{D5a}$$

$$C_L/C_{LO} = B \sin (\omega t + \phi). \tag{D5b}$$

Here, ω is the entrainment frequency and the conditions $\omega/\omega_n \approx 1$ and $\omega/\omega_S \approx 1$ are implicitly assumed; A and B are, respectively, amplification factors for the cylinder displacement amplitude and the fluctuating lift.

When equations (D5) are substituted into equations (D1) and (D4), the entrained response is found to be

$$A = (BC_{LO}/S_G)/(\delta^2 + 4)^{1/2}, \tag{D6a}$$

$$B^2 = 1 - (F/GS_G C_{LO}^2)\ [\delta/(\delta^2 + 4)], \tag{D6b}$$

$$\phi = \arctan(-2/\delta), \tag{D6c}$$

where δ must satisfy the cubic equation

$$\delta^3 - \Delta\delta^2 + (4 - HF/\zeta GS_G)\ \delta - 4(\Delta - F/2\zeta S_G) = 0. \tag{D7}$$

In these equations, the detunings δ and Δ are defined by

$$\delta = (2/\zeta)(\omega/\omega_n - 1), \tag{D8a}$$

$$\Delta = (2/\zeta)(\omega_s/\omega_n - 1), \tag{D8b}$$

and the response parameter $S_G = \zeta/\mu$.

It has been shown (D3,D9) that the above equations yield an accurate representation of the entrained resonant response of spring-mounted rigid cylinders when the empirical parameters G, H and F are appropriately selected. Based on an analysis of several diverse sets of experimental data for

†More recent studies (D7,D8) have demonstrated that, for oscillations of bluff cylinders in water, this simplified specification of the damping is not appropriate. This point is discussed in more detail in Appendix C, and the presentation here is meant only to demonstrate the general approach to a "wake-oscillator" type of formulation. For most cylinders in air, the structural damping and the still fluid damping are virtually identical.

resonantly vibrating cylinders, the proper selections *for circular cylinders* were related to the response parameter S_G through the equations

$$\log_{10} G = 0.25 - 0.21\ S_G, \tag{D9a}$$

$$H = \zeta h, \tag{D9b}$$

$$\log_{10} hS_G^2 = -0.83 + 0.98\ S_G, \tag{D9c}$$

$$F = 4GS_G/h. \tag{D9d}$$

When the above relation for F is specified, the stable entrained responses are associated with the solutions of equation (D7) for which $\delta \leqslant 0$. The above relations are valid within the nominal Reynolds number range 400 to 10^5 for which St and C_{LO} are generally constant.* One consequence of equations (D9) is that the maximum cylinder response amplitude A_{MAX} in the entrainment region becomes a function of only S_G. An example of the results that have been obtained with the wake-oscillator model is given in Fig. D1.

The vortex shedding process is strongly dependent on the local amplitude of vibration, but only weakly, or not at all, dependent on the behavior of nearby cable elements. This provides an initial justification for extending the model to elastic cylinders—namely, the equation (D1), without the introduction of any spatial derivatives, should be applicable for describing the vortex-excited oscillating lift force on an elastic, cylindrical structure.

To develop the model for the vortex-excited oscillation of an elastic cylinder, it is useful to adopt a normal mode formulation. Let the vortex-induced displacement $Y(x,t)$ of an elastic cylinder by expressed as

$$Y(x,t) = \sum_i q_i(t)\psi_i(x) \tag{D10}$$

where the $q_i(t)$ are the modal response factors and the $\psi_i(x)$ are the normal modes of the response. The dynamical equations for the $q_i(t)$ are then obtained as

$$\ddot{q}_i + 2\zeta_i\omega_{n,i}\dot{q}_i + \omega_{n,i}^2 q_i = \int_0^L \frac{\rho DV^2 C_L \psi_i(x)\,dx}{2m_i}, \tag{D11}$$

*Available experimental results indicate a lack of coherence in the data for C_{LO}, but the value chosen is reasonable. Different values of C_{LO} require different values of G, H, and F to yield accurate predictions of resonant vibrations. However, changing the value C_{LO} affects only the numerical coefficients F, G, and H and not the functional dependence on S_G.

where, as before, the i^{th} natural frequency $\omega_{n,i}$ and the i^{th} damping ratio ζ_i are those values measured in a *stationary* fluid having the same physical properties as the flowing fluid (see previous footnote). Here m_i is the effective mass of the i^{th} mode of the vibration.

Finally, let the fluctuating lift coefficient C_L in the shedding region be developed as

$$C_L = \sum_i Q_i(t)\psi_i(x), \tag{D12}$$

where the $Q_i(t)$ are the lift response factors. When equation (D12) is substituted into equation (D1), and the latter is multiplied by $\psi_j(x)$ and integrated over the length of the structure, the lift equation for the i^{th} lift response factor reduces to

$$\begin{aligned}\ddot{Q}_i + \omega_S^2 Q_i - \{C_{LO}^2 - I_{iiii}[Q_i^2 + (\dot{Q}_i/\omega_S)^2]\}[\omega_S G_i \dot{Q}_i - \omega_S^2 H_i Q_i] \\ + \sum\sum\sum I_{ijkl}[\omega_S G_i \dot{Q}_j Q_k Q_l + (G_i/\omega_S)\dot{Q}_j \dot{Q}_k \dot{Q}_l \\ - \omega_S^2 H_i Q_j Q_k Q_l - H_i Q_j \dot{Q}_k \dot{Q}_l] = \omega_S F_i \dot{q}_i/D;\ j,k,l \neq i \text{ simultaneously}\end{aligned} \tag{D13}$$

where

$$\begin{aligned}I_{ijkl} &= (m/m_i)\int_0^L \psi_i\psi_j\psi_k\psi_l dx \\ &= \int_0^L \psi_i\psi_j\psi_k\psi_l dx \Big/ \int_0^L \psi_i^2 dx.\end{aligned} \tag{D14a}$$

This equation of motion for the structure reduces to

$$\ddot{q}_i/D + 2\zeta_i\omega_{n,i}\dot{q}_i/D + \omega_{n,i}^2 q_i/D = \omega_S^2 \mu_{ii} Q_i, \tag{D14b}$$

where

$$\mu_{ii} = \rho D^2/8\pi^2 S^2 m \tag{D14c}$$

is a constant and m is the virtual mass per unit length of the structural member.

The undamped linear equivalents to the governing equations show that if the system is responding at a frequency ω then $q_i \propto Q_i/[1 - (\omega/\omega_{n,i})^2]$ and $Q_i \propto q_i/[1 - (\omega/\omega_S)^2]$. Thus, for $\omega/\omega_{n,i} \approx 1$ and $\omega/\omega_S \approx 1$ simultaneously, the equivalent linear solution reveals that the i^{th} vibration mode undergoes a resonant type behavior while the remaining vibration modes remain small. Hence, for the flow condition $\omega_S \approx \omega_{n,i}$, the solution to the equation (D14) is sought as the pure mode form

$$q_i/D = A_i \sin \omega t \tag{D15a}$$

$$q_j = 0, \; j \neq i \tag{D15b}$$

$$Q_i / C_{LO} = B_i \sin(\omega t + \phi_i) \tag{D15c}$$

$$Q_j = 0, \; j \neq i. \tag{D15d}$$

Here again A_i and B_i are modal amplification factors for the cylinder displacement and fluctuating lift, and ϕ_i is the phase of the fluctuating lift relative to the cylinder displacement. The conditions $\omega/\omega_{n,i} \approx 1$ and $\omega/\omega_S \approx 1$ imposed on the response frequency ω must be satisfied for the assumed solution to be valid.

The entrained pure mode response of the system is found to be

$$A_i = (B_i C_{LO}/S_{G,i})/(\delta_i^2 + 4)^{1/2}, \tag{D16a}$$

$$B_i^2 = (1/I_{iiii})\{1 - (F_i/G_i S_{G,i} C_{LO}^2)[\delta_i/(\delta_i^2 + 4)]\}, \tag{D16b}$$

$$\phi_i = arctan\ (-2/\delta_i), \tag{D16c}$$

where δ_i must satisfy the cubic equation

$$\delta_i^3 - \Delta_i \delta_i^2 + (4 - H_i F_i/\zeta_i G_i S_{G,i})\delta_i - 4(\Delta_i - F_i/2\zeta_i S_{G,i}) = 0, \tag{D17}$$

and where

$$\delta_i = (2/\zeta_i)(\omega/\omega_{n,i} - 1), \tag{D18a}$$

$$\Delta_i = (2/\zeta_i)(\omega_S/\omega_{n,i} - 1), \tag{D18b}$$

$$S_{G,i} = \zeta_i/\mu_{ii}. \tag{D18c}$$

These equations for the i^{th} pure mode response are identical to the equations for the vortex-excited response of a rigid, spring-mounted cylinder except for the multiplicative factor of $I_{iiii}^{-1/2}$ appearing in the equation for B_i. Hence, the behavior of the i^{th} modal response as a function of Δ_i, or $\omega_S/\omega_{n,i}$, is similar to the behavior of the rigid, spring-mounted cylinder, complete discussions of which of can be found elsewhere (D9).

The vortex-excited oscillation of an elastic cylinder under the condition $\omega_S \approx \omega_{n,i}$ is

$$\bar{Y}(x,t)/D = A_i \psi_i(x) \sin \omega t.$$

The maximum oscillation amplitude $\bar{Y}_{i,MAX}(x)$ in the i^{th} pure mode entrainment region is then

$$\bar{Y}_{i,MAX}(x)/D = A_{i,MAX}|\psi_i(x)|$$

where $A_{i,MAX}$ is a function only of the modal response parameter $S_{G,i}$. This equation can also be written in the form

$$\overline{Y}_{i,MAX}(x)/D = A_{MAX}(S_{G,i})\, I_i^{-\frac{1}{2}} |\psi_i(x)| \tag{D19}$$

where A_{MAX} is the maximum response amplitude for a rigid, spring-mounted cylinder ($\psi_i = 1, \psi_{i \neq 1} = 0$) having a cross-section similar to the elastic cylinder. Here the notation for the multiplicative factor I_{iii} is simplified to I_i. The parameters F_i, G_i, H_i in equations can be obtained from equations (D9) when the modal response parameter $S_{G,i} = \zeta_i/\mu_{ii}$ is known. Then not only the amplitude response but also such system features as the lift response and phase between the lift force and structural motion can be obtained from equations (D16), as demonstrated in detail elsewhere (D10). Additional discussion of the wake-oscillator approach can be found in a recent textbook on wind engineering by Simiu and Scanlan (D11), the proceedings of a recent international conference on wind engineering (D12), and in the discussions of a recent colloquium on vortex shedding from bluff bodies (D13).

References

D1. R.E.D. Bishop and A.Y. Hassan, "The Lift and Drag Forces on a Circular Cylinder in a Flowing Fluid," Proceedings of the Royal Society of London, Series A, Vol. 277, pp. 31-75, 1964.

D2. R.T. Hartlen, W.D. Baines and I.G. Currie, "Vortex-Excited Oscillations of a Circular Cylinder," University of Toronto Technical Report 6809, 1968.

D3. R.A. Skop and O.M. Griffin, "On a Theory for the Vortex-Excited Oscillations of a Flexible Cylindrical Structure," Journal of Sound and Vibration, Vol. 41, pp. 263-274, 1975.

D4. O.M. Griffin and R.A. Skop, "The Vortex-Induced Oscillations of Structures," Journal of Sound and Vibration, Vol. 44, pp. 303-305, 1976.

D5. W.D. Iwan and R.D. Blevins, "A Model for the Vortex-Induced Oscillation of Structures," Transactions of ASME, Journal of Applied Mechanics, Vol. 41, pp. 581-585, 1974.

D6. W.D. Iwan, "The Vortex-Induced Oscillation of Elastic Structural ELements," Transaction of ASME, Journal of Engineering for Industry, Vol. 97, pp. 1378-1382, 1975.

D7. T. Sarpkaya, "Vortex-Induced Oscillations: A Selective Review," Transactions of ASME, Journal of Applied Mechanics, Vol. 46, pp. 241-258, 1979.

D8. O.M. Griffin, "Vortex-Excited Cross Flow Vibrations of a Single Cylindrical Tube," Transactions of ASME, Journal of Pressure Vessel Technology, Vol. 102, pp. 158-166, 1980.

D9. R.A. Skop and O.M. Griffin, "A model for the vortex-excited response of bluff cylinders," Journal of Sound and Vibration," Vol. 27, pp. 225-233, 1973.

D10. O.M. Griffin, R.A. Skop and G.H. Koopmann, "The Vortex-Excited Resonant Vibrations of Circular Cylinders," Journal of Sound and Vibration, Vol. 31, pp.235-249, 1973.

D11. E. Simiu and R.A. Scanlan, *Wind Effects on Buildings and Structures: An Introduction to Wind Engineering,* Wiley-Interscience: New York, 1978.

D12. J. Cermak (ed.), *Proceedings of the Fifth International Conference on Wind Engineering (Preprints),* Colorado State University: Fort Collins, Colorado, July 1979.

D13. P.W. Bearman and J.M.R. Graham, "Vortex Shedding from Bluff Bodies in Oscillatory Flow: A Report on Euromech 119," Journal of Fluid Mechanics, Vol. 99, Part 2, 225-246, 1980.

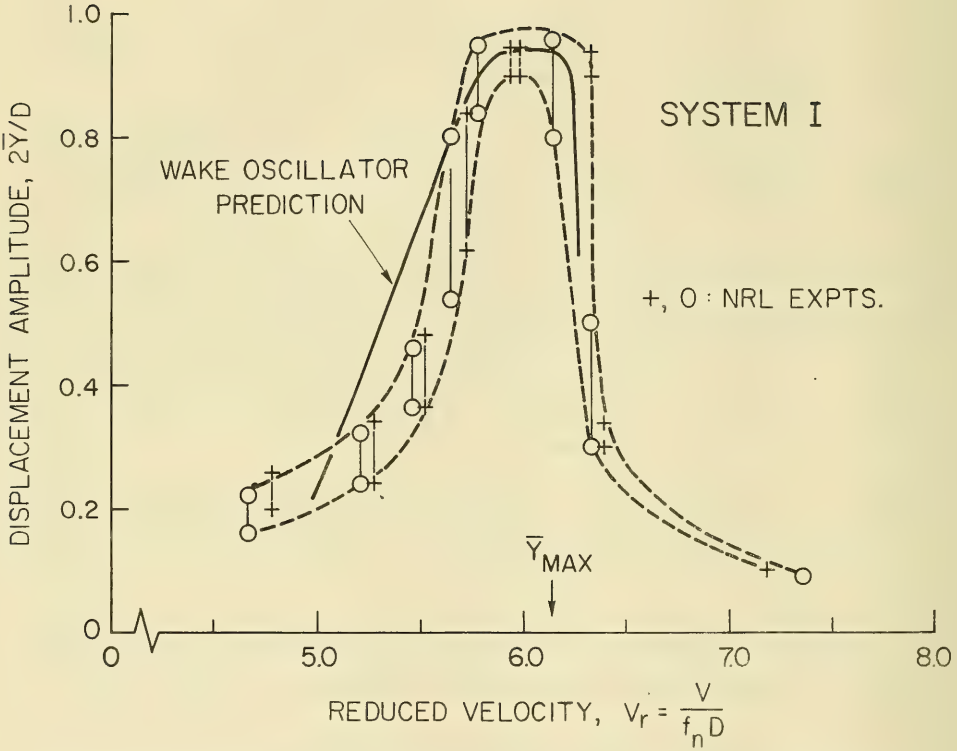

Figure D1 Lift amplification $C_{L'}/C_{LO}$ and cross flow displacement amplitude $\bar{Y}/D$, for a spring-mounted rigid cylinder in air, plotted against the reduced velocity $V_r = V/f_n D$.

Legend for data:

Wake-oscillator model prediction: ——. Wind tunnel measurements ($\zeta_s/\mu = 0.5$, Re = 500 to 900): +, speed increasing; 0, speed decreasing.

Appendix E

OTHER CABLE STRUMMING PREDICTION MODELS

The "wake-oscillator" model described in the previous appendix is but one of the several models for predicting the response of bluff structures to vortex shedding-induced forces. However, most of these other models have not been sufficiently extended to the case of an arbitrary flexible body such as a cable. The several categories of predictive models are:

- Empirical models, in which the hydrodynamic forces are derived from experiments;
- Random vibration models, in which the vortex forcing and cable response are modeled as stochastic processes;
- Discrete vortex methods, in which the flow field parameters and the hydrodynamic forces are computed from the motions of arrays of discrete vortices inserted into the flow;
- Numerical solution of the Navier-Stokes equations, in which the complete equations of unsteady fluid motion are integrated numerically.

The first two methods have been developed specifically toward applications to predicting the vortex-excited oscillations of flexible members such as cables. The third and fourth methods are, except for special cases, limited to problems in two dimensions. These methods have not been extended to practical design problems but they have employed in basic fluid dynamic studies.

E.1 The Prediction of Strumming Parameters from Measured Force Coefficients. The equation for the resonant cross flow vibration of an elastically-mounted, rigid cylindrical structure, *with the vortex and vibration frequencies locked on*, can be written in general as

$$\ddot{y} + 2\zeta_s \dot{y} + y = \mu \left(\frac{\omega_s}{\omega_n}\right)^2 (\tilde{C}_L - \tilde{C}_R), \tag{E.1.1}$$

where the dot $(\cdot)$ notation denotes differentiation with respect to time. Here $y = \bar{y}/D$, $\tau = \omega_n t$, the mass ratio $\mu = \dfrac{\rho D^2}{8\pi^2 St^2 m}$ and ζ_s is the *structural* damping ratio. The fluid force coefficients are

$$\text{Lift: } \tilde{C}_L = \frac{\bar{F}_L}{1/2\rho V^2 D} = C_L \sin(\alpha\tau + \phi),\ \alpha = \frac{\omega}{\omega_n}, \tag{E.1.2a}$$

$$\text{Reaction: } \tilde{C}_R = \frac{\bar{F}_R}{1/2\rho V^2 D} = C_R \sin(\alpha\tau + \phi_1),\ \alpha = \frac{\omega}{\omega_n}, \tag{E.1.2b}$$

as suggested by Griffin and Koopmann (E1), Griffin (E2) and Chen (E3), where ϕ and ϕ_1 are the phase angles between the lift and the displacement and between the reaction and the acceleration, respectively. The two forces represented by $\tilde{C}_L$ and $\tilde{C}_R$ are orthogonal (E2).

If the cross flow displacement y is written as

$$y = Y \sin \alpha\tau, \quad \alpha = \frac{\omega}{\omega_n},$$

with $Y = \bar{Y}/D$, then the equation of motion separates into

$$\sin \alpha\tau: \ -\alpha^2 Y + Y - \mu \left(\frac{\omega_s}{\omega_n}\right)^2 (C_L \cos\phi - C_R \cos\phi_1) = 0 \tag{E.1.3a}$$

$$\cos \alpha\tau: \ 2\zeta_s Y - \mu \left(\frac{\omega_s}{\omega_n}\right)^2 (C_L \sin\phi - C_R \sin\phi_1) = 0 \tag{E.1.3b}$$

when the coefficients of $\sin \alpha t$ and $\cos \alpha t$ are grouped appropriately. The various force components are identified as follows:

STRUCTURAL				FLUID			
INERTIA	AND	STIFFNESS		INERTIA	AND	ADDED MASS	
$-\alpha^2 Y$	+	Y	=	$\mu \left(\frac{\omega_s}{\omega_n}\right)^2 (C_L \cos\phi - C_R \cos\phi_1)$			(E.1.4a)

STRUCTURAL DAMPING | FLUID EXCITATION AND DAMPING

$$+ 2\zeta_s Y = \mu\left(\frac{\omega_s}{\omega_n}\right)^2 (C_L \sin\phi - C_R \sin\phi_1). \qquad \text{(E.1.4b)}$$

A decomposition of the system such as this allows the fluid and structural force contributions to be separated completely. The various fluid forces then can be measured individually or derived from the total measured force.

Using a different approach Sarpkaya (E4, E5) has expressed the measured total fluid force on a resonantly vibrating cylinder as the sum of two components

$$C_{\text{TOTAL}} = \frac{\bar{F}}{\frac{1}{2}\rho V^2 D} = C_{mh} \sin\alpha\tau - C_{dh} \cos\alpha t, \qquad \text{(E.1.5)}$$

where C_{mh} is an "inertia" force and C_{dh} is a "drag" force. These components are related to Sarpkaya's "generalized force coefficients" C_{dl} and C_{ml} (E5), see Figs. 2.3 to 2.6, by

$$C_{dh} = \frac{8}{3\pi} C_{dl} \left(2\pi \frac{\bar{Y}}{D}\right)^2 V_r^{-2} \qquad \text{(E.1.6a)}$$

and

$$C_{mh} = \pi^2 C_{ml} \left(2\pi \frac{\bar{Y}}{D}\right) V_r^{-2} \qquad \text{(E.1.6b)}$$

where V_r is the "reduced velocity" $V_r = \frac{2\pi V}{\omega_n D}$ or $\frac{V}{f_n D}$.

In this case the equation of motion for the cylinder becomes

$$\ddot{y} + 2\zeta_s \dot{y} + y = \mu\left(\frac{\omega_s}{\omega_n}\right)^2 (C_{mh} \sin\alpha\tau - C_{dh} \cos\alpha\tau) . \qquad \text{(E.1.7)}$$

The force component C_{dh} is negative when energy is transferred to the cylinder, as is the case for resonant, vortex-excited oscillations. If a steady-state response is assumed, then

$$y = Y \sin(\alpha\tau - \epsilon) ,$$

where ϵ is an undefined phase angle. This form of the equation of motion separates into

$$\sin\alpha\tau: -\alpha^2 Y \cos\epsilon + 2\zeta_s Y \sin\epsilon + Y \cos\epsilon - \mu\left(\frac{\omega_s}{\omega_n}\right)^2 C_{mh} = 0 \qquad \text{(E.1.8a)}$$

and

$$\cos \alpha\tau: \alpha^2 Y \sin \epsilon + 2 \zeta_s Y \cos \epsilon - Y \sin \epsilon + \mu \left(\frac{\omega_s}{\omega_n}\right)^2 C_{dh} = 0 \qquad \text{(E.1.8b)}$$

when the coefficients of $\sin \alpha\tau$ and $\cos \alpha\tau$ are again grouped appropriately.

Upon rearranging, these equations reduce to

STRUCTURAL INERTIA		STRUCTURAL STIFFNESS		FLUID FORCE TERMS		(E.1.9a)
$-\alpha^2 Y$	+	Y	$= \mu \left(\frac{\omega_s}{\omega_n}\right)^2$	$[C_{dh} \sin \epsilon - C_{mh} \cos \epsilon]$		
STRUCTURAL DAMPING				FLUID FORCE TERMS		
$2 \alpha \zeta_s Y$			$= \mu \left(\frac{\omega_s}{\omega_n}\right)^2$	$[-C_{dh} \cos \epsilon + C_{mh} \sin \epsilon]$.		(E.1.9b)

which are of the same form as those derived above. The two approaches are in fact identical when

$$C_L \sin \phi = - C_{dh} \cos \epsilon, \qquad \text{EXCITATION}^\dagger \qquad \text{(E.1.10a)}$$

$$C_L \cos \phi = C_{dh} \sin \epsilon, \qquad \text{FLUID INERTIA} \qquad \text{(E.1.10b)}$$

$$C_R \sin \phi_1 = -C_{mh} \sin \epsilon, \qquad \text{FLUID REACTION (DAMPING)} \qquad \text{(E.1.10c)}$$

$$C_R \cos \phi_1 = C_{mh} \cos \epsilon, \qquad \text{ADDED MASS} \qquad \text{(E.1.10d)}$$

These relations can be used to compare recent measurements of the various force components. Blevins (E6) also has proposed the use of a force decomposition such as that given by equations (E.1.4b) and (E.1.9b).

†These equations are discussed further in Reference E2.

These solutions are based upon the assumption that the fluid forces are independent of the resonant motion of the cylinder. In reality, there is a complex nonlinear dependence between the fluid forces and the displacement, c.f., Fig. 2.7. Also, the maximum displacement is dependent upon the mass ratio and structural damping of the cylinder and its mountings. When the force coefficients are assumed to be known, as from experiments, as shown in Figs. 2.3 to 2.6, these analytical models can be used to predict the cylinder displacement and vice versa. A more complete development of these equations is given by Griffin (E2, E7).

It is a relatively simple matter to extend the analysis to the case of a flexible cylinder such as a cable with a normal mode shape $\psi_i(z)$, following the "wake-oscillator" formulations described in Appendix D. If a pure mode response is assumed, then the displacement of the flexible cylinder is

$$Y_i = Y\,\psi_i(z)\,\sin\alpha\tau \tag{E.1.11}$$

at each spanwise point $z = \bar{z}/L$, and the maximum displacement is scaled by the factor

$$Y_{EFF,MAX} = Y\,I_i^{1/2} \;/\; |\tilde{\psi_i}(z)|_{MAX} = Y/\gamma_i \tag{E.1.12}$$

where

$$I_i = \frac{\int_0^1 \psi_i^4\,(z)\,dz}{\int_0^1 \psi_i^2\,(z)\,dz} \text{ and } \gamma_i = \frac{|\psi_i(z)|_{MAX}}{I_i^{1/2}} \tag{E.1.13}$$

for a cylinder of length L. For the special case of a circular cylinder $I_i = |\psi_i(z)|_{MAX} = 1$, and other values of I_i and ψ_i for a variety of flexible cylindrical cross-sections are tabulated in Table E1. The parameter γ_i can be calculated directly from the entries in the table.

The model just discussed also can be extended to the case of a flexible cylinder by means of a normal mode approach. The cross flow displacement of the cylinder is assumed to take the form

$$y(z,t) = \sum_{i=1}^{\infty} Y_i(t)\,\psi_i(z) \tag{E.1.14}$$

which is a standard expansion of the normal modes. When equation (E.1.14) is substituted into equation (E.1.1), the result is a generalized form for the equation of motion given by

$$\sum_{i=1}^{\infty}(m(z)\,Y_{i,tt}+2m(z)\omega_{ni}\,\zeta_{si}\,Y_{i,t}+m(z)\omega_{ni}^2\,Y_i)\psi_i =$$

$$\frac{\rho\,D^2\,\omega_s^2}{8\pi^2 St^2}\,(\tilde{C}_L-\tilde{C}_R) \tag{E.1.1a}$$

where, in general $\tilde{C}_L$ and $\tilde{C}_R$ are assumed to be functions of both z and t, and the mass per unit length m is a function of z. If this equation is multiplied through by $\psi_j(z)$ and integrated over the length $L\,(z=\bar{z}/L)$ of the cylinder, then the balance of forces for the ith mode is

$$(Y_{i,tt}+2\,\omega_{ni}\,\zeta_{si}\,Y_{i,t}+\omega_{ni}^2\,Y_i)\left(\int_0^1\psi_i^2(z)m(z)\,dz\right)=$$
$$\frac{\rho D^2\omega_s^2}{8\pi^2 St^2}\left[\int_0^1\tilde{C}_L\psi_i(z)\,dz-\int_0^1\tilde{C}_R\psi_i(z)\,dz\right] \tag{E.1.15}$$

when the normal modes of the structure satisfy the orthogonality condition

$$\int_0^1 m(z)\psi_i(z)\,\psi_j(z)\,dz=\begin{vmatrix}0 & i\neq j\\ m & i=j\end{vmatrix}. \tag{E.1.16}$$

In terms of the variables given in the first paragraph of this section, equation (E.1.15) reduces to

$$\omega_{ni}^2(\ddot{Y}_i+2\zeta_{si}\,\dot{Y}_i+Y_i)=\frac{\rho D^2\omega_s^2}{8\pi^2 St^2}\left\{\frac{\int_0^1\tilde{C}_L\psi_i(z)\,dz}{\int_0^1 m(z)\psi_i^2(z)\,dz}-\frac{\int_0^1\tilde{C}_R\psi_i(z)\,dz}{\int_0^1 m(z)\psi_i^2(z)\,dz}\right\}, \tag{E.1.17}$$

where Y_i is the generalized displacement and the integrals on the right-hand side are generalized force coefficients. When "equivalent" force coefficients and the "equivalent" mass are introduced by

$$\tilde{C}_{LE}=\frac{\int_0^1\tilde{C}_L\psi_i(z)\,dz}{\int_0^1\psi_i(z)\,dz}, \tag{E.1.18a}$$

$$\tilde{C}_{RE}=\frac{\int_0^1\tilde{C}_R\psi_i(z)\,dz}{\int_0^1\psi_i(z)\,dz}, \tag{E.1.18b}$$

and

$$m_E=\frac{\int_0^1 m(z)\psi_i^2(z)\,dz}{\int_0^1\psi_i^2(z)\,dz}, \tag{E.1.18c}$$

the equation of motion reduces to

$$\ddot{Y}+2\zeta_s\dot{Y}+Y=\mu\left(\frac{\omega_s}{\omega_n}\right)^2(\tilde{C}_{LE}-\tilde{C}_{RE})\frac{\int_0^1\psi(z)\,dz}{\int_0^1\psi^2(z)\,dz}. \tag{E.1.18d}$$

The subscript i is dropped since a single mode response is understood in this equation. In the case of the flexible cylindrical structure, such as a cable, a work and energy balance as discussed by Griffin (E2,

E7) and Sarpkaya (E4) leads to the result

$$2\zeta_s \int_0^{\omega_n T} (\dot{Y})^2 dt = \pi\mu \left(\frac{\omega_s}{\omega_n}\right)^2 (C_{LE} Y \sin\phi - C_{RE} Y \sin\phi_1) \frac{\int_0^1 \psi(z)\,dz}{\int_0^1 \psi^2(z)\,dz}$$

where C_{LE} and C_{RE} are "equivalent" force coefficients similar in form to those given by equation (E.1.18).

E.2 Random Vibration Models. Predictive models for vortex shedding-induced oscillations based on a random vibration approach have been introduced by Blevins and Burton (E8) and by Kennedy and Vandiver (E9). The latter model is tailored specifically toward the prediction of cable strumming oscillations which are not in complete resonance with the vortex shedding. The former model is a pure-mode approach, based upon an assumption of resonant interaction between the body and the fluid. Also, the model equations are derived for arbitrary flexible cylinders, of which the cable is but one specific example.

Blevins and Burton (E8) derive the equation of motion for a flexible cylinder in a manner similar to that given in Section E.1. It is then assumed that

$$\hat{y}^2 = \int_0^\infty \frac{\int_0^L \int_0^L S_F(z_1,z_2,\omega)\psi(z_1)\psi(z_2)\,dz_1 dz_2}{|z(\omega)|^2 \left[\int_0^L \psi^2 dz\right]^2}\, d\omega \qquad \text{(E.2.1)}$$

where $\hat{y}$ is the rms cross flow response and $S_F(z_1,z_2,\omega)$ is the cross spectral density of the vortex-induced lift force, and $z(\omega)$ is the impedance of the system. This equation reduces to

$$\overline{Y}/D = \frac{\pi}{(2\pi St)^2 k_s} \left(\frac{\int_0^L \psi\,dz}{\int_0^L \psi^2 dz}\right) C_{LE} \qquad \text{(E.2.2)}$$

where the equivalent excitation force coefficient, C_{LE}, is

$$C_{LE}^2 = \frac{K_1^2 K_2^2 \int_0^L \int_0^L g(z_1) g(z_2) r(z_1 - z_2) \psi(z_1)\psi(z_2)\,dz_1 dz_2}{\left[\int_0^L \psi\,dz\right]^2} \qquad \text{(E.2.3)}$$

In this equation $K_1 K_2 g(z)$ is the rms lift coefficient at the spanwise location z and $r(z_1 - z_2)$ is the spanwise correlation coefficient. K_1 and K_2 are arbitrary constants. The correlation coefficient is specified from experimental measurements on a cable or cylinder at resonance.

Blevins and Burton have applied their formulation to a number of specific cases. One such case is plotted in Fig. E1 where the predicted peak displacement amplitude for a sine mode (taut cable) at resonance is plotted. At the lower displacement amplitudes the cable response is dependent upon the correlation length, but only a single prediction is the result at displacement amplitudes above $\overline{Y} \approx 0.3$ D. The limiting value of $\overline{Y}/D$ (see Fig. 2.2) is 1.2 for the particular case of a cable as shown in Fig. E1.

Kennedy and Vandiver (E9) have introduced a stochastic model for the cross flow strumming response of marine cables. The lift coefficient C_{LE} in the non-lock-on regime is assumed to be a narrow band random variable centered about a local Strouhal frequency that is characterized by its correlation function or its power spectrum. Much the same approach as had been used by Blevins and Burton is employed, except that the response of the cable is treated as a forced oscillation. A normal mode response with mode shape ψ_j and modal frequencies f is assumed, and the modal force spectrum is given by

$$S_{F_{jK}}(f) = \int_0^L \int_0^L \psi_j(z_1)\psi_k(z_2) S_F(z_1,z_2,f)\, dz_1 dz_2. \tag{E.2.4}$$

In the analysis cross terms ($j \neq k$) are assumed to be small in relation to the modal response for which $j = k$. The response and force spectra are then related by

$$S_{\bar{y}}(z_1,z_2,f) = \sum_j \psi_j(z_1)\psi_j(z_2)|H_j(f)|^2 S_{Fj}(f) \tag{E.2.5}$$

where

$$S_{Fj}(f) = \int_0^L \int_0^L \psi_j(z_1)\psi_j(z_2) S_F(z_1,z_2,f)\, dz_1 dz_2.$$

The total displacement response spectrum then is the sum of the individual modal response spectra that are included in the excitation bandwidth. Kennedy and Vandiver have applied their model to two practical problems: the response of a nonuniform cable in a uniform flow and the case of a uniform cable in a nonuniform (shear) flow. These problems are discussed in detail in reference E9.

Forced vibration models based upon random oscillations have been introduced by Howell (E10) and Kwok and Melbourne (E11) for the purpose of predicting the cross flow response of aeroelastic structures in turbulent shear flows.

E.3 Discrete Vortex Methods. The discrete vortex method (DVM) is a potential flow representation of the separated shear layers and vortex wake of a body from which flow separation has taken place. The DVM approach has been applied recently to the case of a freely oscillating circular cylinder by Sarpkaya and Shoaff (E12,E13). The method has only come into general usage with the advent of modern high speed computers, and applications of the method have dealt primarily with modeling the flow separation from two-dimensional bodies with fixed separation points as described by Maull (E14) and Clements and Maull (E15). Stansby (E16) has applied the DVM approach to the periodic flow past a circular cylinder in order to model wave/structure interactions. The history of the method and the mathematical details of it are discussed by Sarpkaya and Shoaff (E12) and by Clements and Maull (E15).

A problem with implementing the DVM approach has been the number of empirical parameters that must be employed to minimize undesirable features. These features include instability of the vortex sheets, the need for extreme accuracy of the flow field in the vicinity of the separation point, and the difficulty in tracking the evolution of a random distribution of discrete vortices. Sarpkaya and Shoaff appear to have minimized these problems by the introduction of a boundary layer calculation on the cylinder to precisely determine both the location of the separation point and the amount of shed vorticity and by a method of rediscretization for the evolving vortex sheets. The evolution of the vortex wake behind a vibrating circular cylinder is shown in Fig. E2. The arrow in each step of the figure represents the incident flow relative to the cylinder. By application of Blasius' theorem to the flow the time-dependent and steady fluid forces can be calculated. The form of the equation employed by Sarpkaya and Shoaff is

$$C_D + iC_L = i \sum_{n=1}^{N} \Gamma_n \left[\overline{(\dot{z}_n - \dot{z}_0)} - \overline{\dot{(z_n - z_0)^{-1}}} \right] - i\dot{z}_0 \sum_{n=1}^{N} \Gamma_n - \pi \ddot{z}_0. \tag{E.3.1}$$

Here z_0 denotes the (complex) position of the center of the cylinder and the $(\cdot)$ notation denotes differentiation with respect to time. The circulation and location of the nth discrete vortex in the wake are given by Γ_n and z_n, respectively, and the second term in the brackets represents the image point of the nth discrete vortex within the cylinder. It is readily seen from equation (E.3.1) that the forces on

the body are critically dependent upon the strength (circulation) and location of the discrete vortices. These parameters are in turn dependent upon the starting conditions (separation point, magnitude of the vorticity, number of vortices, etc.) and upon the evolution of the vortices.

It is possible to predict the major features of the complex nonlinear interaction that characterizes vortex-excited oscillations, but application of the discrete vortex method (DVM) is thus far limited to the case of a rigid cylinder. Although Sarpkaya and Shoaff (E12, E13) have made considerable progress in limiting the number of empirical parameters that must be used with the DVM and have achieved good agreement with rigid cylinder experiments, the prediction of the vortex-excited response of flexible bluff bodies such as cables and marine pilings will require the formidable step to a three-dimensional code. Moreover, the effects of yaw angle, shear, and roughness will no doubt be extremely difficult to incorporate into the boundary layer calculations, i.e. starting conditions, without resort to further empiricisms.

E.4 Numerical Models. Few, if any, numerical models for calculating the flow around bluff bodies have been developed for practical applications. This is primarily due to the difficulties that are encountered in achieving the required small grid sizes and time steps as the Reynolds number is increased to a practical value (say $Re \approx 200$ at a minimum). The numerical solution of the Navier-Stokes equations of motion for flow past a cylinder are highly sensitive to the grid size, especially near the cylinder, and to the time step size.

A numerical solution of the Navier-Stokes equations for the flow around a circular cylinder was obtained recently by Hurlbut, Spaulding and White (E17, E18). Three cases were considered: a cylinder vibrating in a still fluid, a cylinder vibrating in line with an incident uniform flow, and a cylinder vibrating normal to an incident uniform flow. The maximum Reynolds number achieved was $Re = 100$. The solution of the governing equations in the presence of the oscillating cylinder was achieved by transforming the equations for the computational grid system to a noninertial (accelerating) system. Good quantitative agreement was achieved with experimental data for the steady drag and unsteady lift forces on a vibrating cylinder at $Re = 80$. The computer model developed by Hurlbut,

Spaulding and White (E17, E18) presently is being extended to Re = 200 in order to model numerically the drag and lift forces on a vibrating cylinder.

Virtually all computations of the flow past bluff bodies (except for the discrete vortex model described earlier) have been based upon a finite-difference approximation to the governing equations where the continuum is represented by a grid of discrete points. Recently, however, the finite-element method has been extended to the modeling of the time-dependent flow over a (stationary) cylinder (E19). The finite element method in this case approximates the fluid continuum by some form of weighted-residual average of the governing equations over elemental volumes (three dimensions) or an elemental areas (two dimensions). Several finite element formulations were employed by Greshko, Lee and Upson (E19) to solve the problem of flow past a stationary circular cylinder at Re $\approx$ 100. Some promising results were obtained, but the numerical solution was shown to be highly dependent upon the choice of element (simple versus higher-order) and other considerations (lumped mass versus conventional mass matrices). The prospect of three-dimensional computations by any of the Navier-Stokes numerical methods is conceptually straightforward but is at the same time sobering financially.

References

E1. O.M. Griffin and G.H. Koopmann, "The Vortex-Excited Lift and Reaction Forces on Resonantly Vibrating Cylinders," Journal of Sound and Vibration, Vol. 54, 435-448, 1977.

E2. O.M. Griffin, "Vortex-Excited Cross Flow Vibrations of a Single Cylindrical Tube," in *Flow Induced Vibrations,* S.S. Chen and M.D. Bernstein (eds.), ASME: New York, 1-10 (June 1979); see also Transactions of ASME, Journal of Pressure Vessel Technology, Vol. 102, No. 2, 158-166, 1980.

E3. S.S. Chen, "Crossflow-Induced Vibrations of Heat Exchanger Tube Banks," Nuclear Engineering and Design, Vol. 47, 67-86, 1978.

E4. T. Sarpkaya, "Vortex-Induced Oscillations—A Selective Review," Transactions of ASME, Journal of Applied Mechanics, Vol. 46, 241-258, 1979.

E5. T. Sarpkaya, "Transverse Oscillation of a Circular Cylinder in Uniform Flow," Proceedings of the ASCE, Journal of the Waterways, Port, Coastal and Ocean Division, Vol. 104, 275-290, 1978.

E6. R.D. Blevins, *Flow-Induced Vibrations,* Van Nostrand Reinhold: New York, 1977.

E7. O.M. Griffin, "OTEC Cold Water Pipe Design for Problems Caused by Vortex-Excited Oscillations," NRL Memorandum Report 4157, March 1980.

E8. R.D. Blevins and T.E. Burton, "Fluid Forces Induced by Vortex Shedding," Transactions of ASME, Journal of Fluids Engineering, Vol. 98, 19-27, 1976.

E9. M. Kennedy and J.K. Vandiver, "A Random Vibration Model for Cable Strumming Prediction," CIVIL ENGINEERING IN THE OCEANS IV, Vol. I, 273-292, ASCE: New York, September 1979.

E10. J.F. Howell, "Soil-Structure Interaction Under Wind Loading," Ph.D. Thesis, University of Western Ontario, London, Ont., April 1978.

E11. K.C.S. Kwok and W.H. Melbourne, "Cross-Wind Response Due to the Cross-Stream Vibration of Circular Cylinders in Uniform and Shear Flows," in Proc. Fifth Int. Conf. on Wind Engrg. (Preprints), Vol. II, Fort Collins, CO, Paper VI-4, July 1979.

E12. T. Sarpkaya and R.L. Shoaff, "Discrete Vortex Analysis of Transverse Oscillations of a Circular Cylinder in Uniform Flow," Naval Postgraduate School Report NPS-69SL79011, January 1979.

E13. T. Sarpkaya and R.L. Shoaff, "Numerical Modelling of Vortex-Excited Oscillations," CIVIL ENGINEERING IN THE OCEANS IV, Vol. I, 504-517, ASCE: New York, September 1979.

E14. D.J. Maull, "An Introduction to the Discrete Vortex Model," Cambridge University Engineering Department Report CUED/A-Aero/TR8, 1979.

E15. R.R. Clements and D.J. Maull, "The Representation of Sheets of Vorticity by Discrete Vortices," Progress in Aerospace Science, Vol. 16, No. 2, 129-146, 1975.

E16. P.K. Stansby, "An inviscid model of vortex shedding from a circular cylinder in steady and oscillatory far flows," Proceedings of the Institution of Civil Engineers, Vol. 63, 865-880, 1977.

E17. S.E. Hurlbut, M.L. Spaulding and F.M. White, "Numerical Solution of the Time Dependent Navier-Stokes Equations in the Presence of an Oscillating Cylinder," in *Numerical Solution of Non-Steady Flows,* ASME: New York, 201-206, 1978.

E18. S.E. Hurlbut and M.L. Spaulding, "A Numerical Model of Fluid-Structure Interaction for Circular Cylinders," University of Rhode Island, Department of Ocean Engineering Contract Report, November 1978.

E19. P.M. Greshko, R.L. Lee and C.D. Upson, "FEM solution of the Navier-Stokes equations for the vortex shedding behind a cylinder: experiments with the four-node element," in *Proceedings of the Third International Conference on Finite Elements in Water Resources (Preprints),* The University of Mississippi: Oxford, Vol. 2, 4.48-4.65, 1980.

Table E1. Normal Modes $\psi_i(z)$ and Corresponding Values of $I_i^{-1/2}$ for Various Structural Forms

I. Pivoted Rigid Rod

Normal modes: $\psi_1 = \bar{z}/L, \psi_{i\neq 1} = 0$

$I_i^{-1/2}$: $(5/3)^{1/2} = 1.2910$

II. Taut String

Normal modes: $\psi_i = \sin i\pi\bar{z}/L$

$I_i^{-1/2}$: $(4/3)^{1/2} = 1.1547$

III. Pinned-Pinned Beam

Normal modes: $\psi_i = \sin i\pi\bar{z}/L$

$I_i^{-1/2}$: $(4/3)^{1/2} = 1.1547$

IV. Cantilevered Beam

Normal modes; $\psi_i = \cosh \lambda_i\bar{z}/L - \cos \lambda_i\bar{z}/L - \alpha_i(\sinh \lambda_i\bar{z}/L - \sin \lambda_i\bar{z}/L)$

i	λ_i	α_i	$I_i^{-1/2}$
1	1.87510410	0.73409550	0.6525
2	4.19409113	1.01846644	0.7494
3	7.85475743	0.99922450	0.7686

V. Clamped-Clamped Beam

Normal modes: $\psi_i = \cosh \lambda_i\bar{z}/L - \cos \lambda_i\bar{z}/L - \alpha_i(\sinh \lambda_i\bar{z}/L - \sin \lambda_i\bar{z}/L)$

i	λ_i	α_i	$I_i^{-1/2}$
1	4.75300408	0.98250222	0.7348
2	7.8532046	1.00077731	0.7694
3	10.9956078	0.99996645	0.7817

VI. Clamped-Pinned Beam

Normal modes: $\psi_i = \cosh \lambda_i\bar{z}/L - \cos \lambda_i\bar{z}/L - \alpha_i(\sinh \lambda_i\bar{z}/L - \sin \lambda_i\bar{z}/L)$

i	λ_i	α_i	$I_i^{-1/2}$
1	3.92660230	1.00077730	0.7694
2	7.06858275	1.00000144	0.7891
3	10.21027613	1.00000000	0.7972

VII. Free-Pinned Beam

Normal modes: $\psi_i = \cosh \lambda_i(\bar{z}/L) + \cos \lambda_i(\bar{z}/L) - \alpha_i[\sinh \lambda_i(\bar{z}/L) + \sin \lambda_i(\bar{z}/L)]$

i	λ_i	α_i	$I_i^{-1/2}$
1	3.92660	1.000773	0.7628
2	7.06858	1.000000	0.7890
3	10.2102	1.000000	0.7972

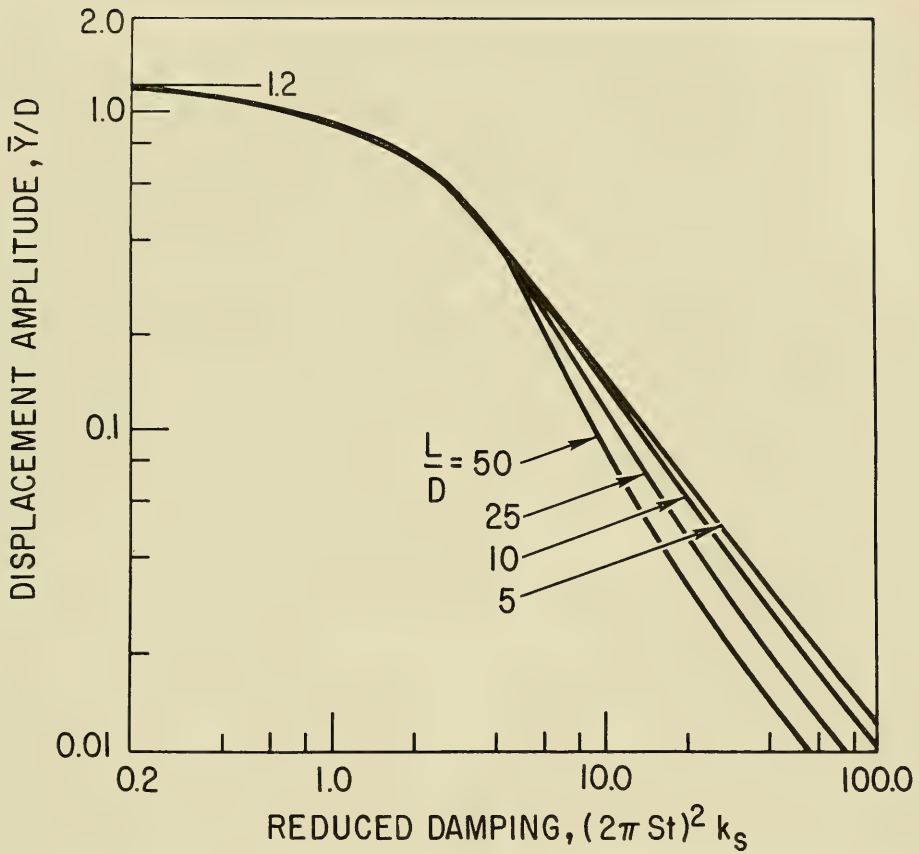

Figure E1 Predicted cross flow displacement amplitude $\bar{Y}/D$ plotted against the reduced damping $(2\pi St)^2 k_s$ for the sine mode resonant response of a flexible structure; from Blevins and Burton (E8). The aspect ratio of the structure, i.e., a cable, is given by L/D.

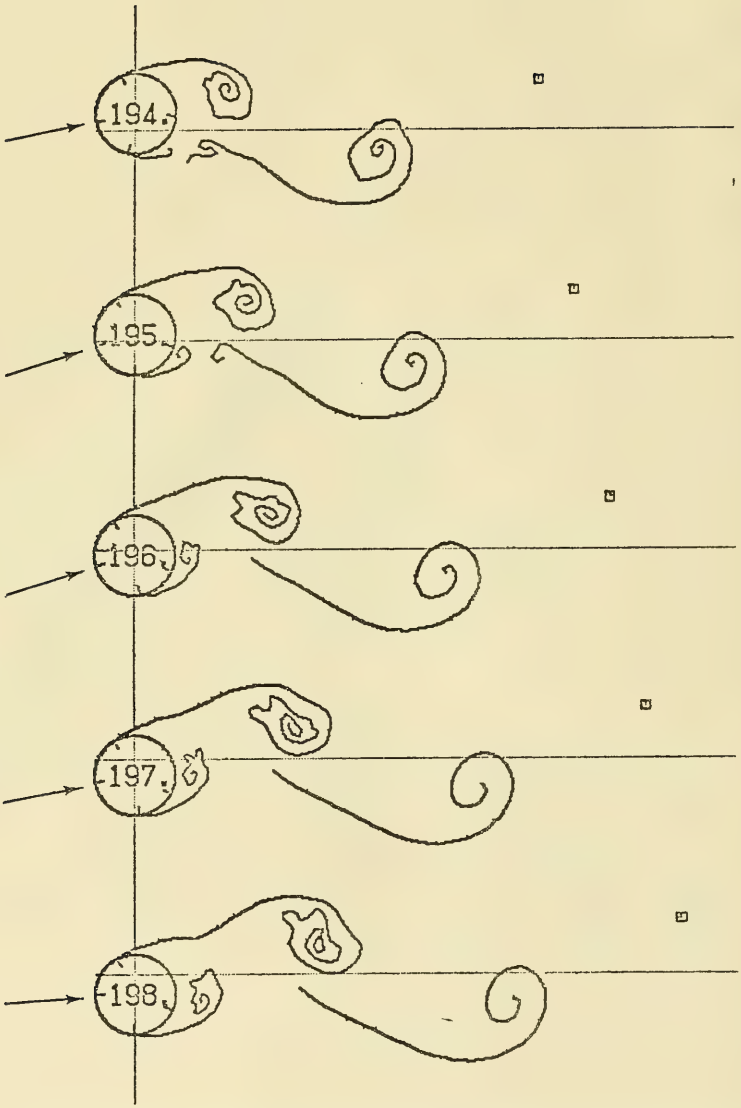

Figure E2 Evolution with time of the vortex shedding in the wake of an oscillating cylinder; from Sarpkaya and Shoaff (E12). The vortex sheets emanating from the cylinder are calculated with the discrete vortex method (DVM). The arrow represents the direction of the incident flow relative to the instantaneous position of the cylinder.

DISTRIBUTION LIST

AFB CESCH, Wright-Patterson
ARCTICSUBLAB Code 54, San Diego, CA
ARMY ARRADCOM, Dover, NJ; BMDSC-RE (H. McClellan) Huntsville AL; Coastal Engr Res Ctr, Eckert, Ft Belvoir, VA
ARMY - CERL Library, Champaign IL
ARMY COASTAL ENGR RSCH CEN Fort Belvoir VA; R. Jachowski, Fort Belvoir VA
ARMY COE Philadelphia Dist. (LIBRARY) Philadelphia, PA
ARMY CORPS OF ENGINEERS MRD-Eng. Div., Omaha NE; Seattle Dist. Library, Seattle WA
ARMY CRREL A. Kovacs, Hanover NH; Library, Hanover NH
ARMY DARCOM Code DRCMM-CS Alexandria VA
ARMY ENG WATERWAYS EXP STA Library, Vicksburg MS
ARMY ENGR DIST. Library, Portland OR
ARMY ENVIRON. HYGIENE AGCY HSE-EW Water Qual Eng Div Aberdeen Prov Grnd MD
ARMY MATERIALS & MECHANICS RESEARCH CENTER Dr. Lenoe, Watertown MA
ARMY MOBIL EQUIP R&D COM DRDME-GS Fuel Tech Br, Ft Belvoir, VA; Mr. Cevasco, Fort Belvoir MD
ARMY TRANSPORTATION SCHOOL Code ATSPO CD-TE Fort Eustis, VA
ASST SECRETARY OF THE NAVY Spec. Assist Energy (Leonard), Washington, DC; Spec. Assist Submarines, Washington DC
CNM MAT 08T245 (Spalding), Washington, DC; MAT-0718, Washington, DC; NMAT - 044, Washington DC
CNO Code NOP-964, Washington DC; Code OP 323, Washington DC; Code OPNAV 09B24 (H); Code OPNAV 22, Wash DC; Code OPNAV 23, Wash DC; OP-23 (Capt J.H. Howland) Washinton, DC; OP987J (J. Boosman), Pentagon
COMNAVBEACHPHIBREFTRAGRU ONE San Diego CA
COMSUBDEVGRUONE Operations Offr, San Diego, CA
DEFENSE INTELLIGENCE AGENCY DB-4C1 Washington DC
DTIC Defense Technical Info Ctr/Alexandria, VA
DTNSRDC Code 522 (Library), Annapolis MD; Pattison, Code 1706, Bethesda, MD; Rispin, Code 1706, Bethesda, MD
HCU ONE CO, Bishops Point, HI
MCAS Facil. Engr. Div. Cherry Point NC
MILITARY SEALIFT COMMAND Washington DC
NAF PWO, Atsugi Japan
NALF OINC, San Diego, CA
NARF Equipment Engineering Division (Code 61000), Pensacola, FL
NAS Dir. Util. Div., Bermuda; ENS Buchholz, Pensacola, FL; PWD - Engr Div, Oak Harbor, WA; PWD Maint. Div., New Orleans, Belle Chasse LA; PWD, Code 1821H (Pfankuch) Miramar, SD CA; PWO Belle Chasse, LA; PWO Key West FL; PWO, Glenview IL; SCE Norfolk, VA; Shore Facil. Ofr Norfolk, VA
NATL BUREAU OF STANDARDS Kovacs, Washington, D.C.
NAVACT PWO, London UK
NAVAEROSPREGMEDCEN SCE, Pensacola FL
NAVAIRDEVCEN Code 813, Warminster PA
NAVCOASTSYSTCTR CO, Panama City FL; Code 715 (J Quirk) Panama City, FL; Code 715 (J. Mittleman) Panama City, FL; Library Panama City, FL
NAVCOMMAREAMSTRSTA SCE Unit 1 Naples Italy
NAVCOMMSTA Code 401 Nea Makri, Greece; PWD - Maint Control Div, Diego Garcia Is.; PWO, Exmouth, Australia
NAVEDTRAPRODEVCEN Technical Library, Pensacola, FL
NAVELEXSYSCOM PME 124-30 (Henderson) Washington, DC; PME 124-612, Wash DC
NAVEODFAC Code 605, Indian Head MD
NAVFAC PWO, Centerville Bch, Ferndale CA
NAVFACENGCOM Code 043 Alexandria, VA; Code 044 Alexandria, VA; Code 0453 (D. Potter) Alexandria, VA; Code 0453C, Alexandria, VA; Code 04A1 Alexandria, VA; Code 100 Alexandria, VA; Code 1002B (J. Leimanis) Alexandria, VA; Code 1113 (T. Stevens) Alexandria, VA; Morrison Yap, Caroline Is.
NAVFACENGCOM - CHES DIV. Code 407 (D Scheesele) Washington, DC; Code FPO-1E, Wash. DC; FPO-1 (Kurtz) Washington, DC; FPO-1 Wash, DC; FPO-1C (Spencer), Washington, DC

NAVFACENGCOM - LANT DIV. Eur. BR Deputy Dir, Naples Italy; European Branch, New York; RDT&ELO 102, Norfolk VA
NAVFACENGCOM - NORTH DIV. (Boretsky) Philadelphia, PA; CO; Code 1028, RDT&ELO, Philadelphia PA; Design Div. (R. Masino), Philadelphia PA; ROICC, Contracts, Crane IN
NAVFACENGCOM - PAC DIV. Code 402, RDT&E, Pearl Harbor HI; Commander, Pearl Harbor, HI
NAVFACENGCOM - SOUTH DIV. Code 90, RDT&ELO, Charleston SC
NAVFACENGCOM - WEST DIV. Code 04B San Bruno, CA; O9P/20 San Bruno, CA; RDT&ELO Code 2011 San Bruno, CA
NAVFACENGCOM CONTRACT Eng Div dir, Southwest Pac, Manila, PI; OICC, Southwest Pac, Manila, PI; OICC/ROICC, Balboa Canal Zone; ROICC, NAS, Corpus Christi, TX
NAVOCEANO Library Bay St. Louis, MS
NAVOCEANR&DACT Swenson, NSTL Station, MS
NAVOCEANSYSCEN Code 41, San Diego, CA; Code 4473 Bayside Library, San Diego, CA; Code 4473B (Tech Lib) San Diego, CA; Code 52 (H. Talkington) San Diego CA; Code 5204 (J. Stachiw), San Diego, CA; Code 5214 (H. Wheeler), San Diego CA; Code 5221 (R.Jones) San Diego Ca; Code 5311 (Bachman) San Diego, CA
NAVPGSCOL C. Morers Monterey CA; E. Thornton, Monterey CA
NAVPHIBASE CO, ACB 2 Norfolk, VA; COMNAVBEACHGRU TWO Norfolk VA; Code S3T, Norfolk VA; Harbor Clearance Unit Two, Little Creek, VA; SCE, Coronado, San Diego CA
NAVREGMEDCEN SCE (D. Kaye)
NAVSCOLCECOFF C35 Port Hueneme, CA
NAVSEASYSCOM Code PMS 395 A 3, Washington, DC; Code SEA OOC Washington, DC
NAVSHIPREPFAC Library, Guam; SCE Subic Bay
NAVSHIPYD Bremerton, WA (Carr Inlet Acoustic Range); Code 202.4, Long Beach CA; Code 202.5 (Library) Puget Sound, Bremerton WA; Code 440 Portsmouth NH; Code 440, Puget Sound, Bremerton WA; Library, Portsmouth NH; Tech Library, Vallejo, CA
NAVSTA CO Naval Station, Mayport FL; CO Roosevelt Roads P.R. Puerto Rico; PWD (LTJG.P.M. Motolenich), Puerto Rico; PWO Pearl Harbor, HI; PWO, Keflavik Iceland; PWO, Mayport FL; SCE, Guam; SCE, Subic Bay, R.P.; Security Offr, San Francisco, CA
NAVSUPPACT LTJG McGarrah, SEC, Vallejo, CA
NAVTECHTRACEN SCE, Pensacola FL
NAVWPNCEN Code 3203, China Lake, CA
NAVWPNSTA Code 092, Colts Neck NJ
NAVWPNSTA PW Office (Code 09C1) Yorktown, VA
NAVWPNSTA PWD - Maint. Control Div., Concord, CA; PWD - Supr Gen Engr, Seal Beach, CA; PWO, Charleston, SC; PWO, Seal Beach CA
NAVWPNSUPPCEN Code 09 Crane IN
NCBC Code 10 Davisville, RI; Code 15, Port Hueneme CA; Code 155, Port Hueneme CA; Code 156, Port Hueneme, CA
NMCB FIVE, Operations Dept
NOAA DATA BUOY OFFICE Engrng Div (Riannie) Bay St. Louis, MS
NORDA CO, Bay St. Louis, MS; Code 350 (Swenson) Bay St. Louis, MS; Code 410 Bay St. Louis, MS; Code 440 (Ocean Rsch Off) Bay St. Louis MS
NRL Code 5800 Washington, DC; Code 5843 (F. Rosenthal) Washington, DC; Code 8441 (R.A. Skop), Washington DC; Griffith, Wash., DC
NROTC J.W. Stephenson, UC, Berkeley, CA
NSD SCE, Subic Bay, R.P.
NUSC Code 131 New London, CT; Code 332, B-80 (J. Wilcox) New London, CT; Code EA123 (R.S. Munn), New London CT; Code TA131 (G. De la Cruz), New London CT
OCEANSYSLANT LT A.R. Giancola, Norfolk VA
ONR (Scientific Dir) Pasadena, CA; Cagle, Pasadena, CA; Central Regional Office, Boston, MA; Code 481, Bay St. Louis, MS; Code 485 (Silva) Arlington, VA; Code 700F Arlington VA
PHIBCB 1 P&E, San Diego, CA; 1, CO San Diego, CA
PMTC Code 3331 (S. Opatowsky) Point Mugu, CA; Code 4253-3, Point Mugu, CA; EOD Mobile Unit, Point Mugu, CA; Pat. Counsel, Point Mugu CA
PWC CO Norfolk, VA; CO, (Code 10), Oakland, CA; CO, Great Lakes IL; CO, Pearl Harbor HI; Code 10, Great Lakes, IL; Code 120, Oakland CA; Code 120C, (Library) San Diego, CA; Code 128, Guam; Code

154, Great Lakes, IL; Code 200, Great Lakes IL; Code 30C, Norfolk, VA; Code 30C, San Diego, CA; Code 400, Great Lakes, IL; Code 400, Pearl Harbor, HI; Code 400, San Diego, CA; Code 420, Great Lakes, IL; Code 420, Oakland, CA; Code 700, San Diego, CA

UCT TWO OIC, Norfolk, VA; OIC, Port Hueneme CA

US NAVAL FORCES Korea (ENJ-P&O)

USCG G-ECV (C E Smith) Washington, DC

USCG R&D CENTER D. Paskausky, Groton, CT; Debok, Avery Point, CT

USNA Ch. Mech. Engr. Dept Annapolis MD; Civil Engr Dept (R. Erchyl) Annapolis MD; Ocean Sys. Eng Dept (Dr. Monney) Annapolis, MD; PWD Engr. Div. (C. Bradford) Annapolis MD

WOODS HOLE OCEANOGRAPHIC INST. Doc Lib LO-206, Woods Hole MA

DEPARTMENT OF THE NAVY

CIVIL ENGINEERING LABORATORY
NAVAL CONSTRUCTION BATTALION CENTER
PORT HUENEME, CALIFORNIA 93043

OFFICIAL BUSINESS
PENALTY FOR PRIVATE USE, $300

POSTAGE AND FEES PAID
DEPARTMENT OF THE NAVY
DoD-316

U.S.MAIL

85 - 823.001 - 140 1

Document Library L0-206
Woods Hole Oceanographic Institution
Woods Hole, MA 02543